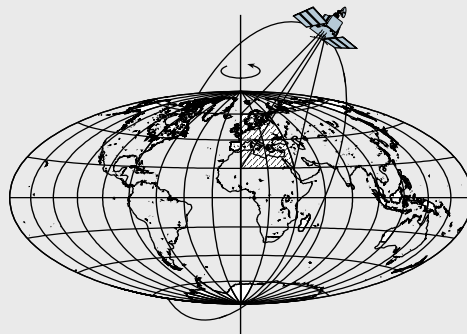


# SATELLITE RADAR ALTIMETRY FOR INLAND HYDROLOGIC STUDIES

by

Manman Zhang



Report No. 491

Geodetic Science and Surveying

The Ohio State University  
Columbus, Ohio 43210

March 2009

**SATELLITE RADAR ALTIMETRY FOR  
INLAND HYDROLOGIC STUDIES**

**Manman ZHANG**

## ABSTRACT

Satellite radar altimetry, which is originally designed to measure global ocean surface height, has been applied to inland surface water hydrologic studies. We have developed a water-detection algorithm based on statistical analysis of decadal TOPEX/POSEIDON height measurement time series, used the backscatter coefficient to classify the inland surface properties, and the 10-Hz (corresponding to an along track spatial resolution of 700m) radar waveform-retracked TOPEX data, to be able to observe small ( $<300\text{Km}^2$ ) inland bodies of water for hydrologic studies. We applied the algorithm to the selected study regions in Manitoba and northwestern (SW) Ontario, Canada, Amazon River Basin, and southwestern Taiwan. Finally we studied the application of TOPEX altimetry to the 1997 Red River flood monitoring. For the study regions in western Manitoba, the correlation coefficient between stage and TOPEX altimetry data in the large Lakes reaches 0.98 using the 10-Hz retracked data, thus verifying the validity and accuracy of the satellite measurement. The importance of the waveform retracking for the inland water applications is validated by the improvement of the correlation coefficients from 0.34 to 0.87 before and after retracking. We detected the bodies of water, which are otherwise missed by using the original 1-Hz data from the Geophysical Data Records, and illustrated that a higher spatial resolution could be achieved using the individual 10-Hz retracked data. In the Amazon River Basin, the capability of the water-detection algorithm is compared with the use of a high water level mask generated by SAR and other data with a spatial resolution of 100m. It is shown that the algorithm could detect the bodies of water, which are missed by the mask primarily because that the frequency of water fluctuation is more than twice a year at some locations. The bodies of water detected only by the algorithm are confirmed using the detailed local hydrological maps in 3 tested regions. The retrieved water height over the small ( $<300\text{Km}^2$ ) body of water was compared with the nearby stage measurement and showed good seasonal agreement. In the southwest Taiwan, the monthly variation of 10-Hz AGC from 1992 to 2002 were examined, it is found that the high AGC values could be used to indicate inundated area. We detected the annual and semi-annual variations from the 10-Hz AGC and 10-Hz retracked water height time series, which are attributable to two rainy seasons per year in the study region. For the study of the 1997 Red River flood, we compared the geographic distribution of  $\sigma_0$  before, during and after the 1997 flood and found the high  $\sigma_0$  values ( $>35\text{dB}$ ) indicate the inundated regions. In addition, the comparison of the geographically distributed  $\sigma_0$  during Winter, Spring, Summer and Autumn of 1997 showed that the low  $\sigma_0$  values ( $<10\text{dB}$ ) indicate snow coverage. The retrieved water height measurements in the flooded regions are compared with the nearby USGS stage measurements and showed good agreements. The comparison of 10-Hz individual retracked measurements with the 1-Hz non-retracked height measurements confirmed the importance of the retracked data (with higher

spatial variations) in the flood monitoring. Using  $\sigma_0$  and the retrieved water height measurements, we detected the 1997 flooded regions include the Red River Basin of the North in North Dakota and in western Minnesota, the upper Mississippi River Basin in Minnesota, the Missouri River Basin in southern North Dakota and in South Dakota. The observed flood extents from TOPEX agree well with and complement the USGS stage gauge records.

## PREFACE

This research is conducted under the supervision of Dr. C.K. Shum, Professor of Geodetic Science, School of Earth Sciences, The Ohio State University. The research results documented in this report resulted in a PhD Dissertation. NASA and CNES provided the TOPEX/POSEIDON (Geophysical Data Record and Sensor Data Record, GDR and SDR) data products; LEGOS, USDA/NASA/GSFC provided high-level radar altimetry data products; ANA Brazil, and Environment Canada provided the stage gauge data used for this research. This research is supported by grants from NSF's Hydrology Program (EAR-0440007) and NGA's NURI Program (HM1582-07-1-2024), and the study was conducted with the objective to contribute to the Climate, Water, and Carbon Program at The Ohio State University.

March 29, 2009

## ACKNOWLEDGEMENT

I would like to express my sincere gratitude to Professor C. K. Shum, my adviser, for his professional guidance, inspiring consultation, and financial support to make this research possible. I thank Professor Doug Alsdorf, Professor Alan Saalfeld, and Professor Frank Schwartz for their invaluable comments and for serving on my dissertation committee. I acknowledge Dr. Hyongki Lee's numerous invaluable discussions with me, and for his help on satellite radar altimeter processing. I thank Justin Shum for proof-reading this dissertation.

# TABLE OF CONTENTS

	Page
ABSTRACT .....	ii
PREFACE .....	iv
ACKNOWLEDGMENTS .....	v
 CHAPTERS:	
1. INTRODUCTION .....	1
1.1 Introduction.....	1
1.2 The Backscattered Power of Satellite Altimetry.....	5
1.2.1 Backscatter Coefficient for Ocean.....	6
1.2.2 Illuminated Area of Pulse-limited Altimetry.....	8
1.2.3 Waveform of Satellite Altimetry.....	13
1.3 Summary of Chapters .....	16
 2. DATA PROCESSING.....	 17
2.1 Radar Altimeter Waveform Retracking Methods.....	17
2.1.1 Waveform of Inland Water.....	17
2.1.2 Retracking Methods .....	21
2.2 Data Description .....	25
2.3 Range Estimation.....	26

2.4 The Satellite Altimeter Stackfile Database.....	27
3. VALIDATION OF THE WATER-DETECTION ALGORITHM.....	32
3.1 Water-Detection Algorithm Description .....	32
3.2 Manitoba and SW Ontario.....	34
3.3 The Amazon River Basin .....	41
3.4 Southwestern Taiwan .....	48
3.5 Conclusions.....	53
4. THE 1997 RED RIVER FLOOD.....	54
4.1 Introduction.....	54
4.2 Flood Extent and Snow Coverage Detection Using Backscatter Coefficients..	55
4.3 The 1997 Red River Flood in North Dakota.....	62
4.4 The 1997 Flood in Minnesota, South Dakota and Iowa.....	74
4.5 Conclusions .....	78
5. CONCLUSIONS .....	80
BIBLIOGRAPHY .....	83

# CHAPTER 1

## INTRODUCTION

### 1.1 Introduction

Inland bodies of water are the habitat for diverse biological communities, such as fishes and ducks. Terrestrial water support stunning proportion of plants and animals (Margalef, 1994). Many human activities in different fields rely on the inland water such as: fishery, agriculture drainage, nutrition absorption and recycling, urban and industrial water purification and supply, power generation, and flood management (Oki et al, 2006). Human activities change the quality and quantity of the water. The improper usage of water threatens the aquatic ecosystems as well as human life. Currently, nobody knows if there is enough fresh water for us to use in the future. One-third of the global populations do not have access to clean fresh water (Alsdorf et al, 2007, Gleick, 2003). To facilitate the strategic planning of management of inland water, the knowledge of the surface water resource distribution is necessary (Alsdorf et al, 2007, Marburger and Bolten, 2004, 2005).

There are hundreds of thousands of reservoirs and millions of lakes in the world. However, it is still unclear how the storage of these water bodies change and how they interact with climate change. Hydrology is an interdisciplinary science dealing with the global water cycle, which is related to the origin, distribution, volume, and properties of water on the globe (Dingman, 2002). Monitoring, understanding and modeling of global terrestrial hydrology represent the basis for development and management of global water resources. Despite its importance, hydrologic and hydraulic studies are hindered by the limitation of the traditional hydrological observing tools—in-situ gauge measurements. The global hydrological prediction strategy is impossible with only the in-situ stage gauge because there are water bodies in many different countries. The stage gauge measurements are only available at limited sites within a watershed and are especially restricted by the inaccessibility of remote study regions. The availability of the in-situ data is limited by logistical problems or political reasons resulting in the inaccessibility of the hydrologic data to users. Satellite remote sensing measurements have been demonstrated to be effective for hydrologic studies over a large basin or at the global scale with adequate temporal and spatial resolutions.

In particular, satellite radar altimetry has the advantage of global coverage and is an all-weather sensor. It has revolutionized the global ocean science with its unprecedented accuracy of several centimeters root-mean-square (RMS) of measurement of sea surface height from space (Fu et al., 1994a). It provides information about ocean topography, wind speed, tidal parameters, and dry and wet atmospheric corrections (Fu & Pihos, 1994b). In 1969, American scientist W.M. Kaula first proposed the concept of satellite altimetry in the NASA Williamstown conference (Kaula, 1970), after that the first satellite altimeter Skylab was launched by NASA in May 1973, several altimetry satellites were launched afterwards. A brief summary of satellite altimeters is listed in Table 1.1. The accuracy of TOPEX/POSEIDON and ENVISAT could reach several centimeters for ocean surface measurement with the support of on board high precision GPS position technology and the improved geopotential model, EGM96.

Although satellite radar altimetry was originally designed for deep ocean circulation studies, they have demonstrated excellent potential to study large terrestrial bodies of water. The use of satellite altimetry, such as TOPEX/POSEIDON, ENVIRONMENTAL SATELLITE (ENVISAT), JASON-1, and JASON-2 could observe global surface water topography height with an accuracy of several cm and a spatial resolution of ~100km with approximately weekly or monthly sampling. Brooks (1982) used lake elevation measurements from Seasat in the mapping to control ground points. Rapley et al. (1987) showed the surface height (maintain lock) over 32% of earth's land surface is able to be acquired. Rapley interpreted the Seasat radar echoes over the wetland, where surface slope is small, and showed wetland were well observed. Following him, Cudlip et al. (1990) produced the first surface elevation contour maps for Sudd Marshes and the Amazon Basin as well as provided the variation of water level of the Sudd Marshes. Guzkowska et al. (1990) investigated the prospect of the application of satellite altimetry in inland water and estimated the absolute elevation profile of the Amazon using Seasat measurement. These preliminary results demonstrated the potential of satellite altimetry to measure water levels in the continent, although the usage of the measurement are limited due to the short life (3 months) of the Seasat satellite and the inaccurate Seasat Satellite orbit value (Rapley et al. 1987).

Koblinsky et al. (1993) explored the capability of satellite altimetry further using U.S. Navy's Geodetic Satellite (GEOSAT) which operated from period 1985-1989 with temporal resolution 17.05 days. The GEOSAT measurements are retrieved at 4 locations in the Amazon River Basin where river gauges are available. His comparison of satellite altimetry measurement with tide gauge measurement showed that the root-mean-square (RMS) of satellite measurements range from 0.7m-1.2m. The more extensive study of GEOSAT was hindered by a variety of difficulties for the GEOSAT measurement over rough terrain. However, researching terrestrial water using measurement of satellite radar altimetry was predicted to be promising after the operation of satellites TOPEX/POSEIDON and ERS1/ENVISAT, which corrected many problems of GEOSAT satellite (Koblinsky et al., 1993).

Name	Seasat	Geosat	ERS-1	ERS2	ENVISAT	TOPEX/POSEIDON	Jason 1/2
country	USA	USA	Europe	Europe	Europe	USA/France	USA/France
Mission Period	Jul., 1978 -Oct., 1978	Mar., 1985 -Dec., 1989	Jul., 1991 -May, 1996	Apr., 1995 - Jun.,2003	Mar.,2002 -present	Aug.,1992	Dec., 2001
Altitude of orbit(km)	800	800	785	785	785	1336	1336
Inclination of orbit(degree)	108	108	98.5	98.5	98.5	66	66
Equatorial Ground Track Interval (km)	800,160	164	20-80	80	80	318	318
Period (days)	3,17	17	3,35,168	35	35	10	10
Measurement Accuracy(cm)	5	4	3	3	3	2	2

Table 1.1: Summary of satellite radar altimeters.

1. The interval of tracks along the equator is computed from the Equation:  $\Delta = 2 * \pi * R / (n - 1)$ , where R is the radius of earth at equator, 6378km, n is number of equator crossing cycles for descending passes and ascending passes, for ENVISAT n= 501, TOPEX/POSEIDON n= 127.

2. The accuracy of the Seasat and Geosat information refer to orbits after subsequent improvements in precision orbit determination applied retroactively, which reduce the orbits' error to about 20cm for Seasat and 10-20cm for Geosat (Fu & Cazenave, 2001).

The application of satellite radar altimeter over the inland water has been explored more extensively after the TOPEX/POSEIDON and ERS1/ENVISAT began to operate. Birkett (1995) showed that TOPEX/POSEIDON measurement could reach 4cm RMS accuracy for the Great lakes and demonstrated the capability of a satellite to monitor the inland water with area  $> 300\text{km}^2$  (Morris, et al., 1994, Birkett, 1995). Cazenave et al. (1997) detected that from January 1993 to July 1995 there is  $18.9 \pm 0.5\text{cm/yr}$  level rise of Caspian Sea which is the largest inland sea of the world (Cazenave et al, 1997) extending over 1200km from north to south using TOPEX/POSEIDON. Stanev et al. (2004) observed a drop of the water level at rate 0.6m/year for the Aral Sea, which is an enclosed sea in an arid/desert region of Asia during 1993 to 2000 using TOPEX/POSEIDON.

Besides the demonstration of the capability of the satellite to monitor great lakes and inland seas, scientists expanded the application of satellites into large river/lake basins. Birkett researched the contribution of TOPEX/POSEIDON radar altimeter to monitor the large rivers and wetlands (Birkett, 1998). She demonstrated that TOPEX/POSEIDON can successfully track both large wetland and rivers with width  $>1\text{km}$  with accuracy up to 11cm RMS. Coe & Birkett (2004) calculated the river discharge and prediction of lake height from TOPEX/POSEIDON for the lake Chad basin. The other regions that have been demonstrated to be monitored well using satellite altimetry was the Amazon River Basin (Birkett et al, 2002, Berry et al, 2005, Zakharova et al, 2006). Birkett et al. (2002) demonstrated that TOPEX/POSEIDON could successfully monitor the transient flood waves of this continental scale river with mean accuracy up to tens of centimeters. Berry et al. (2005) validated the Amazon basin level measurement at one location using multiple satellite altimeters, including TOPEX, ERS-1/ENVISAT. Mercier et al. (2002) studied the inter-annual lake level fluctuations in Africa using TOPEX/POSEIDON. Zakharova et al. (2007) analyzed the variability of water level for large reservoirs and lakes in Euphrates-Tigris Rivers using multiple satellites, including the TOPEX/POSEIDON, ENVISAT and Geosat Follow-On (GFO).

At present, research institutions providing high-level surface water height data products for hydrologic studies include the Laboratory of d'Etudes en Geophysique et Oceanographie Spatiales (LEGOS) (<http://www.legos.obs-mip.fr>), and US Department of Agriculture and NASA's Goddard Space Flight Center (GSFC) ([http://www.pecad.fas.usda.gov/cropexplorer/global\\_reservoir/](http://www.pecad.fas.usda.gov/cropexplorer/global_reservoir/)). Both data centers primarily used 1-Hz TOPEX/POSEIDON (and other altimetry) data or averaged data of several individual 10-Hz data without radar waveform retracking. The other kind of radar altimetry hydrologic data products is available from the "Contribution of Spaceborne Altimetry to Hydrology" (CASH) Project (Seyler et al., 2007), which was established by the Réseau Terre et Espace, French Ministry of Research and Technology. The CASH project has realized the retracking of the TOPEX/POSEIDON archive with the algorithms used in the ENVISAT waveform retracking procedure, i.e. the retrackers OCEAN, ICE1, ICE2 and SEAICE (Benveniste et al., 2002). These TOPEX/POSEIDON retracked hydrologic data products for about 80 altimetric time series over 8 great fluvial basins in the world are available at: <http://ocean.cls.fr/html/cash/welcome.html>.

The regions studied in the previous research are big rivers and lakes, and none of them used individual 10-Hz TOPEX/POSEIDON retracked measurements. The returned

waveforms over the large bodies of water are well behaved according to the altimeter instrument design criteria over ocean, primarily because these inland bodies of water are large ( $>300\text{km}^2$ ) and directly underneath the satellite ground track. As a result, the surface water heights have been accurately computed assuming that radar waveforms conform to the Brown-Model (Brown, 1977) which is designed for deep-ocean radar scatter modeling. When a body of water becomes smaller, the shape of the waveform changes and the non-retracked data cannot be directly used without retracking of the radar waveform. This study extends the technique developed by Lee et al. (2008), which optimally retracks individual 10-Hz TOPEX/POSEIDON waveforms for geodynamics and wetland applications, to apply to several study regions containing small bodies of inland water for hydrologic studies.

Another problem involved in the study of small bodies of water is the unavailability, in general, of high-resolution masks which enable classification of water and land-covers at the sub-satellite points of the satellite measurements. One such high-resolution mask was developed by Hess et al. (2003) over the Amazon basin. They used JERS-1 L-Band Synthetic Aperture Radar (SAR) to map Amazon wetland extents, land inundation and vegetation extents with 100-m resolution and for high-water and low-water seasons. These masks have the potential disadvantage that even a two-season per year classification may not be adequate to completely classify the inundation extents of the study region. Other generated masks used data from satellites carrying optical/infrared sensors, such as LANDSAT TM, which often have problems with cloud and smoke cover contaminations, or problems from the canopy above the water area. Generation of masks usually is tedious and thus global high-resolution ( $<100\text{m}$ ) masks are in general unavailable.

A potential new classification method using information from one satellite system, i.e., satellite radar altimetry, to classify the water from other land covers using radar backscatter has been demonstrated by Papa et al. (2003) using TOPEX/POSEIDON radar altimetry. In this study, we propose an algorithm towards semi-automated water-detection and retrieval of accurate surface water height measurement by retracking of TOPEX radar altimeter measurements, land-cover classification using radar backscatter coefficient, and based on the statistics of the generated water height inferred by radar altimetry. The algorithm is tested in three study regions: Manitoba and Ontario, the Amazon basin, and the southwestern Taiwan terrain. Each of these regions is distinct in its climatology, land cover, and the size of water inundation areas. The objective is to test the developed algorithm to detect and obtain accurate surface water height measurements over the relatively small bodies of water. The combination of the semi-automated classification method and the optimally retracked 10-Hz retracked measurement explores the potential of the application of the satellite altimetry over small terrestrial bodies of water, which can maximize the usage of satellite radar altimetry to study surface water hydrology.

## 1.2 The Backscattered Power of Satellite Altimetry

The microwave frequency range of satellite radar altimetry is 2-18GHz, which include S-band (1.55-4.20GHz), C-band (4.20-5.75GHz), X-band (5.75-10.9GHz) and Ku-band (10.9GHz-22.0GHz). There are several reasons to choose this range for the radar altimeter.

First, within this range the signal reflected from water is strong and the graybody emission of electromagnetic radiation from the sea surface is very weak, so it is easy to measure the returned signal with little interruption of the natural emissions (Fu & Cazenave, 2001). Secondly, the atmospheric attenuation of the returned signal increases rapidly at the higher frequency, consequently the power returned from the water surface will decrease rapidly at the higher frequency. Thirdly, at lower frequency there are civilian and military applications of radar, such as navigation and communication, which result in the increased interference. In addition, the ionosphere refraction of electromagnetic radiation increases, so at lower frequency the accuracy of the measurement of the returned signal could be decreased.

### 1.2.1 Backscatter Coefficient for Ocean

One of the fundamentals of the measurement from satellite altimetry is the ratio of the power of the signal received at the antenna and the power transmitted from the antenna. After the electromagnetic radiation is transmitted from the satellite, it is attenuated while it went through the atmospheric; then it arrives at the water surface. Some of the power are backscattered and some are absorbed by the water; during the pass to go back to the satellite, the power is attenuated again by the atmospheric and received by the satellite. During the whole process the power of the backscattered signal is influenced by the 2-way atmospheric attenuation, the parameter of the satellite and the scattering character of the water surface. The backscattered power from the satellite footprint could be computed using Equation (1.1):

$$Pr = t_{\lambda}^2 \frac{\lambda^2 P_t}{(4\pi)^3 R^4} \int_{A_f} G^2 \sigma_0 dA \quad (1.1)$$

Where  $Pr, Pt$  are received and transmitted power in watts;  $\lambda$  is the wavelength of the transmitted and received electromagnetic radiation;  $t_{\lambda}(R, \theta)$  is the atmospheric transmittance, which is defined to be the fraction of electromagnetic radiation at wavelength  $\lambda$  that is transmitted through the atmosphere from an altitude  $R$  at off-nadir angle  $\theta$ ;  $G$  is the transmitted and received antenna gain;  $\sigma_0$  is normalized radar cross section, also called the backscatter coefficient; both of the  $G$  and  $\sigma_0$  change with the variation of off-axis angle so they are in the integral,  $R, \theta$  and  $A_f$  are illustrated in Figure 1.1. In Equation (1.1),  $R$  and  $\theta$  is assumed to be constant.

If the backscatter coefficient  $\sigma_0$  is spatially homogeneous over the antenna footprint, then Equation (1.1) could be rearranged to Equation (1.2):

$$\sigma_0 = \frac{(4 * \pi)^3 R^4}{t_{\lambda}^2 G_0^2 \lambda^2 A_{eff} P_t} P_r \quad (1.2)$$

Where  $G_0$  is the antenna gain at the antenna boresight, it is the peak gain;  $A_{eff}$  is the “effective footprint area” which is defined to be the area integral of  $G^2(\theta)/G_0^2$  over the angles  $\theta$  subtended by the antenna beamwidth; the other denotations are the same as in Equation (1.1). As explained for the Equation (1.1)  $G(\theta), G_0, \lambda, Pt$  are known parameters of radar system and  $R$  and  $t_{\lambda}(R, \theta)$  are physical parameters of the medium between the

altimeter and the target. So Equation (1.1) and (1.2) show the returned power depends on the backscatter coefficient, the parameter of the radar system and the measurement geometry parameters illustrated in Figure 1.1.

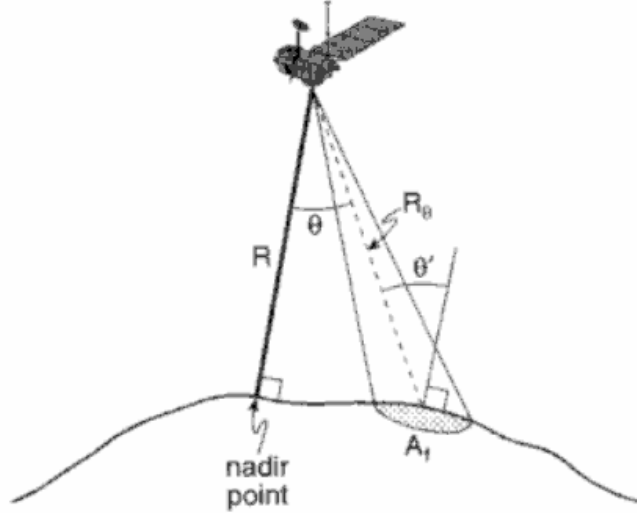


Figure 1.1: The geometry of satellite altimetry,  $R$  is the altitude of satellite,  $R_\theta$  is the slant range of the radar measurement at pointing angle  $\theta$ ,  $\theta'$  are incidence angle,  $A_f$  is the footprint area (Fu & Cazenave, 2001).

The normalized radar cross section, also called the backscatter coefficient, can be computed using Equation (1.3)

$$\sigma_0(\theta \approx 0) = \pi \rho^2(0^\circ) \sec^4 p(\xi_x, \xi_y) \Big|_{\xi_x = \xi_y = 0} \quad (1.3)$$

Where  $\xi$  is the sea-surface height relative to mean sea level;  $\rho^2(0^\circ)$  is the Fresnel reflectivity which is the fraction of incident radiation that is reflected for normal incident angle;  $p(\xi_x, \xi_y)$  is the joint probability density function of long-wave sea surface slopes  $\xi_x$  and  $\xi_y$  in two orthogonal directions. The “long-wave” means the portion of the ocean wave spectrum with wavelengths longer than that of the radar signal, for TOPEX/POSEIDON dual-frequency altimeter the wavelength is 2.3cm for 13.6GHz Ku band and 5.8cm for 5.4GHz C band. From Equation (1.3) we can see that the radar return closely related to the sea surface slopes which changes with different wind speed. For sea-surface, its roughness increases with the increase of wind speed. A typical altimetry measurement of  $\sigma_0$  is about 11dB, at very low wind speed  $\sigma_0$  is 20dB and it decreases to 5dB when wind speed increases to 30m/sec (Fu & Cazenave, 2001). As indicated in Equation (1.3), the radar

return is also related to the reflectivity of the surface. It is shown that the reflectivity of microwave with wavelength between 1cm and 1m at  $0^\circ$  incident angle is close to 1 when the temperature of water is  $25^\circ C$  (Maul, 1985).

### 1.2.2 Illuminated Area of Pulse-limited Altimetry

From Equation (1.1), we can see the size of the footprint plays an important role in the returned power, so we describe it briefly here. There are two satellite altimeter operating modes, the beam-limited and the pulse-limited as illustrated in Figure 1.2. For the beam-limited altimeter, the size of the corresponding footprint is defined to be the area within the field of view subtended by the beam width which is the full width at half power during the radiation time. For the pulse-limited altimeter, a short pulse is transmitted with a duration of a few nanoseconds, so the pulse does not illuminate the entire beam width footprint at the same time. The size of the corresponding footprint is defined by the pulse width which is smaller than the illuminated area. The pulse-limited mode measures the shortest range to the ground, while the beam-limited mode measures the range to the ground which locates at the radar pointing angle shown in Figure 1.1. The accuracy of the range measurement from a beam-limited mode is highly sensitive to antenna pointing errors. For example, a pointing error of only  $0.02^\circ$  introduces a range error 8cm for the TOPEX/POSEIDON with orbit height of 1336km. Another disadvantage of beam-limited altimeter is that their narrow beam width requires large antenna diameter as shown in Equation (1.4):

$$\gamma = k \frac{\lambda}{d} \quad (1.4)$$

Where  $\gamma$  is antenna beam-width;  $d$  is antenna diameter;  $k$  is a constant particular to the details of the illumination pattern across the antenna aperture (Ulaby et al., 1981). The altimeter with a large enough antenna is beam-limited. Since most satellite altimeter antennas are restricted in physical size, they tend to be pulse-limited.

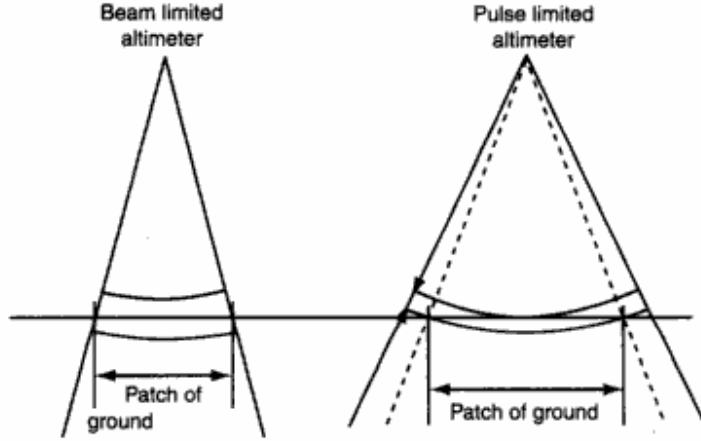


Figure 1.2: The illustration of the beam-limited altimeter and pulse-limited altimeter (Lacomme et al., 2001).

Satellite altimetry received electromagnetic radiation from the illuminated area within the footprint of the pulse-limited altimeter, so the variation of the footprint size influences the power received by the altimeter. For each specular reflector of sea surface, we use  $\zeta(\chi, \phi, t)$  to denote the height above the mean sea level. Here,  $\chi$  is the azimuth angle of the line connecting the altimeter and the nadir point,  $\phi$  is the colatitude which substitute off nadir angle  $\theta$  under the spherical earth assumption,  $t$  is two-way travel time of this specular reflector. Approximation to the first order, the sea surface height is the Gaussian distribution (also called normal distribution) whose probability density function with mean  $\mu$  and standard deviation  $\sigma_\zeta$  is shown in Equation (1.5). The average crest-to-trough height is called the significant wave height  $H_{1/3}$  which is 1/3 of the highest waves and is 4 times the standard deviation of the wave height distribution. So we have  $H_{1/3} = 4\sigma_\zeta$  (Fedor et al., 1979). If the sea surface height is symmetrically distributed ( $\mu = 0$ ), then the probability density function for the mean sea surface elevation is shown in Equation (1.6)

$$q_s(\zeta) = \frac{1}{\sigma_\zeta \sqrt{2\pi}} \exp\left(-\frac{(x-u)^2}{2\sigma_\zeta^2}\right) \quad (1.5)$$

$$\frac{4}{H_{1/3} \sqrt{2\pi}} \exp\left(-\frac{1}{2} \left(\frac{4\zeta}{H_{1/3}}\right)^2\right) \quad (1.6)$$

Due to the random nature of sea surface height, the instantaneous illumination pattern is probabilistic, the probability of illumination of specular reflector with  $\zeta(\chi, \phi, t)$  is

$$P = \int_{\zeta_1}^{\zeta_2} q_s(\zeta) d\zeta \quad \text{with } \zeta_1 = R_\phi - ct/2, \zeta_2 = R_\phi - c(t-\tau)/2 \quad (1.7)$$

Where  $R_\phi$  is the distance from the altimeter to mean sea level at  $\phi$ ,  $c$  is speed of light and  $\tau$  is the duration of pulse. From Equation (1.7) we can see the probability of illumination

depends on co-latitude  $\phi$  and time  $t$ . For Gaussian wave height with  $H_{1/3}=5\text{m}$ , the illumination reaches greatest at nadir at time  $t_{1/2}$  which is the time when the midpoint of the pulse reaches the mean sea level at nadir. The footprint size of the altimeter is defined by the 1% threshold illumination criterion, so the radius is where the probability of the illumination is larger than 1%. Using this definition, it was shown by Fu & Cazenave (2001) that evolution of the size and the area of the footprint of sea surface with Gaussian distributed height are very close to which of the monochromatic sea surface whose crest-to-trough wave height  $H_w$  is equal to  $H_{1/3}$ . So for the simplicity of illustration of the evolution of the size and area of the footprint from which the altimeter received the backscatter power, we use monochromatic sea surface as example in the explanation below.

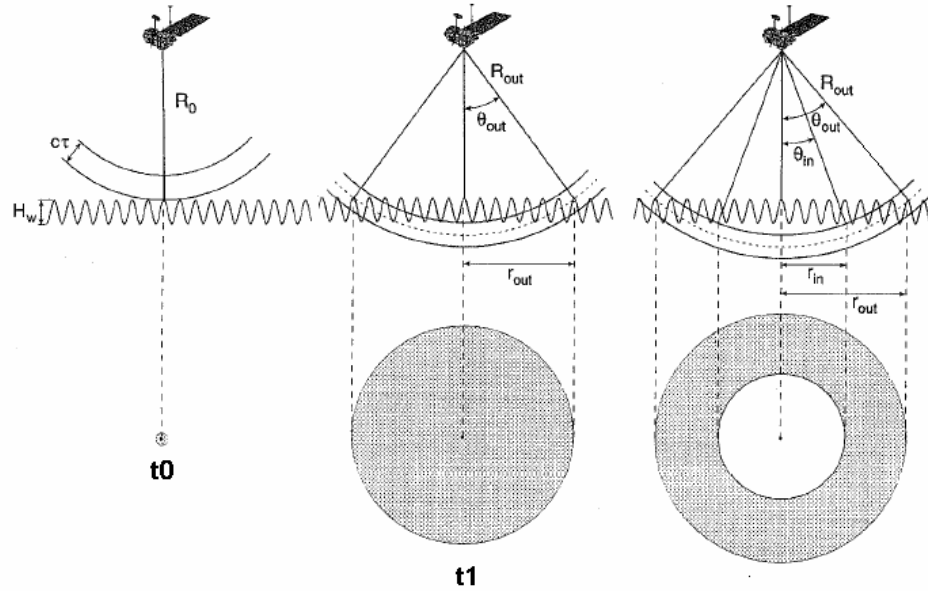


Figure 1.3: The evolution of footprint size of pulse-limited altimeter (Fu & Cazenave, 2001).

There are 2 critical times and the 2 associated stages in the evolution of the footprint size as shown in Figure 1.3. The first stage begins when the leading edge of the spherical expanding pulse hits the wave crest of the sea surface at the first critical time  $t_0/2$  with  $t_0$  being the time it takes for leading pulse which strikes the wave crest to return to antenna  $t_0 = 2(R - H_w)/c$ . After  $t_0/2$  the area of footprint increases, it was shown that the footprint radius (Chelton et al., 1989) is

$$r_{out}(t, H_w) \approx \sqrt{\frac{2R_0 \Delta R_{out}}{1 + R_0/R_e}} \quad (1.8)$$

Where  $R_0 = R - H_w / 2$ ;  $R_e$  is the radius of the earth;  $\Delta R_{out} = R_{out} - R_0$ . The time interval between  $t_0$  and the arrival time  $t$  of the pulse returned from the leading edge which hits the wave crest at off-nadir angle  $\theta_{out}$  is

$$\Delta t(H_w) = t - t_0 = \frac{2\Delta R_{out}}{c} \quad (1.9)$$

Put (1.9) into (1.8) we have

$$r_{out}(\Delta t, H_w) = \sqrt{\frac{c\Delta t R_0}{1 + R_0 / R_e}} \quad (1.10)$$

The area of the footprint from which the power is backscattered to altimeter is:

$$A_{out}(\Delta t, H_w) = \pi r_{out}^2 = \frac{\pi c \Delta t R_0}{1 + R_0 / R_e} \quad (1.11)$$

From (1.11), we can see the area of the surface backscatters the power to the altimeter increases linearly with the time interval between time of first returned microwave and the arrival time of the signal reflected from the wave crest at the off-nadir angle  $\theta_{out}$ , so the footprint remains the expanding circle in this stage.

The first stage ends when the trailing edge of the pulse intersects the wave trough at the second critical time  $t_1/2$  with  $t_1$  being the two-way travel time for the trailing edge of the pulse intersecting the wave trough as shown below:

$$t_1(H_w) = \tau + 2(R_0 + H_w) / c \quad (1.12)$$

At time  $t_1$ , the time interval between arrival time of the trailing edge reflected from the wave trough and the first arrival pulse is:

$$\Delta t_1(H_w) = t_1 - t_0 = \tau + 2H_w / c \quad (1.13)$$

From (1.13) the radius and the area of the footprint at time  $t_1$  could be computed as below

$$r_1(H_w) = \sqrt{\frac{c\Delta t_1 R_0}{1 + R_0 / R_e}} = \sqrt{\frac{(c\tau + 2H_w)R_0}{1 + R_0 / R_e}} \quad (1.14)$$

$$A_1(H_w) = \pi r_1^2 = \frac{\pi c \Delta t_1 R_0}{1 + R_0 / R_e} = \frac{\pi(c\tau + 2H_w)R_0}{1 + R_0 / R_e} \quad (1.15)$$

After time  $t_1/2$  the second stage begins, in this stage the elapsed time  $\Delta t > \Delta t_1$ , then radius and area of the inner illumination hole becomes

$$r_{in}(\Delta t, H_w) = \sqrt{\frac{c(\Delta t - \Delta t_1)R_0}{1 + R_0 / R_e}} = \sqrt{r_{out}^2(\Delta t, H_w) - r_1^2(H_w)} \quad (1.16)$$

$$A_{in}(H_w) = \frac{\pi c (\Delta t - \Delta t_1) R_0}{1 + R_0 / R_e} = A_{out}(\Delta t, H_w) - A_1(H_w) \quad (1.17)$$

From Equation (1.17) we get the area of the annulus from which the antenna received power is

$$A_{annulus} = A_{out}(\Delta t, H_w) - A_{in}(\Delta t, H_w) = A_1(H_w) \quad (1.18)$$

Equation (1.18) shows the area of the circle when the trailing pulse arrives at the wave trough only depends on the crest-to-trough height  $H_w$ . So the area of annulus in the second stage keeps the same for the monochromatic sea surface height due to fixed  $H_w$ , although the radius of the inner and the outer perimeter of the annulus continues to increase. Except  $H_w$ , the pulse duration  $\tau$  is the other parameter which affects the area of footprint. For TOPEX/POSEIDON with height of 1336km,  $\tau=3.125\text{nsec}$  ( $3.125*10^{-9}\text{sec}$ ), the diameter of annulus area increase from 2.0km to 9.6km when the sea surface changes from flat to monochromatic crest-to-trough wave height of 10m. Time  $t_{1/2}$  is defined to be the mid point between the time when the leading edge of the pulse returned to antenna from the wave crest at nadir and the time when the trailing edge of the pulse returned to antenna from the wave trough at nadir, from Equation (1.19) we can see  $t_{1/2}$  is the two-way travel time for the midpoint of the pulse to return from nadir mean sea level:

$$t_{1/2} \equiv \frac{t_0 + t_1}{2} = \frac{2R_0 + H_w}{c} + \frac{\tau}{2} = \frac{2R}{c} + \frac{\tau}{2} \quad (1.19)$$

The above is the description of the evolution of the area of the footprint of the satellite altimetry. Although footprint is important to the power backscattered to altimeter, it is not the determinant effect of the power. The area which determines the power received by the antenna is the illumination area within the footprint. The total illumination area at arrival time  $t$  is the integrated area of the specular scatters where the transmitted pulse intersects with the sea surface at time  $t/2$ . For the flat earth surface with  $H_w=0$ , the illumination area equals the area of the footprint. For the real sea surface, due to the complexity of the wave field in the footprint, the illuminated area for a particular pulse will be very noisy. To reduce the noise of the individual illuminated area, the averaged illuminated area is used. The details of the averaged illumination area are described in Brown (1977), Hayne (1980), Barrick and Lipa (1985), and Rodriguez (1988). The average of 1000 simulated independent time series of illuminated area for a Gaussian wave height distribution is shown in Figure 1.4.

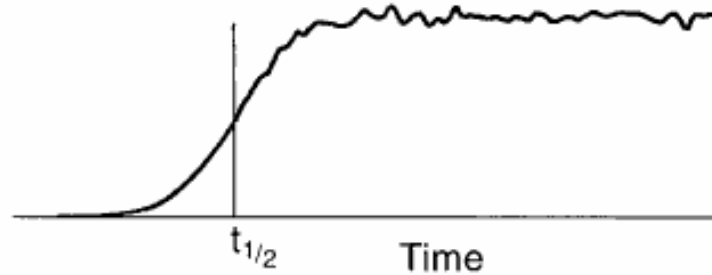


Figure 1.4: Average of 1000 simulated independent time series of illuminated area for a Gaussian wave height distribution (Townsend et al., 1981).

### 1.2.3 Waveform of Satellite Altimetry

As stated before, the illuminated area determines the returned power, however, it is not the only determinant factor. From Equation (1.1) we know the power of the returned signal also depends on the antenna gain pattern and backscatter coefficient. The dependence of the backscatter coefficient is eliminated by the implemented automatic gain control (AGC) loop in the electronics package, so the power is proportional to the illuminated area scaled by the antenna gain pattern Gain pattern  $G$ . From Moore and Williams (1957), the averaged illuminated area is

$$A_r(t) = A_r U(t - t_{1/2}) \otimes q_s(t) \otimes p_\tau(t) \quad (1.20)$$

Where  $\otimes$  denotes convolution,  $A_r$  is area of annulus footprint,  $q_s(t)$  is the probability density function for the sea surface height  $\zeta$  as shown in Equation (1.6) with  $t = \frac{-2\zeta}{c}$ ,

$$p_\tau \approx \left[ \frac{\sin(\frac{\pi}{\tau})}{\frac{\pi}{\tau}} \right]^2 \text{ it is the shape of the altimeter pulse, } U(t - t_{1/2}) \text{ is the unit step function,}$$

$$U(t - t_{1/2}) \equiv \begin{cases} 1(t \geq t_{1/2}) \\ 0(\text{otherwise}) \end{cases} \quad (1.21)$$

From (1.20), we have the power of the returned signal is

$$W(t) = W_{\max} P_{FS}(t) \otimes q_s(t) \otimes p_\tau(t) \quad (1.22)$$

$$P_{FS}(t) = G(t)U(t - t_{1/2}) \quad (1.23)$$

where  $P_{FS}$  is the radar impulse response for the flat sea surface on a spherical earth;  $W_{\max}$  is the power of the average signal output by the AGC at time  $t_1$  when the footprint becomes the annulus;  $G(t)$  decreases approximately exponentially with the increasing two-way travel time  $t$ , the details of the precise form of  $G(t)$  are discussed in Hayne (1980), Barrick and Lipa (1985) and Rodriguez (1988). The average time series of the returned power, called waveform, are shown in the Figure 1.5. The actual waveform fluctuated around the average lines. Figure 1.5 shows the waveform decreases approximately exponentially with the time although the illumination area remains the same as shown in Figure 1.4, this is due to the two-way antenna gain pattern  $G$  decrease exponentially. Because the returned power is proportional to the illumination area, so at the two-way travel time  $t_{1/2}$  the power is  $W_{1/2}$  which is the half power between the  $W_{\max}$  and the  $W_{\text{noise}}$ . By identifying the time of  $W_{1/2}$ , we get the two-way travel time  $t_{1/2}$ , using which we compute the altitude of the altimetry after correction for atmospheric and actual non-symmetric distribution of sea surface height distribution.

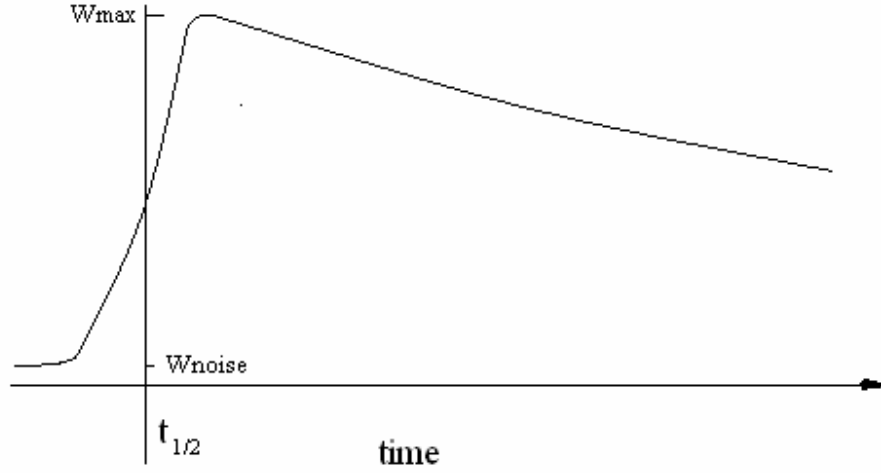


Figure 1.5: The average waveform of the returned signal.

As stated before the pulse duration  $\tau$  is short, this is accomplished by the radar range technique called pulse compression. The actual pulse with duration  $\tau'$  which is the same as the duration of the transmitted signal are processed (called deramped) by a spectral window to become equivalent to the signal received from transmitted signal with pulse duration of  $\tau$  which is the effective pulse duration of  $\tau$ ,

$$\tau = \Delta F^{-1} \quad (1.24)$$

where  $\Delta F = f_1 - f_2$ , it is the bandwidth of the transmitted pulse. Equation (1.24) shows the effective pulse duration depends on the bandwidth of the transmitted pulse not the actual duration  $\tau'$  of the transmitted pulse. For TOPEX/POSEIDON  $\tau = 3.125\text{nsec}$  corresponds to bandwidth  $\Delta F = 320\text{MHz}$  centered on 13.6Hz and 5.3Hz for Ku band and C band respectively. The details are described in the Ulaby et al. (1981), Chelton et al. (1989). From the derivation in Fu & Cazenave (2001), the waveform in spectral domain is similar to which in time domain, except the abscissa changes from time to frequency. To remove the aliasing effect caused by the frequency above the Nyquist frequency  $f_N$ , the received deramped signal passed through anti-aliasing filter to remove the frequency above the Nyquist frequency  $f_N$ , also called folding frequency.  $f_N$  is the period of the signal in the spectral domain, it could be computed as one half of the inverse sampling interval as shown below

$$f_N = \frac{1}{2\delta t'} \quad (1.25)$$

Where  $\delta t'$  is the sampling interval of the deramped signal. For TOPEX/POSEIDON the anti-aliasing filter has maximum frequency  $f_{\max} = f_N = 625\text{KHz}$ . Using Equation (1.25) we have the sampling interval of the deramped signal is  $\delta t' = 0.8\text{usec}$ , the actual transmitted pulse duration is  $\tau' = 102.4\text{usec}$ , so there is 128 samples of signal. By the onboard Fast Fourier

Transforming of the 128 samples of the deramped signal, the 128 samples of waveform uniformed spaced by  $\delta f' = 625000 * 2 / 128 = 9.766 \text{ KHz}$  in spectral domain are produced.

The waveform location of the signal generated from the hardware through the above described process varies with the variation of the sea-state conditions and the altitude of altimeter above the mean sea level. In order to maintain the leading edge of the returned waveform within a processing window, the onboard adaptive tracking unit (ATU) software is used to time the de-ramped signal to align the half power point of the leading edge of the waveform at a specific location (Bracewell, 1986). The half power point, also called tracking point, of the leading edge of waveform has frequency  $f_o$  in the spectral domain and has time  $t_{1/2}$  in time domain as described before.

The individual waveforms are noisy due to the randomness of the wave height field, so they are averaged within a track interval lasting about 50msec including 240 pulses to obtain the average waveform with reduced noise. This averaged waveform is analyzed by the onboard adaptive tracking unit (ATU) after the neighboring waveform samples are averaged into gates. For TOPEX/POSEIDON, the average of waveform samples 5-8 which is called "noise gate  $S_{noise}$ " is used to estimate the noise power in the background. The average of waveform samples 17-48 are called "AGC gate  $S_{AGC}$ " and  $S_{AGC} - S_{noise}$  are almost equal to the power at the midpoint of the leading edge. The accuracy of this estimation is independent on the precise alignment of the waveform because  $S_{AGC}$  is the average over large number of waveforms. By forming and analyzing the gates, ATU extracts the two-way travel time information from the waveforms. In addition, ATU generates 64 telemetry samples from 128 waveform samples for ground receiving stations. As shown in Figure 1.6, in the leading edge of the original waveform, the individual waveform samples are kept in the telemetry samples, while in waveform preceding and following the leading edge the 2 or 4 original waveform samples are combined into 1 telemetry sample to reduce the data rate.

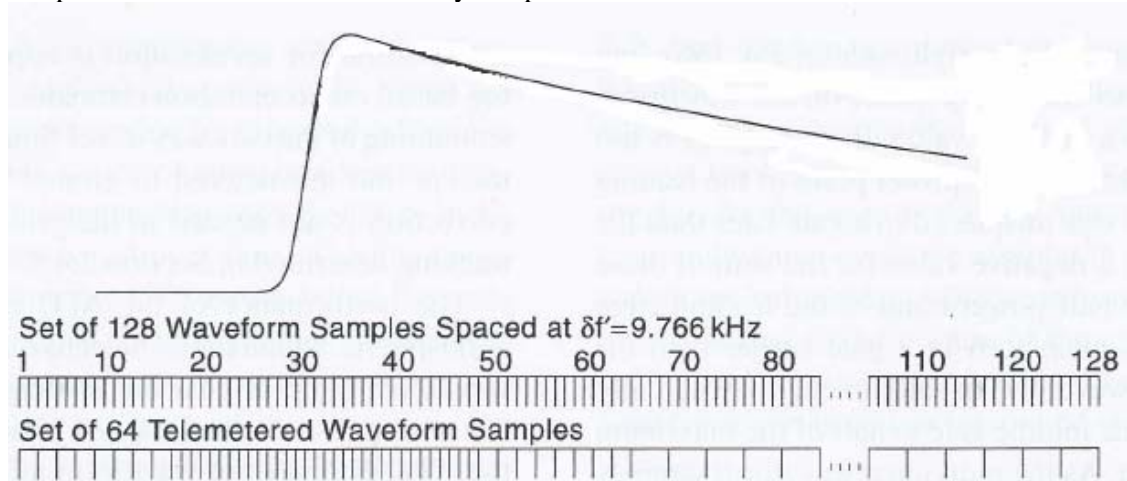


Figure 1.6: The generation of the 64 telemetered waveform samples transmitted to ground receiving stations from the 128 original waveforms in ATU (Zieger et al., 1991).

### 1.3 Summary of Chapters

Chapter 2 describes the satellite altimeter data used in the dissertation and the manipulation of the data. First the waveform over the inland water and the retracking methods are introduced. Following that, the method to estimate the range measurement and the high level database, called Stackfile, used to analyze the data are described briefly.

Chapter 3 demonstrates the methodology to detect the inland water. The algorithm is tested in the Manitoba and northwestern Ontario regions, the Amazon River Basin, and Southwest Taiwan. The retrieved satellite altimeter data is compared with the available in-situ stage measurement and the satellite altimeter data product from the other institutions. The amount of the detected body of water is compared with the mask produced from remote sensing techniques in Amazon River Basin. The backscatter coefficients in Canadian region, the Amazon River Basin and Southwest Taiwan are also analyzed.

Chapter 4 explores the application of the algorithm and the 10-Hz retracked data for the 1997 flood which covered the Red River Basin in North Dakota and Minnesota, the Missouri River Basin in North Dakota and South Dakota, the Minnesota River Basin and the Mississippi River Basin in Minnesota and Iowa. The retrieved data is compared with the in-situ stage measurement from USGS. The usage of the backscatter coefficient to detect the flood extent and snow coverage is explored. The results are compared with the USGS flood record.

Chapter 5 provides the conclusions for the studies.

## CHAPTER 2

### DATA PROCESSING

#### 2.1 Radar Altimeter Waveform Retracking Methods

The on-board altimeter software analyzes the obtained signal in several stages to suit different land surfaces automatically. In the first stage, the bandwidth of the transmitted signal is set to  $\Delta F = 5\text{MHz}$  for TOPEX/POSEIDON (Chelton et al., 2001). This bandwidth is narrow compared to the standard  $\Delta F = 320\text{MHz}$  as described in Chapter 1. From Equation (1.24) we know this narrow bandwidth causes the longer waveform sampling time resolution  $\tau$ , so the 128 waveform samples are sampled in a larger time span than standard time span of  $\tau = 3.125\text{nsec}$  (Chelton et al., 2001, Birkett, 1998). The signal received in the first stage is analyzed in the “coarse-tracking” mode using a simplified tracking algorithm, if the strength of the received signal and the position of the leading edge from the simplified tracking algorithm meet specific criteria programmed in the adaptive tracking unit software (ATU), the ATU will switch to the second stage of “fine tracking” mode with a full frequency sweep of  $\Delta F = 320\text{MHz}$  as described in Chapter 1. Otherwise, the satellite will track in the first stage of the “coarse-tracking” mode. It takes 1-3sec to initiate the fine-tracking mode, correspondingly, the data is lost within 6-20km. In the coarse-tracking mode, the range measurement over irregular terrain could be difficult to interpret because the leading edge of the waveform could be due to the rougher topographic features (or topography with higher slopes) away from the nadir points and the echo shape of the waveform changes with the variation of the inland water surface.

##### 2.1.1 Waveform of Inland Water

As described in Chapter 1, the waveform consists of three parts, the leading edge, the max peak, and the trailing edge. Over oceans, most returned waveforms are Quasi-Brown waveforms with a sharp, stable narrow peak, as shown in Figure 2.1a. However, over inland water the waveform is more complicated and related to the slope and roughness of the surface within the footprint. Waveforms from large lakes and wetlands are the typical high-powered spikes which is similar to signal returns over oceans (Birkett, 1995, 1998). As the

bodies of water become smaller, waveforms become broader and commonly exhibit multiple peaks (Koblinsky et al., 1993, Shum, 1995, Anzenhofer et al., 2000). Over land, the radar signal from the satellite is attenuated at the ground surface and thus provides weak power waveforms. The shape of the waveform changes with different inland water surface. Figure 2.1 shows 4 typical kinds of the waveform from ENVISAT over various inland water surface (Berry, 2005): Quasi-Brown model (Figure 2.1a), Flat Patch model (Figure 2.1b), Quasi-Specular model (Figure 2.1c), and complex model (Figure 2.1d). The proportions of the different waveforms over different water surfaces obtained from ERS-1 are shown in Figure 2.2 (Berry et al., 2005). The large Lake is defined to be the water with area  $> 4,000\text{km}^2$ , the medium lakes are water with area between  $500\text{km}^2$  and  $4,000\text{km}^2$  and the area of a small lake is less than  $500\text{km}^2$ . Figure 2.2 shows that although the Quasi-Brown waveform accounts for larger than 50% for the large lake and ocean, the flat-patch waveform becomes dominant for the small lakes and Amazon River Basin, the proportion of the Quasi-Specular waveform increases to similar to Quasi-Brown model waveform for the Amazon Basin.

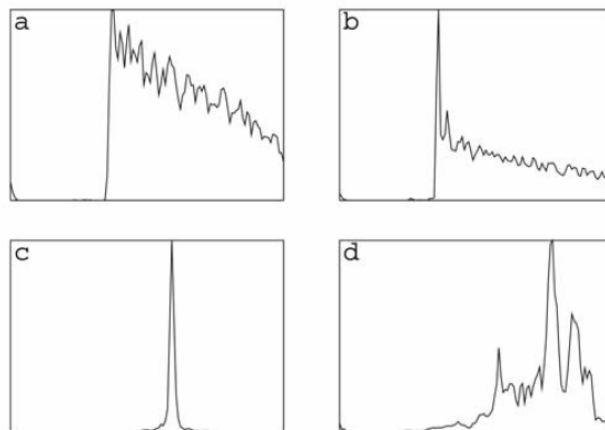


Figure 2.1: The typical waveform shape over inland water (Berry et al., 2005).

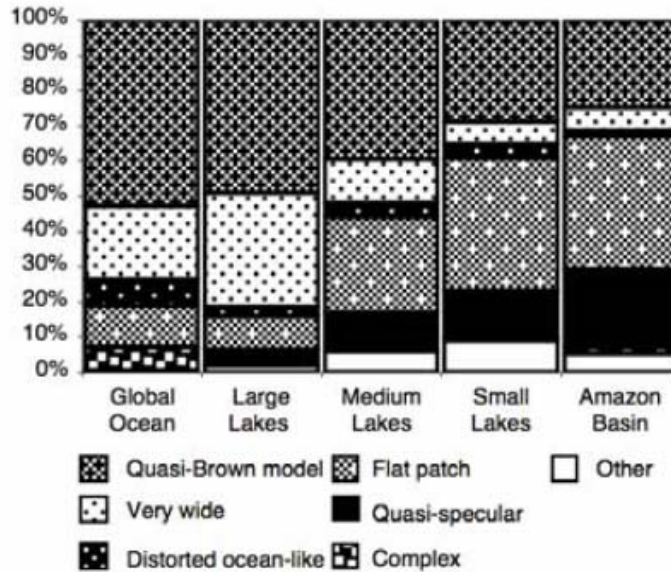


Figure 2.2: Distribution of the different waveform over different water surface (Berry et al., 2005).

Figure 2.1 and Figure 2.2 show the major difference between the waveform over ocean and over inland water is the time of the peak and the duration of the peak. The reasons for the peak difference are analyzed as below. As described in Chapter 1, the evolution of the returned power for each waveform depends on the reflectivity of the surface and the illuminated area. For oceans the power reaches the maximum at the time when the illuminated water area becomes the maximum, after that the illuminated area remains the same from the annulus footprint. So the returned power is stable after peak time although it decreases gradually due to the exponential decrease of antenna gain pattern. For large bodies of water, such as oceans and big lakes, the annulus footprint has the fixed area in the water, which causes the stability of the power after the peak time. However, the inner and outer perimeters of the annulus increase with time, which indicates the backscattered power is from the water area further away from the nadir point with the increase of the time. For the small body of water, the surface within the annulus footprint could become non-water when the inner and outer perimeters increase with time, which causes the sudden decrease of the reflected power because the power is backscattered from the non-water surface of low reflectivity. In other words, the stability of the power after the peak time in the ocean is because the water area is large enough to keep the power backscattered from the water when the radius of the footprint increases with the time, while the power is not stable if the water area is small. For the small body of water, the strength of the returned power is affected by the area of the illuminated water corresponding to the specific waveform sample time. Furthermore, because the power is the average of the individual noisy waveform, the possible difference between the individual noisy waveform could result in the variation of the strength of the power with the time. When there is water within the footprint, because the reflectivity of the water is normally higher than other land surface, the time of the peak is the time when

the returned power is backscattered from the water. Due to the uncertainty of the location of the water in the footprint when the body of water is small, the peak time varies from place to place. The existence of several peaks in the waveform could be because of waveform samples from the object at different height within footprint or because of the difference of the peak time between the individual noisy waveform used in averaging to produce the 10Hz waveform.

As illustrated above, waveform from non-ocean surface is different from waveform from ocean surface and it alters in time and region. In order to generate the accurate range estimation the ground based re-processing of the waveform, called retracking, is required for non-ocean surface. For TOPEX/POSEIDON, altimeter data is delivered from GDR (Geographic Data Record) as 1-Hz products, 1 measurement per second, it does not contain the non-ocean height data. However, the information of the non-ocean height could become available through the sophisticated retracking process using the raw waveform data collected from satellite altimetry. The waveform data which has the most detailed information provided by altimeter is 10-Hz measurements, 10 measurements per second, obtained from sensor data records (SDR) products of altimeter. The ground spacing between each waveform is about 660m. Figure 2.3 shows the example of 10-Hz waveform from TOPEX over the Pantanal wetland (Figure 2.3a) and over Amazon River (Figure 2.3b) (Birkett, 1998), the echo shapes of the waveform are Quasi-specular (Figure 2.1c) and Flat-patch (Figure 2.1b). These two kinds of waveforms are dominant over the small lake and river basins as shown in Figure 2.2. Figure 2.3a is the waveform at the time of maximum water level. Figure 2.3b is the waveform at the time of minimum water level, the last 3 waveforms have several peaks at different time. The multiformity of the 10 waveforms in Figure 2.3b indicates the importance of investigating the individual 10-Hz data to improve the quality and quantity of the measurement of the inland water, which will be proved in Chapter 3 and Chapter 4.

For the retracking analysis of the 10-Hz measurement, the data amount involved is ten times larger and processing is time-consuming. Due to the complexity and data intensity of the retracking, the research in this topic has been done only piecewise and for a restricted time despite of its significance for the inland water study. In this dissertation the 10-Hz waveform is analyzed by the retracking algorithm (Lee et al., 2008, Anzenhofer et al., 2000) to re-compute the surface elevation for the inland water, and the importance of the 10-Hz retracked measurement is compared with 1-Hz non-retracked data for inland water study in Chapter 3 and Chapter 4.

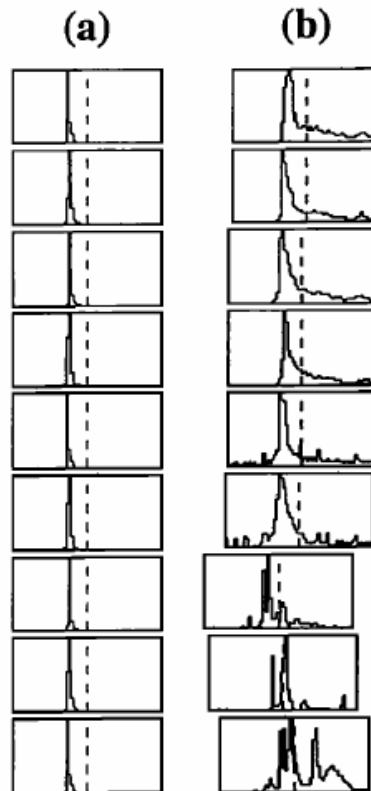


Figure 2.3: The example 10Hz waveform over the Pantanal wetland (a) and the Amazon river (b) (Birkett, 1998).

### 2.1.2 Retracking Methods

To process the waveform over non-ocean surfaces, several retracking algorithms have been developed. The first retracking algorithm was developed by Martin et al. (1983) to process the waveforms from the continental ice-sheet. This algorithm is called the NASA  $\beta$  retracker. After that, Mullard Space Science Laboratory (MSSL) initiated the Offset Center of Gravity (OCOG) algorithm to account for the effect of the topography in radar response (Rapley et al., 1987, Bamber, 1994). Due to the effect of volume scattering in addition to the influence of the surface scattering on the waveform over ice-sheet (Davis, 1993), Davis developed the S/V algorithm and threshold algorithm (Davis, 1995, Davis, 1996). Different algorithm suits for different waveform returned from the varying type of non-ocean surface. Here we describe briefly the 3 popular algorithms: NASA  $\beta$  retracker, OCOG retracker, and threshold retracker.

NASA  $\beta$  retracker use 5 and 9 parameters, called  $\beta$  coefficients, for the single ramp and the double ramp waveform respectively, each single ramp in the waveform represents a

distinct sharp rise in the returned power. The single ramp waveform model with linear trailing edge is analyzed using Equation (2.1).

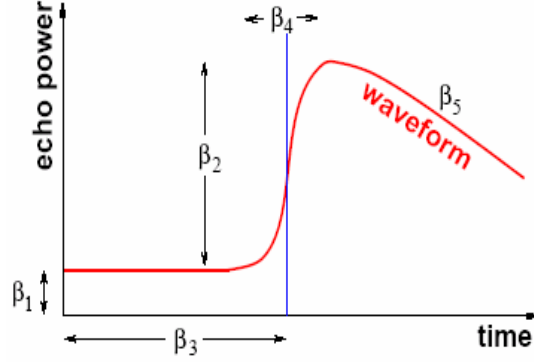


Figure 2.4: The waveform model for the NASA 5  $\beta$  retracker (GeoForschungsZentrum Potsdam, 1998).

$$y = \beta_1 + \beta_2(1 + \beta_5 Q)P\left(\frac{t - \beta_3}{\beta_4}\right) \quad (2.1)$$

$$\text{Where } P(z) = \frac{1}{\sqrt{2\pi}} \int_{-\infty}^z e^{-\frac{q^2}{2}} dq, q = \frac{t - \beta_3}{\beta_4} \quad (2.2)$$

$$Q = \begin{cases} 0, & \text{if } t < \beta_3 + 1/2\beta_4 \\ t - (\beta_3 + 1/2\beta_4) & \text{if } t \geq \beta_3 + 1/2\beta_4 \end{cases} \quad (2.3)$$

The least squares method could be used to estimate the 5  $\beta$  coefficients in Equation (2.1) after obtaining the samples of waveforms. The physical meaning of these coefficients are listed below:  $\beta_1$  is the thermal noise of the waveform to measure the background noise;  $\beta_2$  is the waveform amplitude which could indicate the surface properties with different reflectivity;  $\beta_3$  is the mid-point of the leading edge which corresponds to the two-way travel time used to compute altimeter range;  $\beta_4$  is the slope of the leading edge which is related to significant wave height described in Chapter 1, the smaller the significant wave height, the bigger the slope is. Equation (2.1) assumes the trailing edge in Figure 2.4 is linear, to simulate the antenna attenuation which decreases exponentially, the E-tracking method is used as shown in Equation (2.4).

$$y = \beta_1 + \beta_2 e^{-\beta_5 Q_1} P\left(\frac{t - \beta_3}{\beta_4}\right) \quad (2.4)$$

$$\text{Where } Q_1 = \begin{cases} 0, & \text{if } t < \beta_3 + k\beta_4 \\ t - (\beta_3 + k\beta_4) & \text{if } t \geq \beta_3 + k\beta_4 \end{cases} \quad (2.5)$$

In Equation (2.5),  $k$  is a weight factor which could be adjusted for the return echo and is set to 2. The double ramp waveform model is used when there is distinct height change or discontinued body of water within the footprint, the details are described in (GFZ, 1998).

Offset Center of Gravity (OCOG) retracker constructs a rectangle whose area is equal to the total area under the waveform, the height of the rectangular is the amplitude of the power. The width of the rectangular box combined with the center of gravity (COG) of the box are used to determine the position of the leading edge, which represents the two-way travel time used to estimate altimeter range. The computation is illustrated in Figure 2.5 and Equation (2.6)-(2.9).

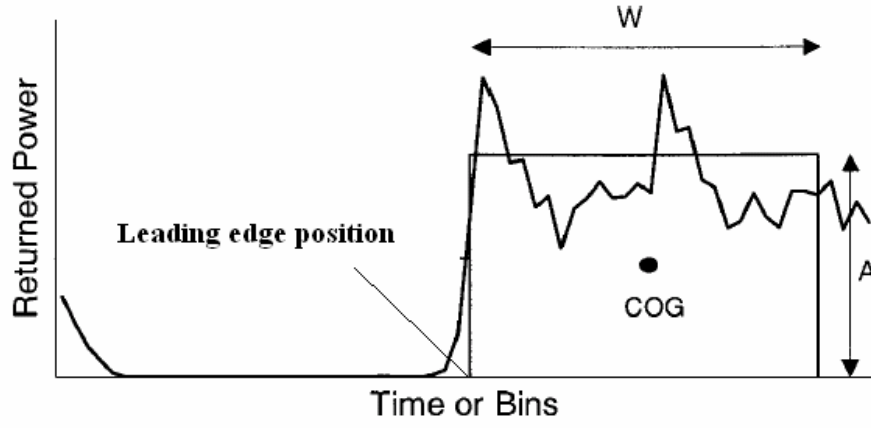


Figure 2.5: Illustration of the OCOG Retracker.

$$\text{Leading edge position } \beta_3 = \text{COG} - W/2 \quad (2.6)$$

$$\text{Position } \text{COG} = \frac{\sum_{n=1+n_a}^{64-n_a} nR^2(n)}{\sum_{n=1+n_a}^{64-n_a} R^2(n)} \quad (2.7)$$

$$\text{Width } W = \left( \frac{\sum_{n=1+n_a}^{64-n_a} R^2(n)}{\sum_{n=1+n_a}^{64-n_a} R^4(n)} \right)^2 \quad (2.8)$$

$$\text{Amplitude: } A = \sqrt{\frac{\sum_{n=1+n_a}^{64-n_a} R^4(n)}{\sum_{n=1+n_a}^{64-n_a} R^2(n)}} \quad (2.9)$$

In Equation (2.6)-(2.9),  $n$  is the bin number;  $R(n)$  is the returned power at bin # $n$ ,  $n=45-50$  are excluded to avoid leakage effect for TOPEX/POSEIDON (Lee et al., 2008, Hayne et al., 1994);  $n_a$  is the number of aliased bins at the beginning and end of the waveform,  $n_a=4$  for

TOPEX/POSEIDON. The effect of low amplitude samples in front of the leading edge could be reduced by computing squares of the sample values (Bamber, 1994).

Following the OCOG retracker, the threshold retracking method is developed specially to measure the ice-sheet elevation change (Davis, 1996). It defines the tracking gate as the time when the returned power satisfies a particular threshold percentage of the maximum returned power. The computation is illustrated in Figure 2.6 and Equation (2.10)-(2.13).

$$\text{Waveform Amplitude } A_{\max} = \max(R(n)) \quad (2.10)$$

$$\text{Thermal noise } DC = \frac{1}{3} \sum_{n=5}^7 R(n) \quad (2.11)$$

$$\text{Threshold level } TL = DC + Tcoeff(A_{\max} - DC) \quad (2.12)$$

$$\text{Tracking gate } \beta_3 = (\hat{n} - 1) + \frac{TL - R(\hat{n} - 1)}{R(\hat{n}) - R(\hat{n} - 1)} \quad (2.13)$$

Where  $n$  is the bin number;  $R(n)$  is the returned power at bin # $n$ ;  $Tcoeff$  is the percentage of the maximum power returned from surface;  $\hat{n}$  is the location of the first gate exceeding the threshold level. For Equation (2.13) when  $R(\hat{n}) = R(\hat{n} - 1)$ ,  $\beta_3 = \hat{n} - 1$ . In Equation (2.11), gates below 5 are excluded due to the aliasing effect in gate 1-4 for TOPEX/POSEIDON. Also similar to the OCOG retracker, gate 45-50 and gate 60-64 are excluded for the spectral leakage problem in the computation. Usually the threshold is 50% for the ocean and 10% for the ice-sheet (Berry et al., 2005).

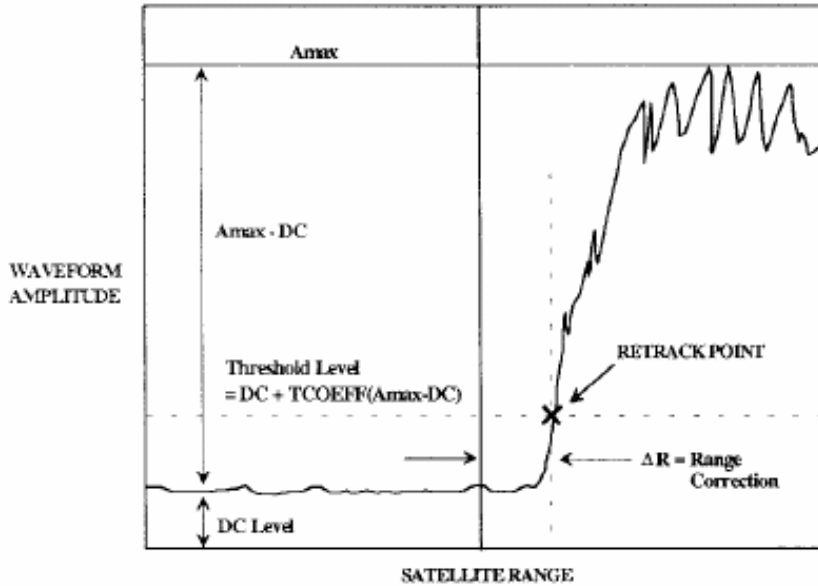


Figure 2.6: The illustration of threshold retracker (Davis, 1996).

From the above description, we know the common goal of all retracker is to compute  $\beta_3$  which is the location of the corrected tracking gate and represents 2-way travel time used to compute the altimeter range. The retracked  $\beta_3$  is then used to estimate the range correction ( $dr$ ) by multiplying the difference between  $\beta_3$  and the onboard tracking point, 24.5 for TOPEX/POSEIDON, with the distance  $ds$  which represents the range difference caused by single gate offset as shown in Equation (2.14) where  $t_k$  is single bin pulse width and  $C=299792458\text{m/s}$  is the velocity of light.

$$\begin{aligned} dr &= (\beta - 24.5) * ds = (\beta - 24.5) * t_k * C / 2 \\ &= (\beta - 24.5) * 3.125 * 10^{-9} * 299792458 \\ &= (\beta - 24.5) * 0.4684 \end{aligned} \tag{2.14}$$

The retracked range is obtained by adding the range correction to the original on-board range estimation. In this dissertation, we will compare the measurements obtained from the OCOG retracker, 10% threshold retracker, 20% threshold retracker and 50% threshold retracker.

## 2.2 Data Description

In this dissertation, we will use data from TOPEX/POSEIDON primarily for demonstration purposes. The methodology is developed to use any or multi-mission satellite radar altimetry over small bodies of water. TOPEX/POSEIDON is the National Aeronautics and Space Administration and Centre National d'Etudes Spatiales (NASA-CNES) joint mission dedicated to study ocean dynamics. TOPEX/POSEIDON is the first satellite carrying two altimeters including the NASA dual-frequency altimeter and the CNES solid-state (single frequency) altimeter (SSALT), operating at 5.3GHz and 13.65GHz respectively. TOPEX/POSEIDON has a repeat cycle of period 9.999 (solar) days and has equator cross track spacing of  $\sim 315\text{km}$ . For each cycle, the satellite made 254 descending passes and 254 ascending passes with global coverage ranging from 66 S to 66 N. The mean orbit height is 1,336km. Previously, TOPEX/POSEIDON was used for ocean study, thus the data over continents are not fully used except for large lakes and rivers. In this dissertation we will explore the usage of inland data for small bodies of water. The two NASA and SSALT altimeters cannot operate simultaneously, SSALT only covers the 10% and it does not operate over rivers and wetlands. So we only consider NASA dual-frequency altimeter data which are more accurate than the single-frequency SSALT. Products available from TOPEX/POSEIDON include the Geophysical data records (GDR) and the sensor data records (SDR). GDR data are post processed data from raw data. It is used for most applications and includes the geophysical information as well as instrumental information to improve the accuracy of the measurements. There are two kinds of GDR data set, one is from the NASA Physical Oceanography Data Center (PODAAC). The other is from the CNES Archiving, Validation, and Interpretation of Satellite Data in Oceanography (AVISO) data center. In this study, we primarily used the GDR and SDR data from PODAAC. The SDR provides waveforms at a rate of 10-Hz delivered approximately every 680m, 0.1s (or 10-Hz). The waveform samples are distributed in a window of 128 bins at 3.125nsec time interval. We will combine the information only available from the GDR, such as the accurate satellite orbit and geophysical corrections, with the NASA altimeter's waveforms which is the

information only available from SDR to obtain the 10-Hz retracked height value at higher resolution and higher accuracy.

## 2.3 Range Estimation

Satellite altimetry obtains the water level ( $h$ ) from the measurement of the range ( $R$ ) which is the distance between the altimeter and water surface using Equation (2.15)

$$h=H-R \quad (2.15)$$

where  $H$  is the given orbit height of the satellite relative to a reference ellipsoid, water level  $h$  is defined as height of water surface relative to the reference ellipsoid which is TOPEX reference ellipsoid with equatorial radius of 6378.1363km and a flattening coefficient of 1/298.257 in this dissertation. The approximation of the range ( $R$ ) is computed as Equation (2.16)

$$\hat{R} = ct / 2 \quad (2.16)$$

where  $c$  is the free-space speed of light and  $t$  is the two-way travel time described in Chapter 1. In reality, the transmitted pulse travels though the atmosphere, although at the chosen microwave frequency the power attenuation caused by the atmosphere is minimum, the speed of pulse is still reduced by atmosphere resulting the computed range is longer and thus the corresponding water level is lower than the real value. For TOPEX/POSEIDON, Chelton et al. (2001) shows the correction for the dry gas component of dry troposphere is the most significant adjustment with the value 226cm from the European center for Medium Range Weather Forecasting (ECMWF); the water vapor and the cloud liquid droplet both contribute to the refraction of the wet troposphere with the ECMWF correction about 24cm at latitude lower than 30° and 10cm at latitude higher than 30°; the free electrons in the ionosphere cause the range correction of 12cm at lower latitude and 6cm at higher latitude. Besides the atmospheric corrections, for the deep ocean study there are tidal corrections including the ocean tide, pole tide, solid earth tide; instrument corrections such as oscillator drift, Doppler shift; and sea-state bias correction etc.

In the dissertation we use ECMWF wet and dry troposphere correction and the DORIS (Doppler Orbitography and Radiopositioning Integrated by Satellite) ionospheric correction. The TMR (TOPEX Microwave Radiometer) wet tropospheric correction and the TOPEX-dual frequency ionospheric correction is not chosen for inland water application due to their invalidity over continent (Birkett, 1995). Different from ocean application, there is no correction for ocean tide. Since the expected wave height are less than 10cm for inland water, the effect of electro-magnetic bias which exist only for the ocean wave field are ignored (Birkett, 1998). In addition, the inverse barometric correction used in the ocean study is not applied here because the body of water is relatively small compared with the atmospheric system. From above, we obtain the satellite altimeter range  $R$  using Equation (2.17)

$$R = \hat{R} - \Delta R_{pole\ tide} - \Delta R_{solid\ earth\ tide} - \Delta R_{wet\ troposphere} - \Delta R_{dry\ troposphere} - \Delta R_{ionosphere} - \Delta R_{instrument} \quad (2.17)$$

Where  $\hat{R}$  is computed from Equation (2.16), and  $\Delta R$  s are range corrections with corresponding factor shown in the subscript.

## 2.4 The Satellite Altimeter Stackfile Database

In this dissertation, decadal TOPEX/POSEIDON data has been reorganized to a high-level product called a “Stackfile” to take the advantage of repeat track property of satellite track. It is a compact database structure for convenient access to altimetry data including state-of-the art corrections and models (Kruizinga, 1997; Yi, 2000).

Most satellite altimetry missions have been flown in repeat orbits. That is, the satellite flies over the same geographic location after one repeat period. Stackfile makes use of the repeating nature of the ground track. The altimeter measurements are reorganized per geographic location. It is actually a database composed of 2-dimensional bins, each bin represents a particular geographic location. The first dimension is addressed by row number which indicates the distance away from the equator for the location. The second dimension is addressed by the column number which indicates the pass no. and thus could provide the information of the equator-crossing longitude of the pass. The repeated measurements at a particular location are stacked into the same bin in the order of cycle, each cycle corresponds to a particular time. Given the fixed row and column, bins contain all the information from all the repeat cycles measured over a particular area of the earth. The illustration of Stackfile is shown in Figure 2.7.

Figure 2.7 shows the surface height is “stacked” in time for each geographic location. The time-ordered surface height data is divided into ascending and descending passes, so there are descending Stackfile and ascending Stackfile with the same structure. The ascending pass is the orbital revolution along which the satellite moves from its most southern latitude to the most northern latitude. The descending pass is another half of orbital revolution along which the satellite moves from its most northern latitude to the most southern latitude. Data are stored into bins approximately 1 second of time long along the satellite ground tracks for 1-Hz Stackfile database, the size of each bin is 6.8km\*2km for TOPEX/POSEIDON.

There are 5 basic steps involved in building the structure of a Stackfile as illustrated in Figure 2.8. In the first step, the data were divided into descending and ascending passes. In Step 2, the chosen ascending (or descending) pass was divided into bins using the time spacing ( $\Delta T$ ) of the height measurement. In Step 3, for the chosen ascending (or descending) pass, the row number of each bin is computed using the difference between the time of the height measurement and the equator crossing time of the same pass ( $T_{asc}, T_{eqAsc}$ ). After that, the column number for the fixed pass is computed using the equator crossing longitude of the pass ( $\lambda_{eqAsc}$ ) and the first ascending equator crossing longitude after the prime meridian ( $\lambda_{eqAsc0}$ ). Finally, the slot number is computed using the equator crossing time of the ascending pass in cycle 1 ( $T_{eqAsc0}$ ) and  $T_{eqAsc}$ .

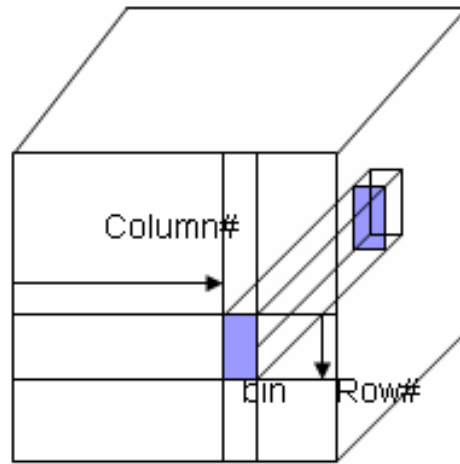


Figure 2.7: The structure of the conceptual 3-dimensional Stackfile.

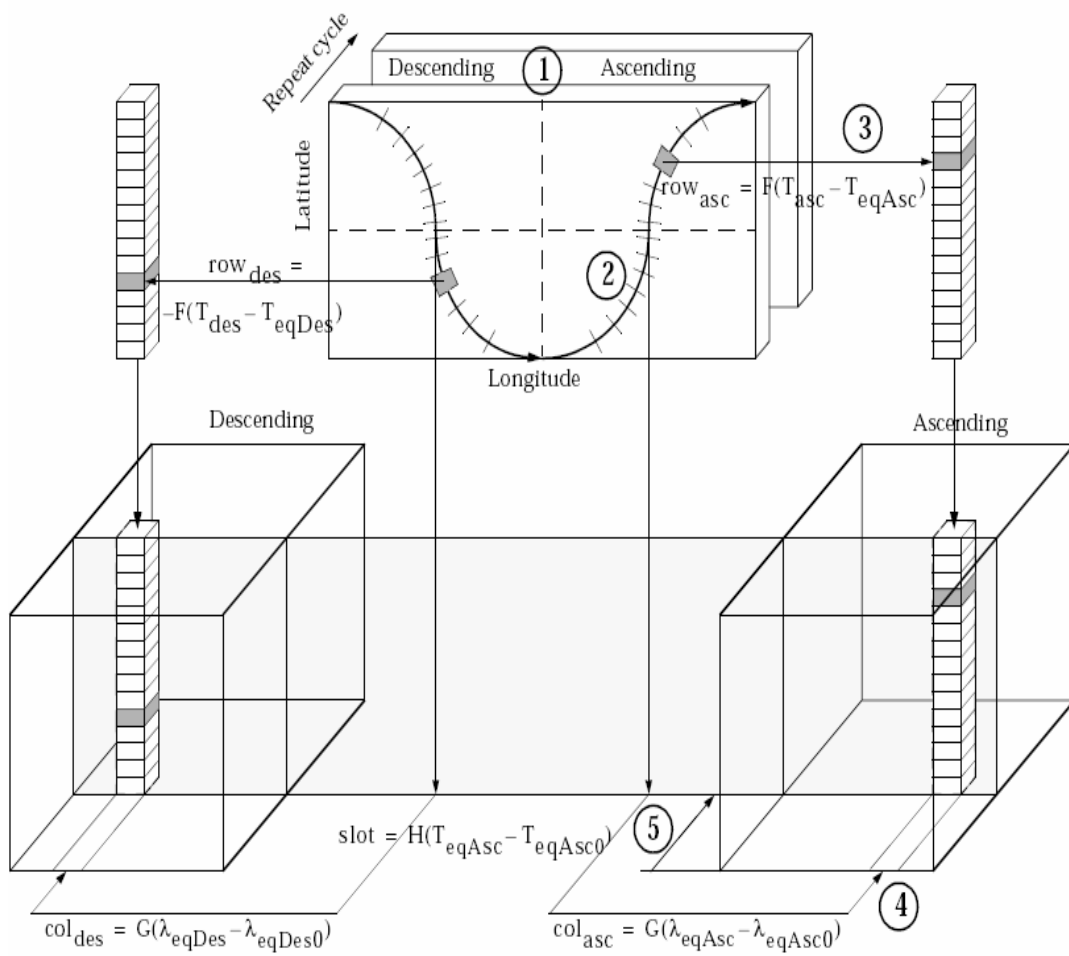


Figure 2.8: The illustration of the procedure to build the structure of conceptual Stackfile (Kruizinga, 1997).

To provide the 10-Hz retracked data, the original 1-Hz Stackfile database is expanded to the 10-Hz Stackfile (Lee et al., 2008). As shown in Figure 2.9, in the built skeleton Stackfile database, the procedure begins within a fixed column. In that column the 10-Hz rate longitude and latitude (Lee et al., 2008) are computed for each row. Following that, iterations are carried out for all cycles in a given pass to search the record which provides the same row number as the given row number from the TOPEX/POSEIDON GDR data. For that specific record in the given cycle and pass we extract all the geophysical information to prepare for the retracking process. After that, the 10-Hz time tag, the actual ground tracks and the retracked height are computed using the information from TOPEX/POSEIDON SDR data which has the same pass and cycle as TOPEX/POSEIDON GDR.

For the large volume of the altimeter data, this reorganization allows for a very efficient access to the altimetry data required for the repeat track and crossing arc analysis. The Stackfile database forms an integral part in the linking of the multiple satellite missions, because its organization allows for efficient access to multiple altimeter datasets for a given location. The methods of building the Stackfile and accessing the stored data are described in Yi, 2002 and Lee et al., 2008.

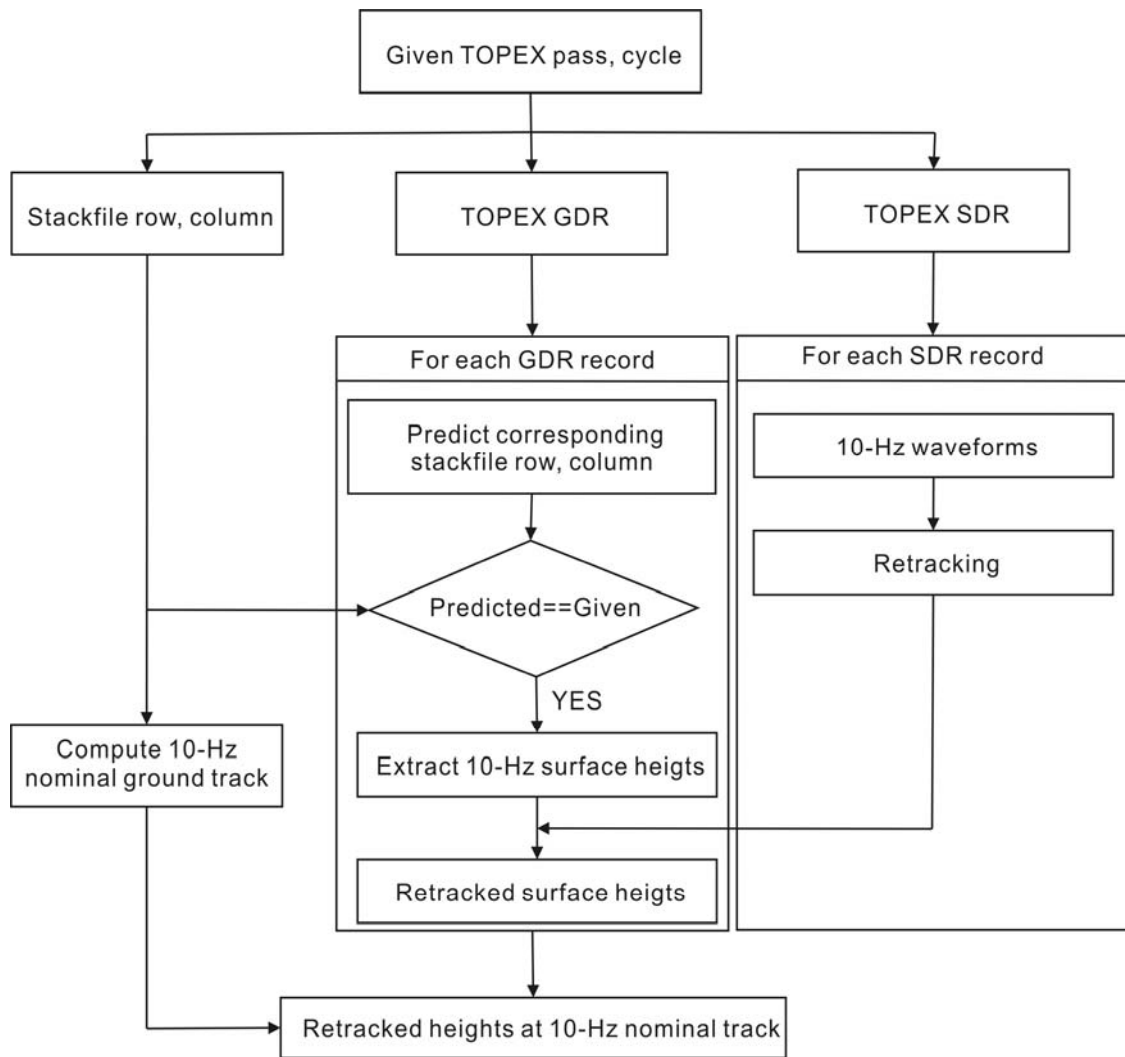


Figure 2.9: The procedure of producing the 10-Hz retracked data (Lee et al., 2008).

## CHAPTER 3

# VALIDATION OF THE WATER-DETECTION ALGORITHM

### 3.1 Water-Detection Algorithm Description

One of the challenges in this study is to observe or to predict land-surface characteristics using the satellite data. In particular, there is a need for robust classification between water and non-water regions using satellite radar altimetry data. Prior to this work, the procedure to accomplish this task included investigation of land cover characteristics using satellite image or existing land cover maps, retrieving the satellite data at the candidate points, and investigating the validity of the measurement at the candidate points manually. This procedure is extremely time-consuming and makes it practically impossible for large scale study. Moreover, the dependence on the a priori information of land properties from maps/masks could result in the loss of valuable measurement of the bodies of water, which are not valid in the map/masks to be classified as water bodies, due to the limitation of the resolution or due to the inappropriate collecting time of the map, or both. For example, in the Amazon region, there is a body of water with seasonally varying extents and not detectable by satellite optical image as “water”, but is verified by the detailed in situ hydrological map as will be shown in this dissertation. Even using high-resolution Amazon mask (dual-season masks) developed by L-band SAR (Hess et al., 2003), as it will be shown in this dissertation, could miss water classifications presumably because of the more frequent fluctuations of inundation extents, which may happen more than twice a year. In this dissertation, the algorithm is developed and tested towards semi-automatically detect water and extract surface water height measurements over relatively small inland bodies of water.

To find the measurement over water, all of the available bins in the Stackfile are first checked automatically to select the locations where the satellite altimeter data is available within the given area. Each bin represents a specific location for a particular 1-Hz data as described in Chapter 2. Then within each selected bin, the data are further organized into groups by their 10-Hz number from 1 to 10 denoting the first to the tenth 10-Hz data within the bin. Thus, each 1-Hz bin is divided into ten locations corresponding to 10-Hz data. For each of the 10-Hz locations, data from all cycles are analyzed. The interval between each cycle is 10 days, and thus for ten years there are about 360 cycles to analyze a particular 10-

Hz location. Three iterations are carried out consecutively to select the location as described below.

In the first iteration, the measurements with missing or extremely large height value, or the backscatter coefficient  $\sigma_0 < 5dB$  (Birkett, 2000) are edited. Following that, the mean value is computed to prepare for the standard deviation computation in the next step. In the second iteration, for each fixed location the difference between the mean and the data of each cycle is computed, then the proportion of the data with difference smaller than M1 is investigated for the same location. We select the location if the proportion is larger than N1 and the standard deviation of data from all cycles is smaller than S1. In the third iteration, the proportion of the data with difference smaller than M2 is investigated for each fixed location, and we select the location if the proportion is larger than N2. Finally, the locations whose time series show good seasonality are selected. The details of the procedure are shown in Figure 3.1. The suggested parameter values (M1, N1, S1, M2, N2) are listed in Table 3.1. These values have been chosen to optimally select over-water altimetry data for the three study regions in this Chapter: the Manitoba and southwestern Ontario region, the Amazon basin, and the southwestern Taiwan region, and for the study of the 1997 Red River Flood in Chapter 4.

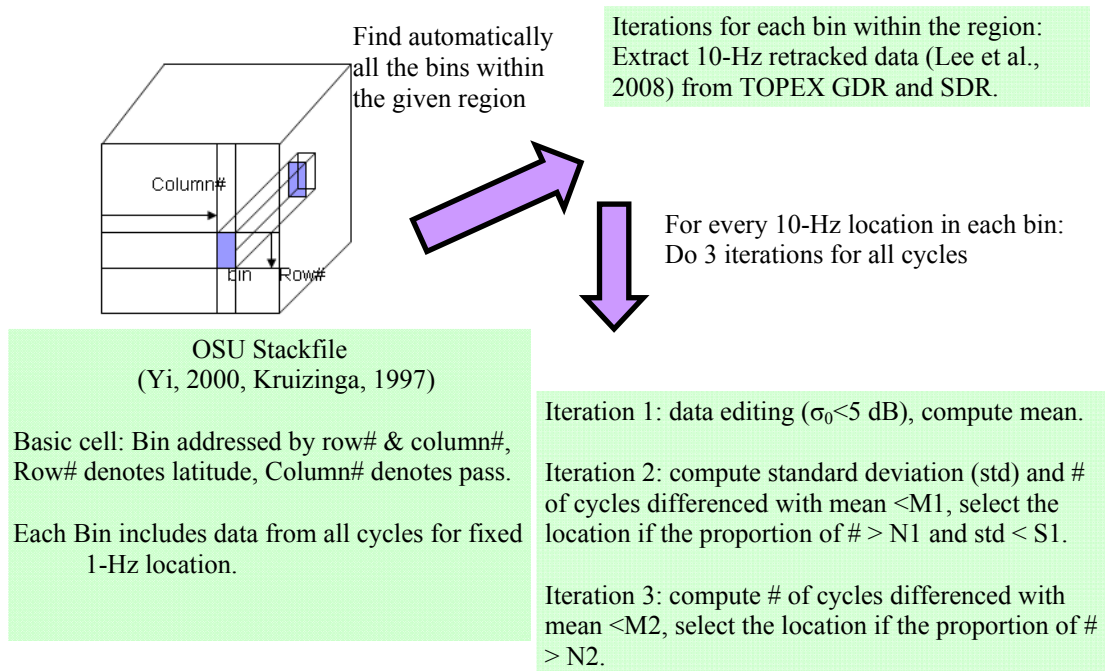


Figure 3.1: Water-Detection Algorithm Flow-chart.

Parameter	N1	N2	M1	M2	S1
Value	38%	68%	20m	2m	4m

Table 3.1: Suggested parameter values used in the water-detection algorithm.

Following the establishment of the algorithm, we then apply the algorithm to three different study regions: the southwestern Hudson Bay land region (Manitoba and southwestern Ontario), the Amazon River Basin and the Southwestern Taiwan. The retrieved TOPEX water level time series are compared with the available in situ stage gauge measurements from the USGS, ANA Brazil, Environment Canada as well as high-level radar altimeter derived water height data products from LEGOS and USDA. The performance of the algorithm for water-point detection are then compared with the results using masks obtained by L-band JERS-1 SAR data over the Amazon River Basin (Hess et al. 2003), along the TOPEX/POSEIDON ground tracks.

### 3.2 Manitoba and SW Ontario

In Saskatchewan, Manitoba and Ontario, most of snow melt and freshwater are transported from the Nunavut region of Canada (northwest of Hudson Bay), which is covered by snow 8 to 9 months every year, as a result of net transport of freshwater from the north (Ingram and Prinsenberg, 1998, Stewart, 2000). Here, we study the small inland bodies of water in Manitoba and SW Ontario and present example points in the small inland bodies of water detected by the algorithm. To assess the accuracy of the satellite altimetry measurement, we first retrieved the TOPEX data at the locations where the stage measurements are available for a validation study. The retrieved water level measurements, located in large Lakes in Manitoba and SW Ontario (primarily because of the availability of gauge data in large lakes and rivers), are compared with the gauge measurements from Environment Canada (<http://scitech.pyr.ec.gc.ca/waterweb>). We investigated both the retracked and non-retracked TOPEX altimetry water level measurements in the regions containing numerous small bodies of water in Manitoba and Ontario. We also compared our retrieved data with data available from other investigators, including LEGOS, USDA & NASA/GSFC and CASH. After that, we studied 10-Hz Automatic Gain Control (AGC) and retrieved water height measurement for the smaller body of water where the stage measurements are not available. The locations of the points are shown in Figure 3.2 and Table 3.2. In Figure 3.2, the big red circles denote the TOPEX altimeter data locations used in the comparison, the purple triangles are the available stage gauges used for the comparison, the red points are detected bodies of water along the satellite tracks, and the small purple box denotes the region used to study the 10-Hz AGC and the retrieved height measurement for the small body of water.

	T O P E X d a t a		G a u g e d a t a	
	Longitude	Latitude	Longitude	Latitude
Reindeer Lake	258.3661	57.8550	258.3333	57.8806
Cedar Lake	259.8181	53.2113	259.8539	53.9394
Lake of Woods	264.9846	49.0674	265.1906	49.7102

Table 3.2: Coordinates of the example points in lakes in Manitoba and SW Ontario.

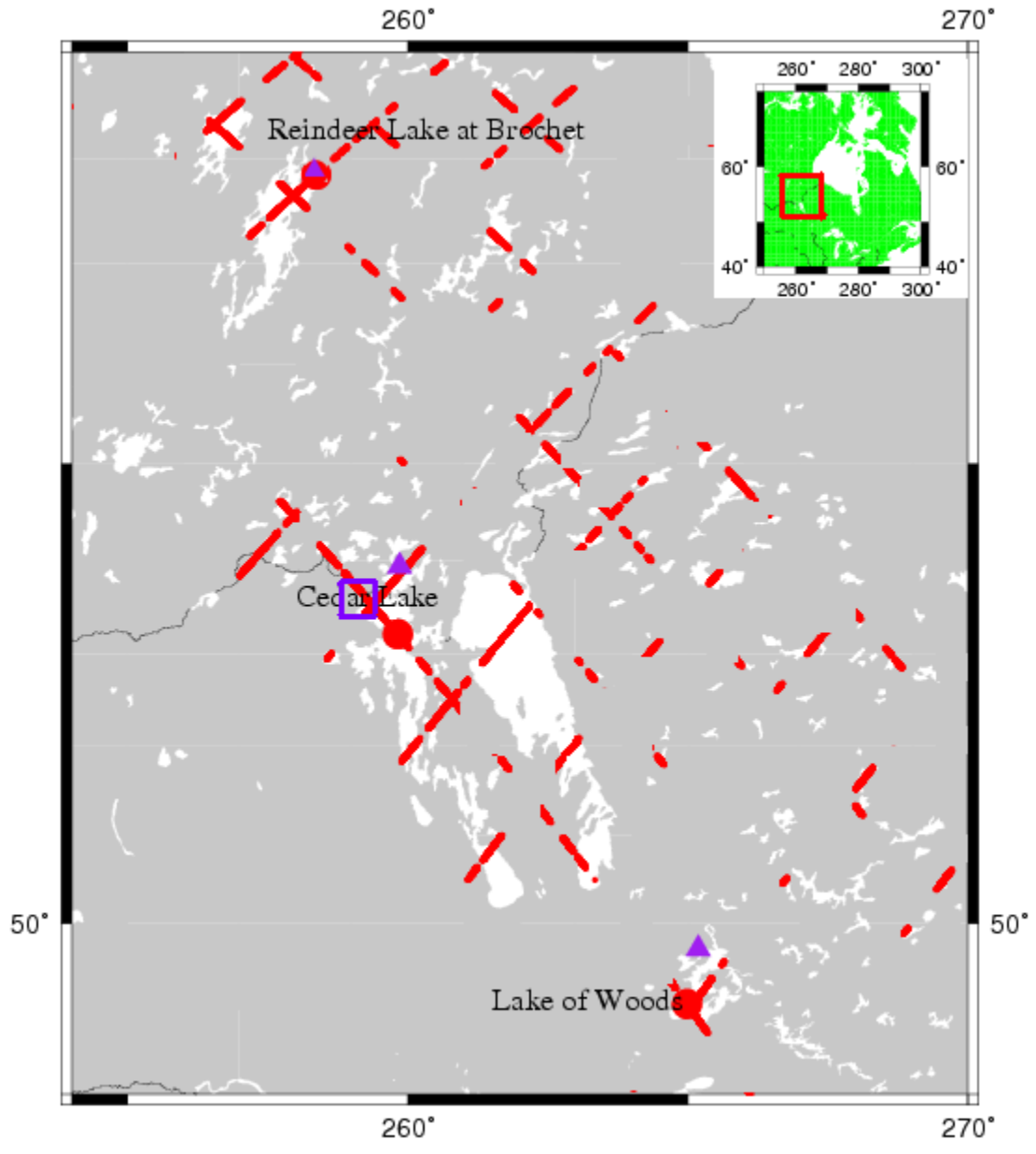


Figure 3.2: Locations of the example points in large lakes used in the comparison and the detected bodies of water in Manitoba and Western Ontario, Canada.

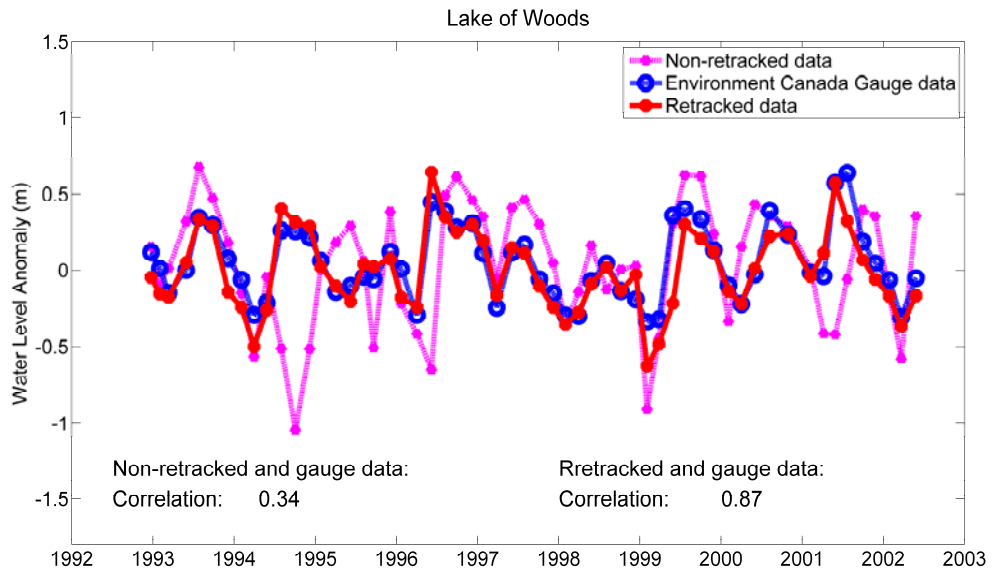


Figure 3.3: Stage gauge time series compared with 1-Hz non-retracked (GDR) and retracked TOPEX data at the Lake of Woods, SW Ontario, Canada.

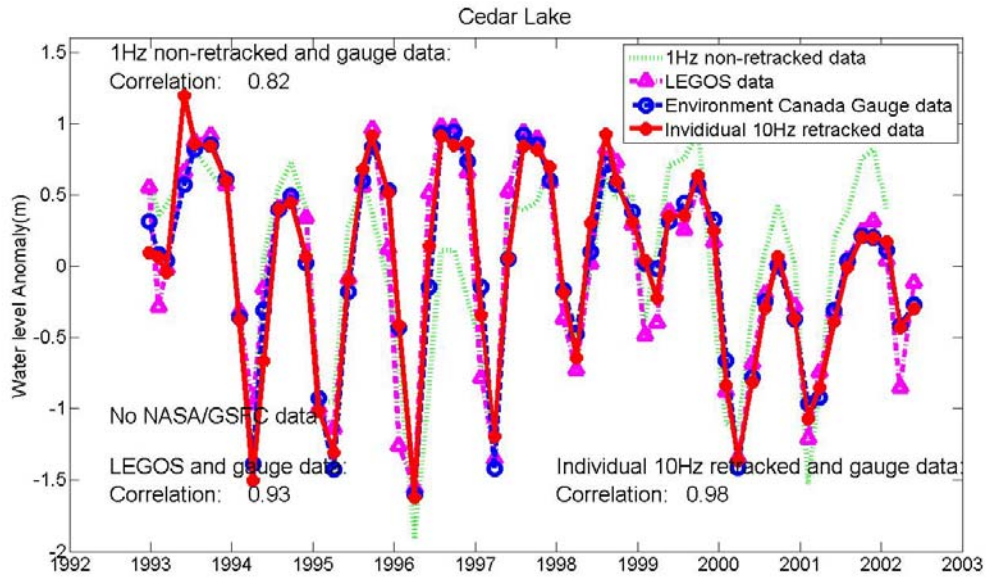


Figure 3.4: Stage gauge time series compared with LEGOS data, 1-Hz non-retracked (GDR) and individual 10-Hz retracked data at Cedar Lake, Manitoba, Canada.

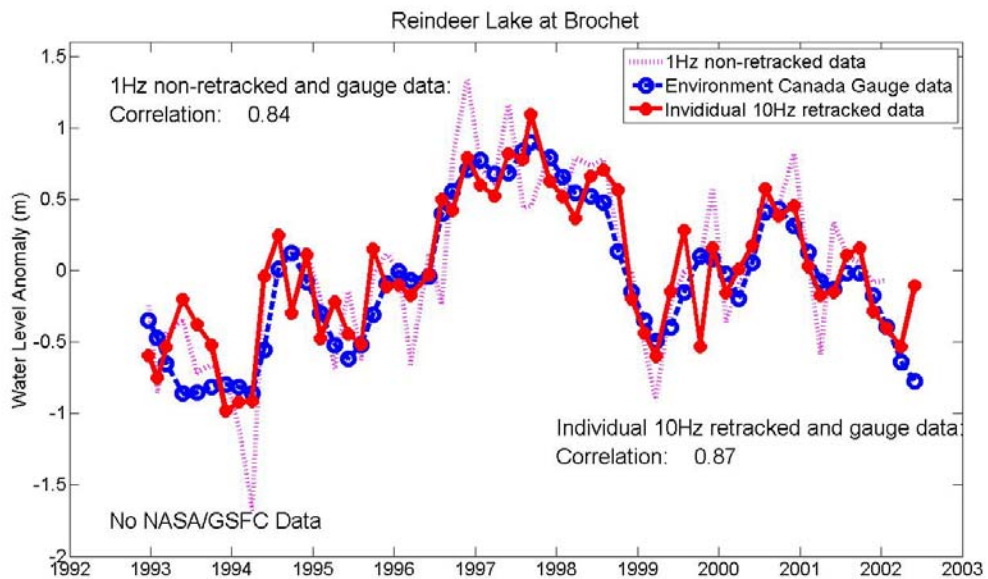
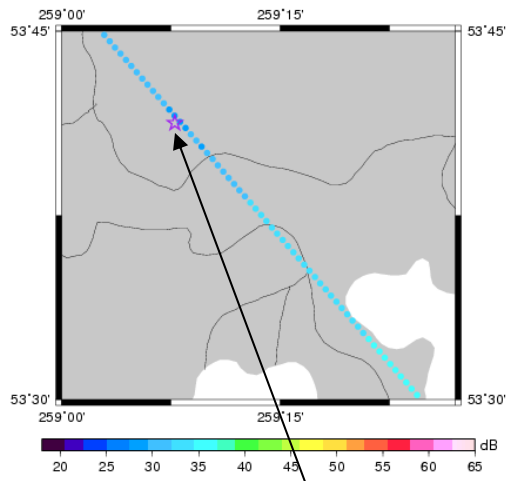


Figure 3.5: Stage gauge time series compared with 1-Hz non-retracked (GDR) and individual 10-Hz retracked data at Reindeer Lake, Brochet, Manitoba, Canada.

TOPEX 10-Hz AGC at 20:38:23~20:38:29 on Jan.12th,1996



TOPEX 10-Hz AGC at 4:8:56~4:9:03 on July 29th,1996

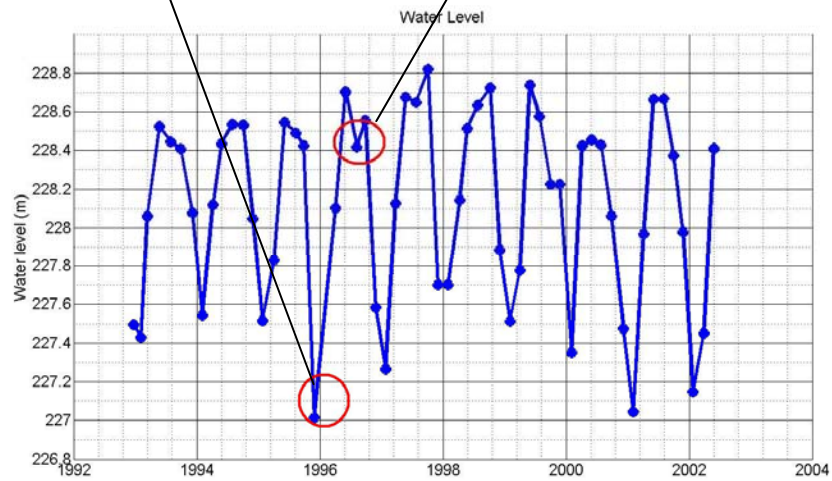
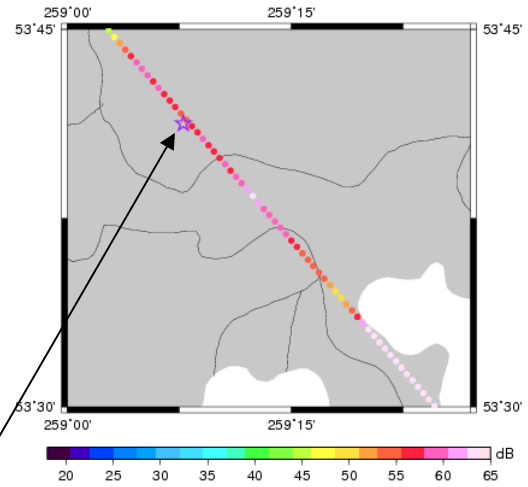


Figure 3.6: The 10-Hz AGC along TOPEX pass #178 when the water level is low (January 12, 1996) and when the water level is high (July 29, 1996) and the retrieved decadal water height for the small body of water away from Cedar Lake, Manitoba, denoted by the purple box in Figure 3.2.

Retracker Gauge	OCO <sub>G</sub>	10% Threshold	20% Threshold	50% Threshold
Lake of Woods	0.76	0.87	0.84	0.80
Reindeer Lake	0.85	0.83	0.87	0.79
Cedar Lake	0.88	0.98	0.97	0.91

Table 3.3: Comparison of the correlation coefficients between the gauge measurements and different retracked water heights for the Lake of Woods, SW Ontario, Canada and Reindeer Lake and Cedar Lake, Manitoba, Canada.

Figure 3.5 shows that we were able to detect the water surface and constructed a TOPEX water level time series in the Reindeer Lake in Manitoba, Canada while there is no data available from the published USDA & NASA/GSFC and CASH data products. We compared our data with the stage data from Environment Canada after the data were interpolated to the same observation time. The comparison shows that the satellite observation has a good correlation of 0.87 with the in situ observations. The individual 10-Hz retracked data has slightly higher correlation with the stage gauge measurement than the 1-Hz non-retracked data. The higher correlation indicates the accuracy is improved using the individual 10-Hz retracked data. Additionally, it is obvious to see from Figure 3.4 that the correlation of individual 10-Hz retracked data reaches 0.98 which is higher than both the LEGOS data and the 1-Hz non-retracked data at Cedar Lake, where there is no USDA & NASA/GSFC and CASH data. Figure 3.3 demonstrates the improvement of the retracked altimeter observations with the correlation value increases from 0.34 to 0.87 at the Lake of Woods where the area has small body of water (Figure 3.2) and there is no CASH data. We compared the retracked height using different retrackers such as the Offset Center Of Gravity (OCO<sub>G</sub>) retracker (Bamber, 1994), 10%, 20%, and 50% threshold retracker (Davis, 1996, Davis, 1997). Table 3.3 shows that the highest correlations of 0.98 and 0.87 are achieved using the 10% threshold retracker for data over Cedar Lake and the Lake of Woods, respectively.

Following the confirmation of the accuracy achieved using the individual 10-Hz retracked satellite altimetry data, we applied the same methodology to detect the smaller body of water and studied the usage of backscatter coefficient for the land surface classification in the inland region away from Cedar Lake, as denoted by the purple box in Figure 3.2. The backscatter coefficient ( $\sigma_0$ ) is the ratio of the returned power and the transmitted power, and it has potential to classify different land surface characteristics as demonstrated by Papa et al. (2003). The backscatter coefficients in TOPEX GDR are only available at 1-Hz frequency, and thus 10-Hz AGC is used instead. It has been known that there is ~20 dB difference between the AGC and  $\sigma_0$  (Birkett, 1998). We detected the body of water where no data is available from LEGOS, USDA& NASA/GSFC and CASH. The results are shown in Figure 3.6. The lower plot is the TOPEX measured decadal water height at the purple star point along in pass #178 shown in the two upper plots in Figure 3.6. The two red circles in the time series denote the measurement times of January 12, 1996 when the

water level is low and July 29, 1996 when the water level is high. We extracted the 10-Hz AGC at these two measurement times along pass #178 as presented in the upper left and upper right plot, respectively. From the upper left plot, we can see the AGC is very low during the winter season, which could indicate the snow coverage. The upper right plot illustrates that AGC is high during the summer when the water level is high causing the large inundated area, so the high AGC value could be used to detect the inland flooded region.

### 3.3 The Amazon River Basin

The Amazon River with more than 1100 tributaries is the world's largest river in terms of water volume. Seven of its tributaries are more than 1600km. About 20% world's river water flowing into oceans is the discharge from the Amazon River into the Atlantic Ocean, which is about 5 times that of the Congo River and 10 times that of the Mississippi River. Due to the massiveness of the water basin and the prohibitive cost to obtain the stage data, scientists used satellite radar altimetry to study the Amazon hydrology (Birkett et al., 2002; Berry et al., 2005; Zakharova et al., 2006).

We demonstrate here the potential of satellite altimetry to study the small river with higher spatial resolution using the retracked individual 10-Hz TOPEX data by applying the algorithm to detect the small bodies of water. The Amazon mask (Hess et al., 2003) we used was made by mosaicking the L-band SAR imageries with the resolution of 100m for dual-season including high-water and low-water conditions. After the delineation of the wetland, the land surface properties are classified into 9 categories (Hess et al., 2003) using information of attributes of pixels. Among nine levels of classifications, the open water, aquatic macrophyte (floating grass), flooded shrub, flooded woodland and flooded forest are considered as water. All other non-flooded and unclassified areas are excluded as non-water surface in the comparison.

We compared the water data points obtained using our algorithm with the points found using the high-water level mask. Figure 3.7 shows the mask region and the results of the comparison of the algorithm-detected points and the mask-detected points in the Amazon River Basin. Blue points denote the water points selected by both the water-detection algorithm and the mask. The red points denote the water points selected only by water-detection algorithm, and they indicate that the algorithm detected the bodies of water missed by the mask. We choose 3 regions including seven example points to validate the points selected only by the algorithm using the detailed hydrological map. The three tested regions for the water detected only by the algorithm are denoted by the three green boxes in Figure 3.7 and the results of the verification of the existence of water are shown in Figure 3.8 through 3.10. The satellite altimeter measurements at these 7 example points in the three tested regions are not available from LEGOS and USDA & NASA/GSFC.

Figure 3.8 shows the validation of the region 1 in Figure 3.7, and part of Figure 3.7 is shown in the upper right panel of Figure 3.8 for convenience. The lower plot is the detailed local map which verifies the existence of water at the points (denoted by the purple points) detected only by the algorithm. The red points in the detailed local map denote the stage gauges closest to the detected points. The stage gauge Fazenda Cipauba does not have data

during the TOPEX/POSEIDON operation time (1992-2002). The upper left plot in Figure 3.8 is the retrieved TOPEX water height measurement at the lower purple point along pass #37. The stage measurement is compared with the individual 10-Hz TOPEX altimeter measurement at Altamira, which is our only available stage data during TOPEX/POSEIDON operation time (1992-2002). The comparison shows that the individual 10-Hz retracked data at the location detected only by the algorithm agrees well with the stage gauge measurement in terms of the seasonal variation except around year 1998. The satellite altimeter measurement was edited out around year 1998 when relatively lower water level can be observed from the stage data, which results in data loss due to the interruptions to the water surface by the surrounding topography. The upper middle plot is another example time series of altimeter measurement at the uppermost purple point along TOPEX pass #37 in Region 1. Similarly, Figure 3.9 and Figure 3.10 verify the existence of water at the points selected in region 2 and region 3.

Similar to what we did in Hudson Bay, we extracted the 10-Hz AGC along TOPEX pass #37 in September, 1996 when the water level is low and in February, 1997 when the water level is high for the region 1 as shown in the lower left and lower right plot, respectively in Figure 3.8 in which the AGC is overlapped in the detailed local map. The different times of 10-Hz AGC are also indicated by the red circles in the upper left plot in Figure 3.8. The detailed local map shows that there are bodies of water in the locations where the AGC value is high. Furthermore, the comparison of AGC at different times demonstrates that the AGC value became higher in February when the water level was high. This implies that the high AGC value indicates the existence of water and thus allowing us to use AGC to detect the flooded region.

On the other hand, it can be seen from Figure 3.8 that the AGC value is relatively low at another body of water detected only by the algorithm denoted by the uppermost purple point along pass #37. This may indicate that the low AGC value cannot be used to verify the non-existence of water because the low AGC value could be obtained over the small body of water surrounded by vegetation (Papa et al., 2003). Overall, when the AGC value is high the existence of the body of water can be inferred. However, when the AGC value is low it could not be used to indicate the non-existence of water.

As we did in Manitoba and SW Ontario, we compared the different retrackers in the Amazon River Basin. The correlation coefficients between the stage and the retracked water height measurements were 0.56, 0.31, and 0.45 using OCOG, 20% and 50% threshold retrackers, respectively. Compared with the results over the Hudson Bay, the correlation coefficients are relatively low and there are obvious amplitude differences between altimeter and gauge data sets. These could be due to the fact that the gauge station is located in the stem of river while the altimeter track point is located in the stream of the river as shown in Figure 3.8. Moreover, the OCOG retracker seems to be the optimal retracker over the Amazon, which agrees with Frappart et al. (2006) whereas the 10% threshold retracker performed better in Manitoba and Ontario. This indicates that waveform retrackers could perform differently and care must be taken to identify the most appropriate waveform retrackers for different regions.

After the verification of the existence of the detected bodies of water, we provided more individual 10-Hz time series for the example bodies of water detected by the algorithm to facilitate the possible hydrology and climatology study in the Amazon River Basin, the plots of time series are shown in Figure 3.11 and the coordinates of the selected points are listed in Table 3.4.

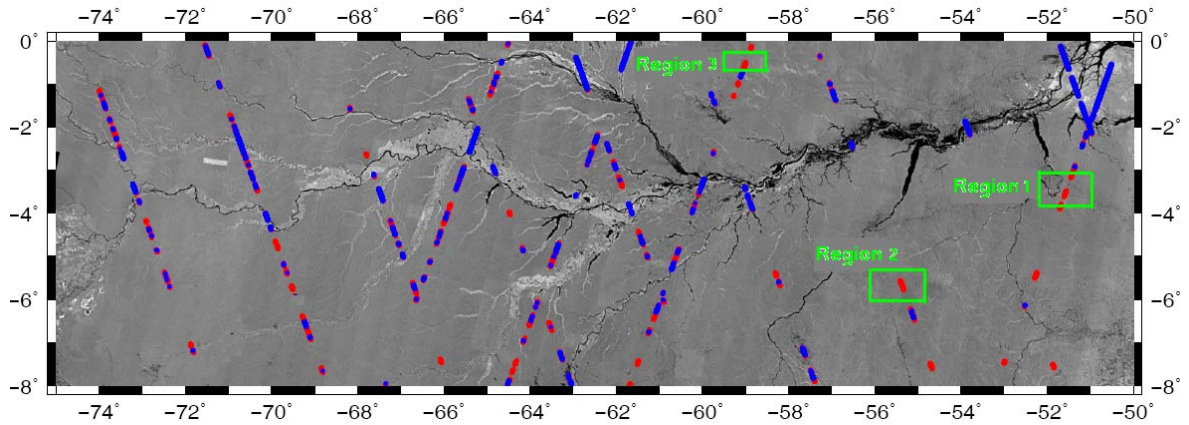


Figure 3.7: Comparison of the algorithm-detected points and the mask-detected points in the Amazon River Basin.

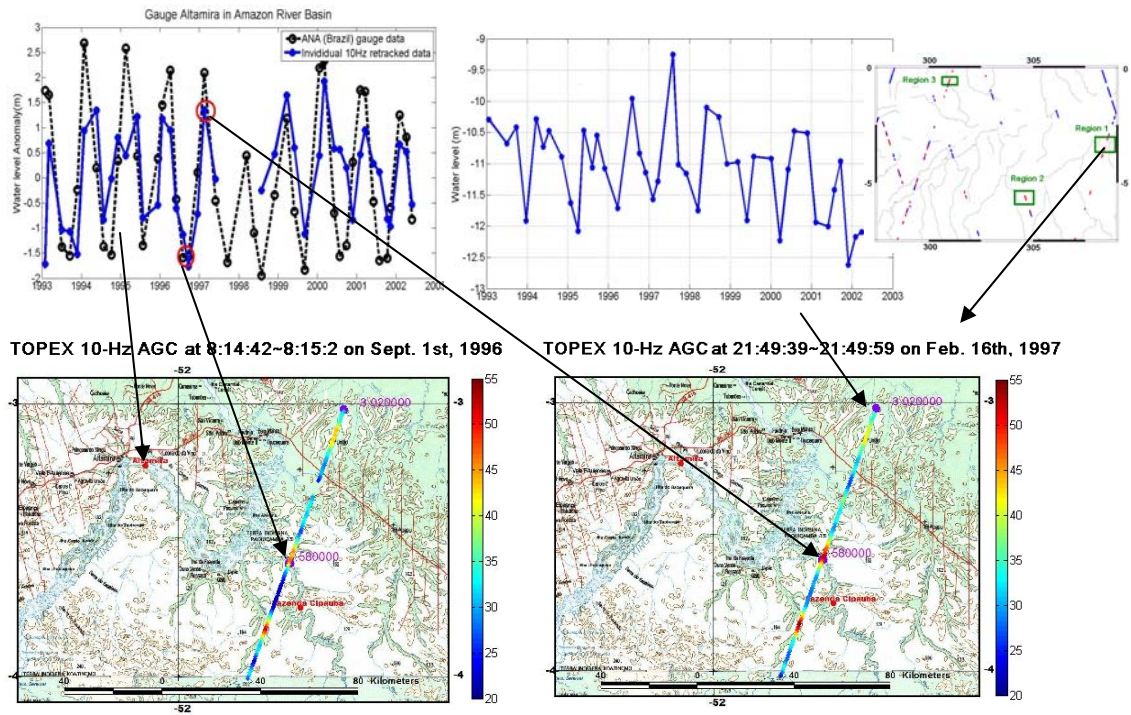


Figure 3.8: Verification of the existence of the water at the points (denoted by the purple points in the detailed map) detected only by the algorithm and 10-Hz AGC in dry season (September 1, 1996) and wet season (February 16, 1997) in region 1 in the Amazon basin.

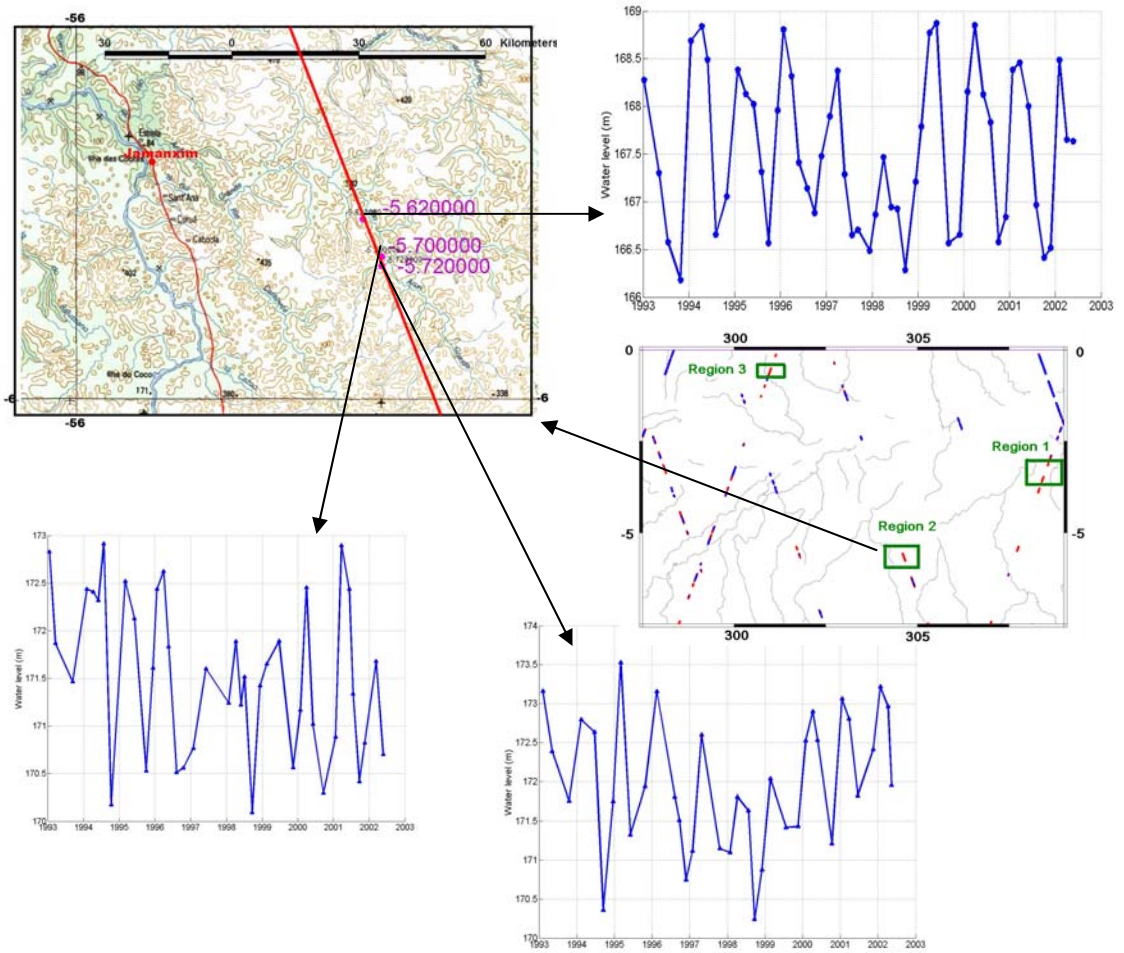


Figure 3.9: Verification of the existence of the water at the points (denoted by the purple points in the detailed map) detected only by the algorithm in region 2 in the Amazon basin.

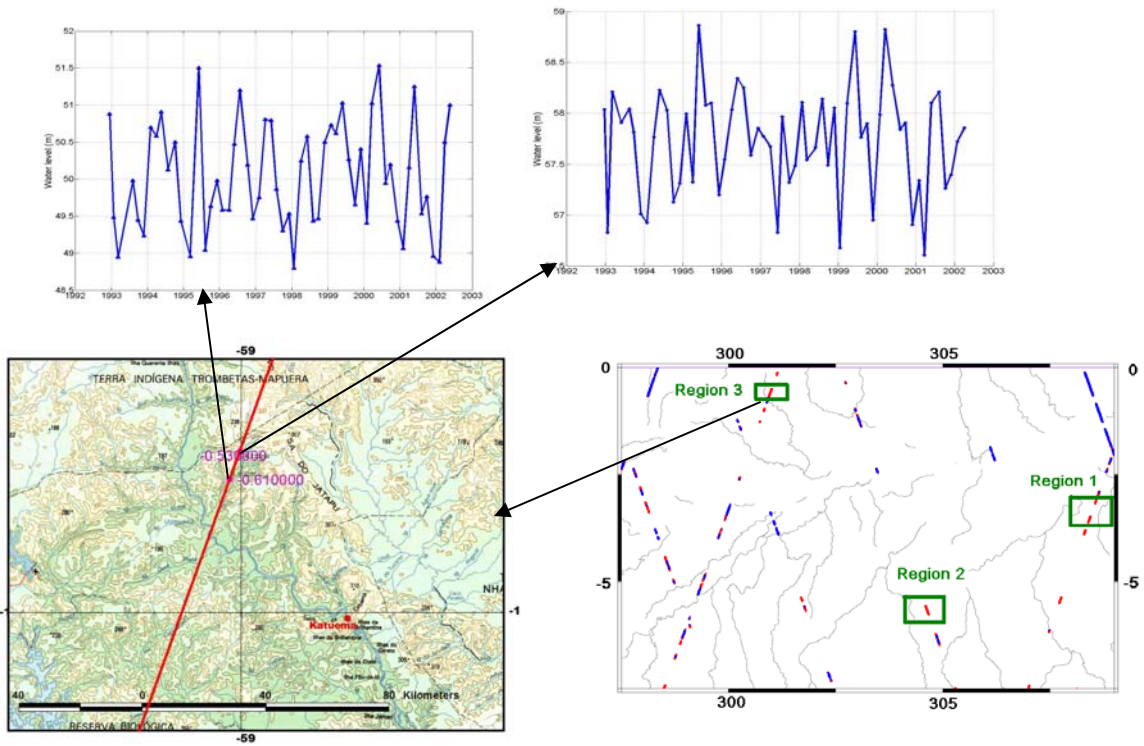


Figure 3.10: Verification of the existence of the water at the points (denoted by the purple points in the detailed map) detected only by the algorithm in region 3 in the Amazon basin.

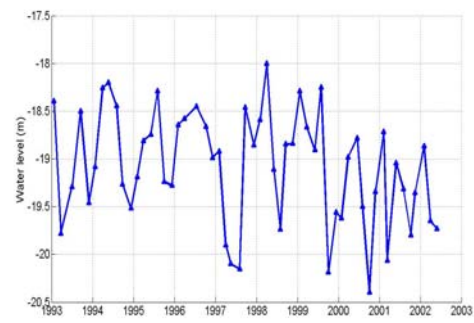
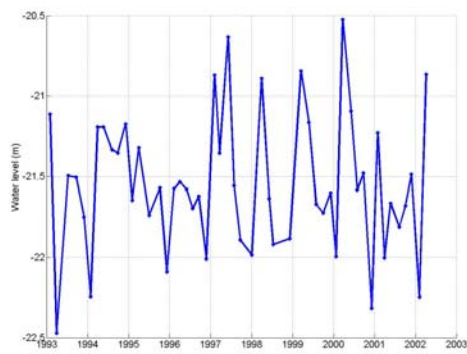
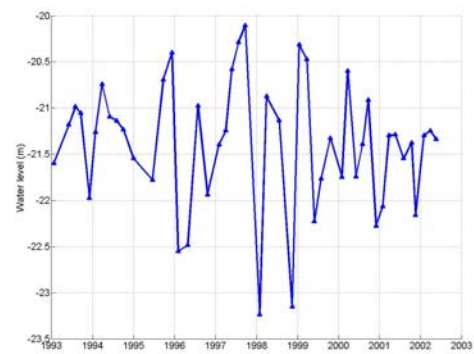
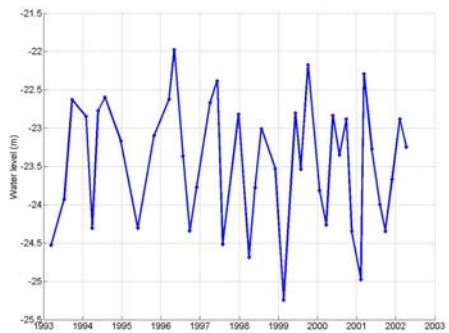
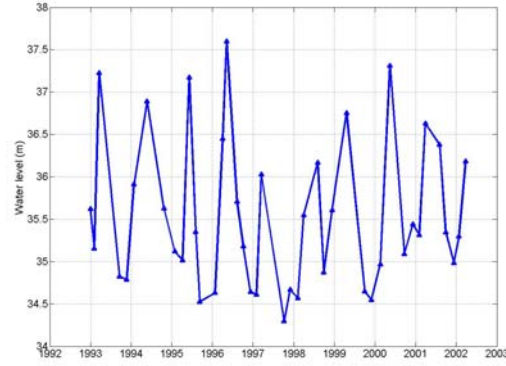
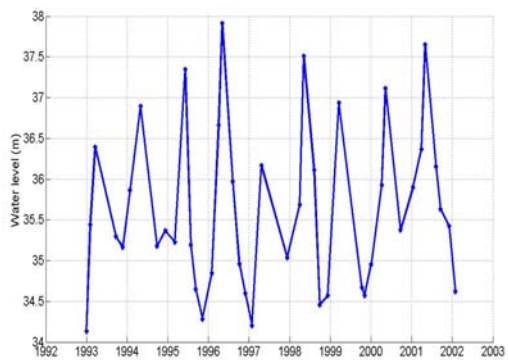


Figure 3.11: Decadal time series of the bodies of water selected by both the mask and the algorithm. The location of the data in Stackfile is: row -57, -58 of column104, row -42, -46, -41, row -56 of column110 from upper left plot to lower right plot, the coordinates of each point are listed in Table 3.4.

	Column #	Row #	Longitude	Latitude
Points indicated as water by both mask and algorithm	110	-41(#6)	308.92	-2.15
		-42(#5)	308.90	-2.21
		-46(#3)	308.82	-2.43
		-56(#9)	308.64	-2.93
	104	-57(#6)	295.17	-3.00
		-58(#1)	295.18	-3.03
Points indicated as water only by algorithm	110	-57(#2)	308.61	-3.02
		-68(#4)	308.41	-3.58
	107(Ascending)	-10(#6)	301.00	-0.53
		-11(#1)	300.97	-0.61
	107(Descending)	-107(#4)	304.61	-5.62
		-108(#10)	304.65	-5.70
		-109(#2)	304.65	-5.72

Table 3.4: The coordinates for the example bodies of water selected by the algorithm and shown in Figure 3.8-Figure 3.11.

### 3.4 Southwestern Taiwan

The climate in Taiwan is divided into two zones, the tropical monsoon climate in the south and semi-tropical monsoon climate in the north as the Tropic of Cancer ( $23.5^{\circ}$  N) across its middle region. From January to late March, there is drizzle in the northern region due to the northeast monsoon while the central and southern region is dry, except several weeks of rain during and after the Lunar New Year. From June to September, the monsoon causes heavy rainfall in the central and southern Taiwan accounting for 80% of annual precipitation (Yen & Chen, 2000). This climatology indicates that the land is inundated approximately twice a year.

Figure 3.12 presents the TOPEX nominal tracks over Taiwan island. We examined the ascending TOPEX track measuring the relatively flat terrains in the southwestern Taiwan. The study region is denoted by the purple box in Figure 3.12. We investigated the variation of monthly 10-Hz AGC along TOPEX pass #51 from 1992 to 2002 as shown in Figure 3.13 and Figure 3.14 from January to December. In Figure 3.13 and Figure 3.14, three purple stars represent the example locations where we extracted time series of 10-Hz water height and 10-Hz AGC. The 10-Hz AGC along TOPEX pass #51 in Figure 3.13 and Figure 3.14 demonstrate that the AGC is higher in the river regions and during the rainy season in southwestern Taiwan. Based on that, we extracted the 10-Hz AGC to detect the water extent indicated by the high AGC value ( $>55\text{dB}$ ) along TOPEX pass #51 on August 3<sup>rd</sup>, 2002 which corresponds to the rainy season as shown in the lower left panel in Figure 3.15.

The right lower plot in Figure 3.15 demonstrates that there is a river as shown in Google Earth at the location of the southernmost star point along TOPEX pass #51 shown as the red line. It should also be noted that there is no satellite derived high level data from LEGOS and USDA & NASA/GSFC in Taiwan region. We extracted the decadal time series of 10-Hz water level and 10-Hz AGC with temporal resolution of 10 days at the star points along the track, and the time series using the smoothed data are shown in Figure 3.15. The red circles in these time series plots indicate the AGC and water height on August 3rd, 2002. The southernmost star point has a more distinct seasonal signal, which indicates the seasonal variation of the water level due to the change of the rainfall as the rainfall becomes the heaviest in summer and the AGC value becomes the highest accordingly. The two upper star points along the track have more distinct semi-annual signal in AGC and in water height at some years, which can be indicative of the local climate with two rainy seasons (Yen & Chen, 2000).

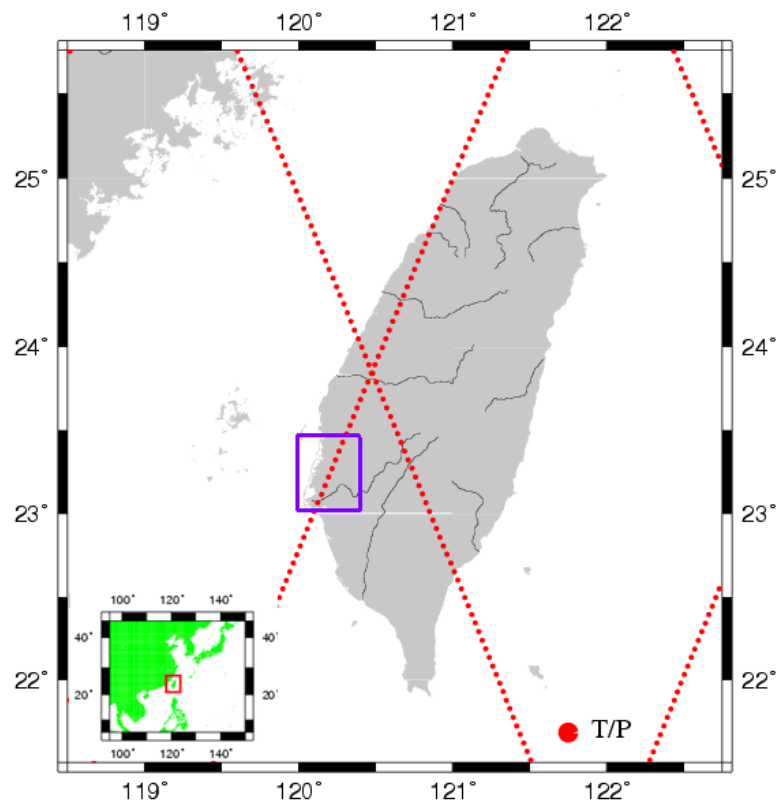


Figure 3.12: TOPEX/POSEIDON (T/P) nominal ground tracks over Taiwan. The purple box is the study region in southwestern Taiwan.

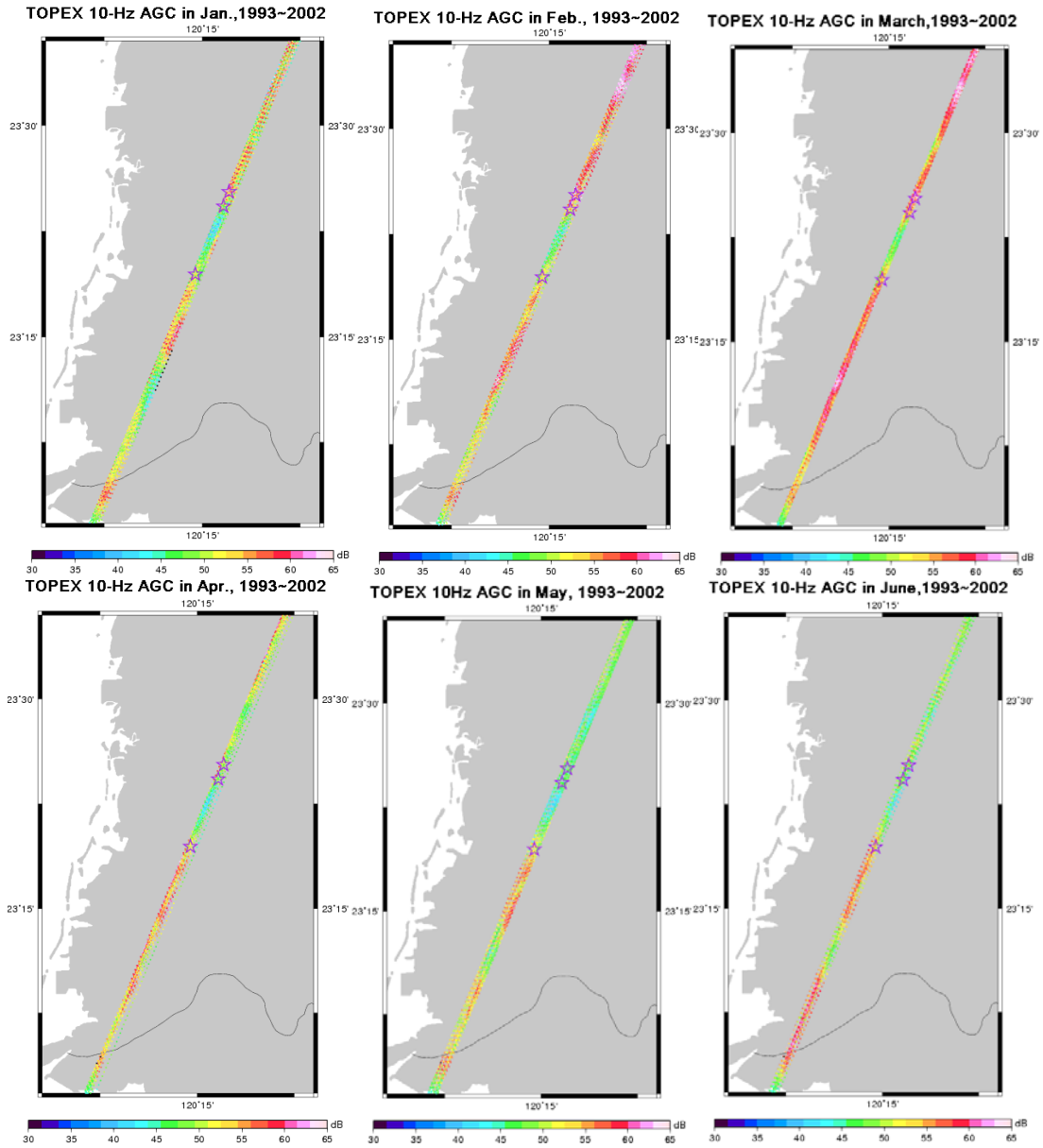


Figure 3.13: TOPEX monthly 10-Hz AGC from January to June, 1993-2002 for the southwestern Taiwan study region shown by the purple box in Figure 3.12.

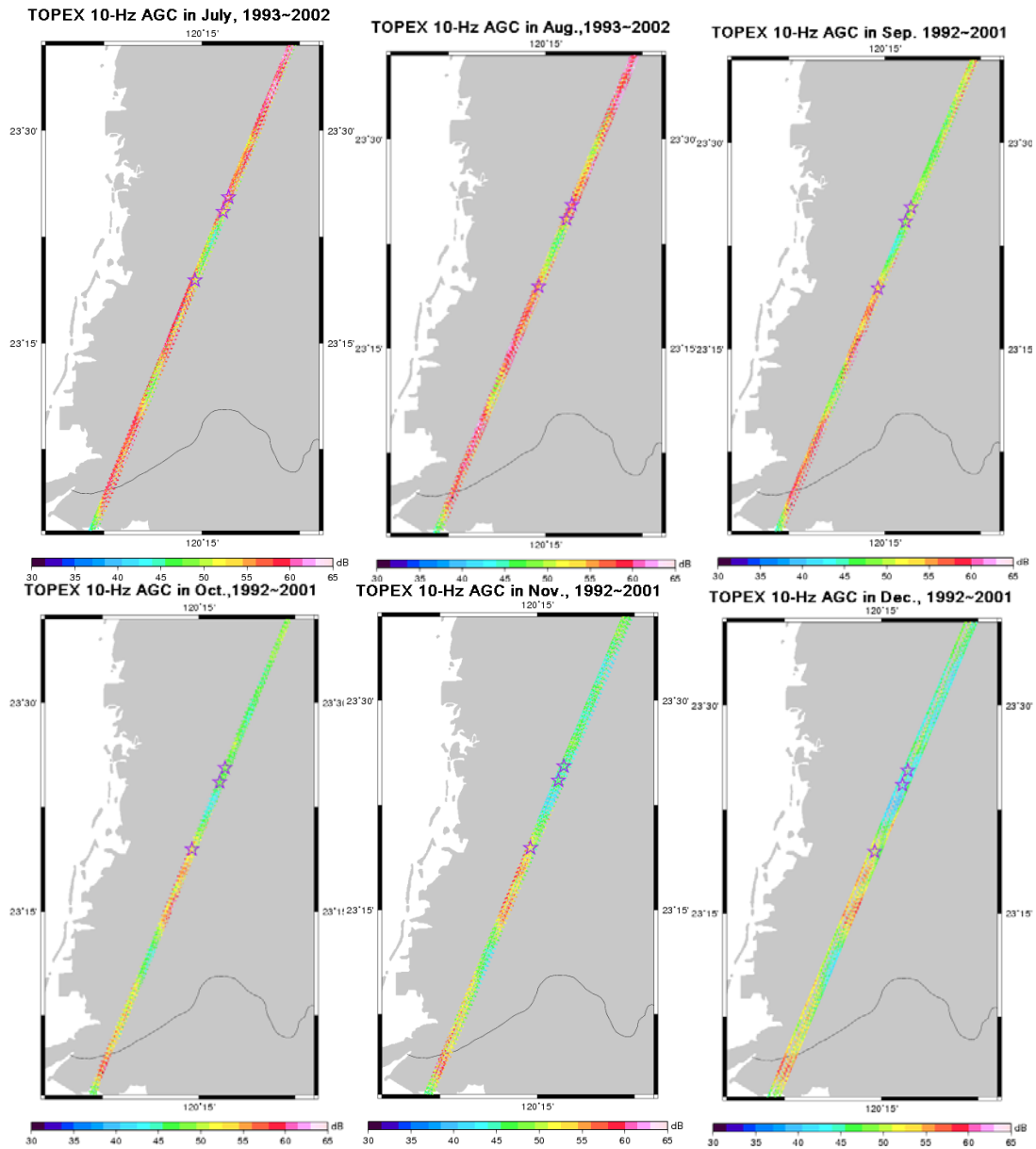


Figure 3.14: TOPEX monthly 10-Hz AGC from July to December, 1992-2002 for the southwestern Taiwan study region shown by the purple box in Figure 3.12.

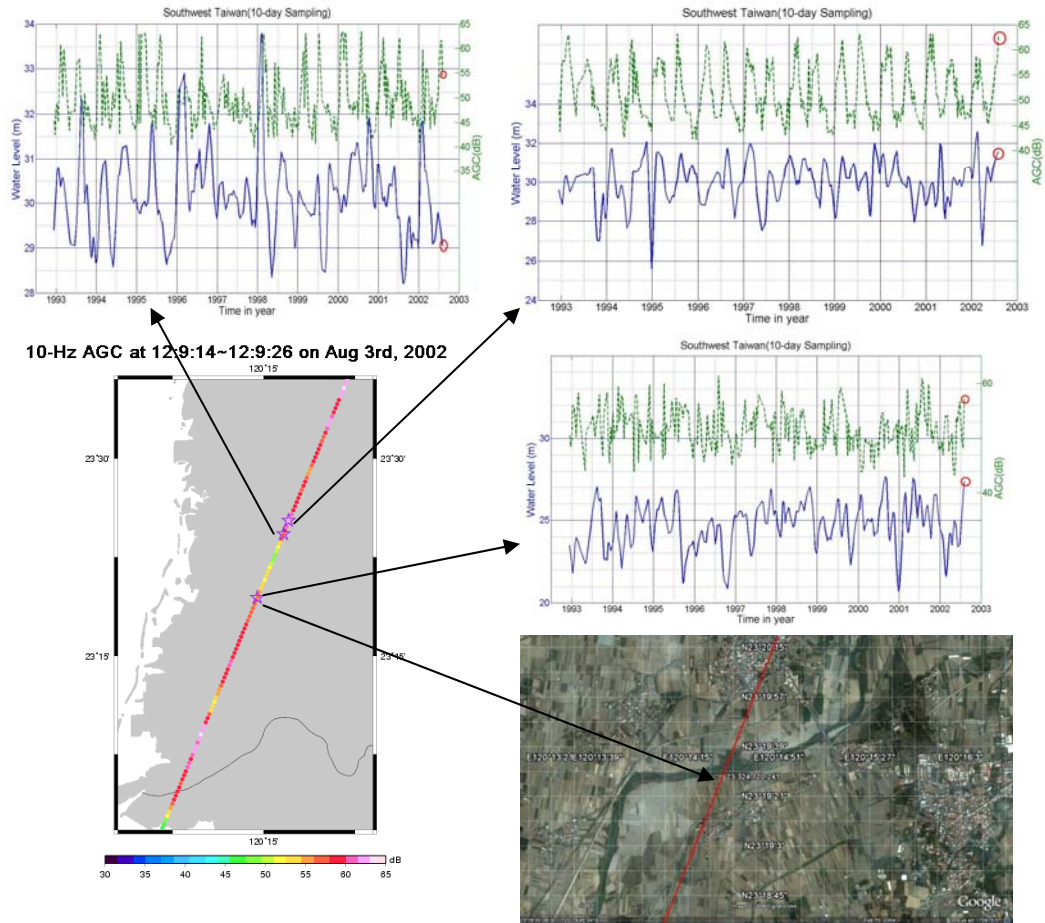


Figure 3.15: The decadal time series of 10-Hz AGC and water height measured by TOPEX in the detected bodies of water verified by the Google Earth or high AGC value in Southwestern Taiwan study region denoted by the purple box in Figure 3.12.

### 3.5 Conclusions

We detected the inland water level variations measured by TOPEX/POSEIDON satellite altimetry using the developed algorithm over the Hudson Bay coastal land region, the Amazon River Basin, and the southwestern Taiwan. The algorithm is based on the backscatter coefficients and the statistical analysis of decadal height measurements. The algorithm is applied in the high-level data product, called Stackfile, to facilitate the efficient access to the altimetry data required for the repeat track analysis. For the first time, the height of small bodies of water measured by TOPEX/POSEIDON are retrieved using the individual retracked 10-Hz data with spatial along track resolution of about 680m while the previous studies (Birkett, 1998; Birkett et al, 2002) used non-retracked TOPEX/POSEIDON data. The individual 10-Hz retracked data provides the measurement with higher accuracy and with the improved spatial resolution.

In the Hudson Bay region, the retrieved 10-Hz height measurements are compared with stage measurements as well as the altimetry products from LEGOS and USDA. The correlation coefficient improved from 0.34 to 0.87 after waveform retracking. Furthermore, the individual 10-Hz retracked measurement provides higher correlation with stage measurement than 1-Hz non-retracked data. The 10-Hz retracked measurement selected by the algorithm improved the quantity and quality of the data. In the Amazon region, we detected small bodies of water which is validated using the detailed hydrological map, but is not shown in the water mask. The measurement from TOPEX shows good agreement in seasonality with the stage data for the small bodies of water. In the southwestern Taiwan study region, the 10-Hz AGC is used to detect the seasonal water coverage. The annual and semi-annual signal shown in the 10-Hz AGC and water level variations indicate the corresponding seasonal variations of local rainfall. The combination of the developed algorithm, optimal waveform retracking of the 10-Hz TOPEX data, and the radar backscatter data provide more detailed hydrologic information which could enhance hydrologic studies of relatively small inland bodies of water.

## CHAPTER 4

### THE 1997 RED RIVER FLOOD

#### 4.1 Introduction

Floods are one of the natural disasters. There have been significant economic losses as a result of major floods. Floods can be categorized into 4 major types according to their causes: riverine flood as a result of the sustained rainfall, rapid snow melting, or intense thunderstorming, estuarine flood which is caused by the storm surge, coastal flood caused by storm, hurricane, or tsunami, and catastrophic flood caused by an unexpected event such as dam breakage, earthquake etc (<http://en.wikipedia.org/wiki/Floods>). To prevent the damages and loss of life, improving flood mitigation, flood modeling and forecasting are among the critical requirements. Timely water level measurements with adequate temporal and spatial resolutions are among the other data types which play a critical role for accurate flood modeling and forecasting. However, the data used are usually stage gauge measurements and in situ flood height data whose availability is limited by the difficulties of collecting and disseminating the data in a timely fashion. In addition, a flood could cause the stage gauges to malfunction. Satellite altimetry has the advantage of global coverage and is an all-weather measurement system, which has the potential to provide large-scale observation of floods. In this chapter, we use TOPEX/POSEIDON retracked data to study the 1997 Red River flood. It is anticipated that the same methodology could be applied in general to other floods. The retrieved water level measurement from satellite altimetry could be used to study the flood extent and flood height, which could be used to improve flood modeling.

The 1997 flood was the most severe flood of the Red River since 1826. USGS stage gauges recorded that the flood covered the Red River Basin in northern North Dakota and western Minnesota, the upper Mississippi River Basin in Minnesota, the Missouri River Basin in southern North Dakota and in South Dakota during the time period from March through June 1997 as shown in Figure 4.1 (Macek-Rowland et al., 2001). There were 3 main factors contributed to the 1997 flood. First was the much-above-normal precipitation before 1997 (US Department of Commerce, NOAA, National Environmental Satellite, Data and Information Service, 1996-97a, 1996-97b, 1996-97c, Macek-Rowland et al., 2001) which resulted in the highly saturated soil. The second factor was the high water level in numerous

small lakes in the northern plain before the flood. The last factor was the heavy snowfall that took place and was 300% above normal during winter and early spring, 1997. Thousands of people had to leave their homes due to the flood. The total estimated damage caused by the 1997 flood was over \$5 billions (<http://nd.water.usgs.gov/photos/1997RedFlood>, NOAA, 1997b). In this Chapter, we study the measurement of flood extent and the water level variation resulting from the 1997 Red River flood using TOPEX/POSEIDON altimetry and USGS stage gauge records.

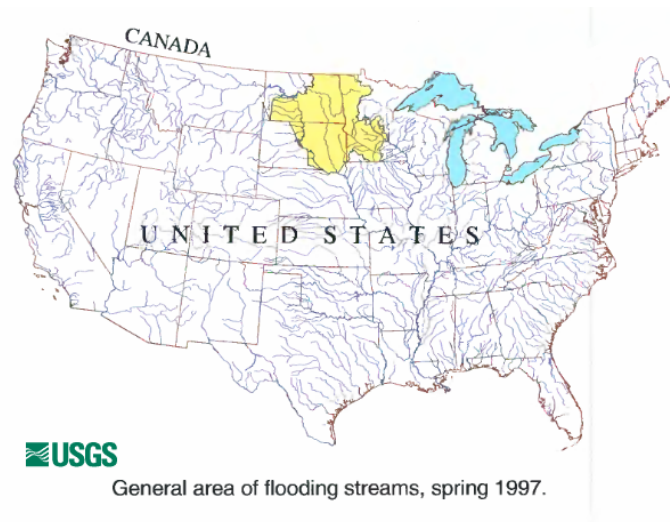


Figure 4.1: The flooding area (yellow shaped region) recorded by USGS.

## 4.2 Flood Extent and Snow Coverage Detection Using Backscatter Coefficients

As described in Chapter 1 and Chapter 3, the backscatter coefficient ( $\sigma_0$ ) has the potential to detect the different properties of land surface. In this study, we explore the application of TOPEX/POSEIDON Ku band (18.6GHz) radar altimeter observed backscatter coefficient in the detection of the snow coverage and flood extent of the 1997 Red River flood. To study the character of the backscatter coefficient during the flood, we extract the Ku band backscatter coefficient from several 10-day repeat cycles corresponding to the time periods before the 1997 flood during early and mid March (cycles 165 and 166), during the flood from late March-July (cycles 167, 168, 169, 170, 171,172, and 173), and after the flood during the summer or August 1997 (cycle 181). Furthermore, we extract  $\sigma_0$  during autumn

or October (cycle 188) and November (cycle 191) and during winter or December (cycle 194), January (cycle 159), and February (cycle 163), 1997 to study the characteristics of the backscatter coefficient of the land cover, focusing on snow cover identifications. The geographic plots of  $\sigma_0$  of the selected cycles along the satellite track in North Dakota, South Dakota and Minnesota are shown in Figure 4.2 through Figure 4.4, the purple line in the plots is the digitalized approximate boundary of the flood recorded by USGS from March-June, 1997 as shown in Figure 4.1. Except the geographic plot, in Figure 4.5 we plot the time series of the 10-Hz water level measurement, and 1-Hz  $\sigma_0$  in 1997 with temporal resolution of 10 days for the location near Fargo, N. Dakota to examine the relationship of the water level and  $\sigma_0$ .

By comparing geographic plots of  $\sigma_0$  at the different time in Figure 4.2 through Figure 4.4, we can see in January and February when there was snow coverage, the  $\sigma_0$  was low (<10dB). In early March  $\sigma_0$  values became higher in the southern South Dakota and southern Minnesota, indicating that snow melting had begun. From April-October 1997,  $\sigma_0$  was obviously higher due to lack of snow. In late November to December when the snow accumulation began, the  $\sigma_0$  values again became small. The same variation of  $\sigma_0$  with the change of the snow coverage could also be exhibited from the time series shown in Figure 4.5. During the snowing season, the  $\sigma_0$  was obviously smaller than that during other times, which indicates that the low  $\sigma_0$  with value <10dB could be used to detect the snow coverage. The same conclusion can be reached in the last plot in Figure 4.2, which shows that  $\sigma_0$  in the middle of North Dakota dropped drastically in early April indicating extensive snow coverage in this region, which agrees with the fact there was a blizzard on April 5-6<sup>th</sup>, 1997 in this region (Macek-Rowland et al., 2001). The conclusion of low  $\sigma_0$  to detect snow coverage agrees with the results in Papa et al. (2003). Table 1 in Papa et al. (2003) shows that  $\sigma_0$  over the Greenland ice sheet has a value of 6.85dB, with a standard deviation of 0.98dB indicating the maximum  $\sigma_0$  over Greenland ice sheet is also <10dB.

Figure 4.2-Figure 4.4 also show  $\sigma_0$  was obviously higher at the recorded flooding locations such as Grand Forks, Fargo in April 1997. In late March when there was snow melting resulting in the local flooding in the west-central and southeastern North Dakota, southwestern Minnesota and north-central South Dakota,  $\sigma_0$  was obviously higher in these regions. The  $\sigma_0$  value became the highest with the value close to the onboard hardware limitation of 44dB during the middle to end of April 1997, especially along Red River of the North, indicating that there was serious flood in the area. After late April,  $\sigma_0$  dropped continuously over most regions, which indicates the retreat of the flood. In the Devils Lake Basin,  $\sigma_0$  value remains high until July as shown in Figure 4.3, which indicates the flooded region remained at the Devil Lake basin. This agrees with the factor that the Devils Lake level kept high until July 1997 (Macek-Rowland et al., 2001). Figure 4.5 shows when the water level is the highest  $\sigma_0$  is also the highest indicating local flooding.

As illustrated above, the backscatter coefficients could be used to detect the flood extent. This is because there is a large area of water inundation during flooding and the reflectivity of water is higher than that of other objects, the returned power of the radar instrument is higher during flooding, and thus the  $\sigma_0$  has a larger value. Based on the above conclusion, we use  $\sigma_0 = 32\text{dB}$  as a threshold to identify the flooded region for the time periods before, during, and after the 1997 Red River flood. The results are shown in Figure 4.6. From Figure 4.6, we can see the inundated regions before and after the flood are obviously smaller than the region during flooding time period. Figure 4.6 also shows that the detected flooded region along TOPEX/POSEIDON ground tracks agrees with USGS recorded flood boundary, which is denoted by the purple line in Figure 4.6. However, in the northwest North Dakota, we detected a larger inundation region resulting from the flood, which is not recorded by USGS. Section 4.3 further proved that flooding indeed occurred in this region, from TOPEX/POSEIDON water level measurements. These results demonstrate that radar satellite altimetry can supplement USGS in situ flood measurements to study this flooding event.

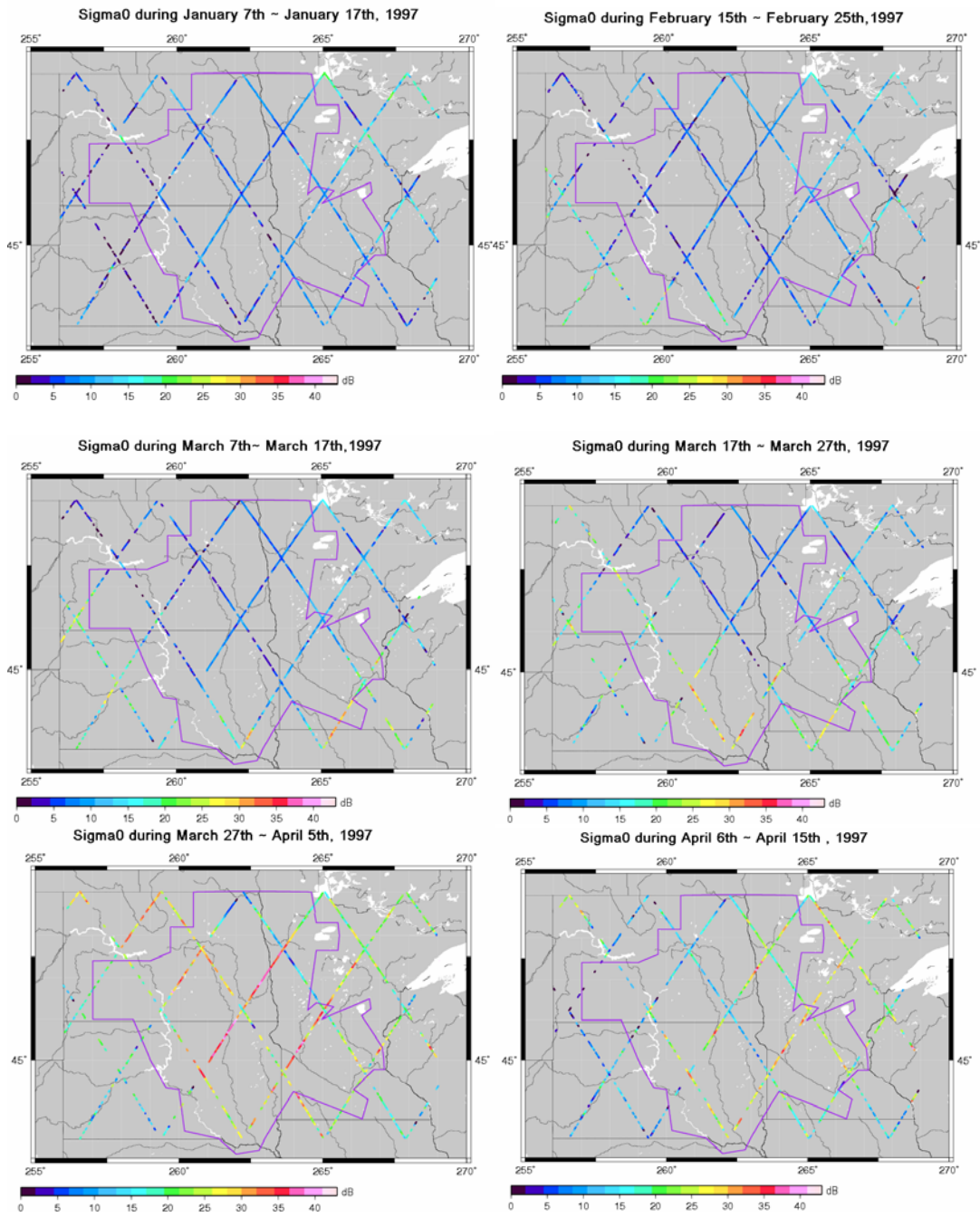


Figure 4.2: Ku Backscatter Coefficient for example cycles from January 7<sup>th</sup> 1997 to April 15<sup>th</sup>, 1997 in North Dakota, South Dakota and Minnesota.

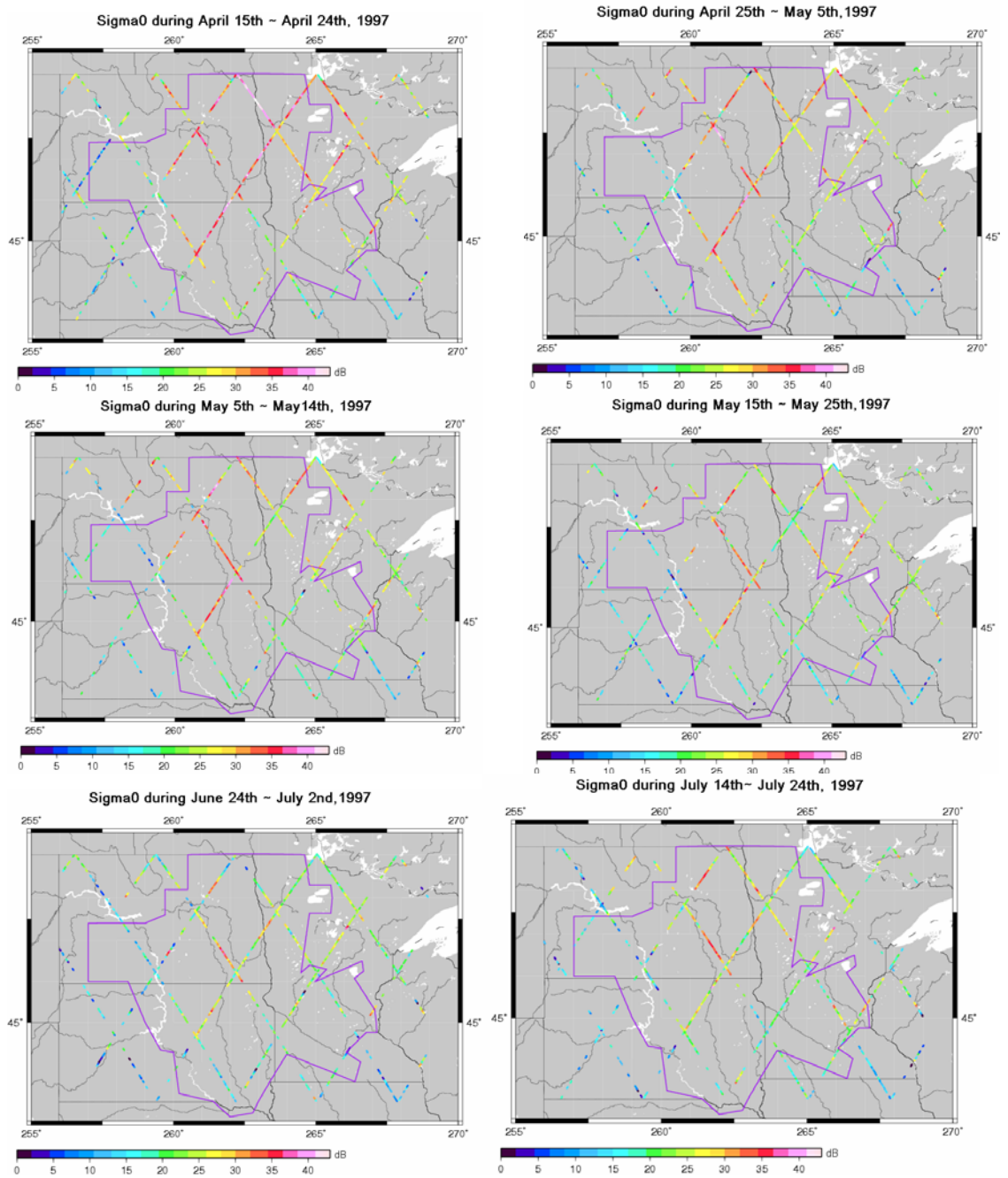


Figure 4.3: Ku Backscatter Coefficient for example cycles from April 15<sup>th</sup>, 1997 to July 24<sup>th</sup>, 1997 in North Dakota, South Dakota and Minnesota.

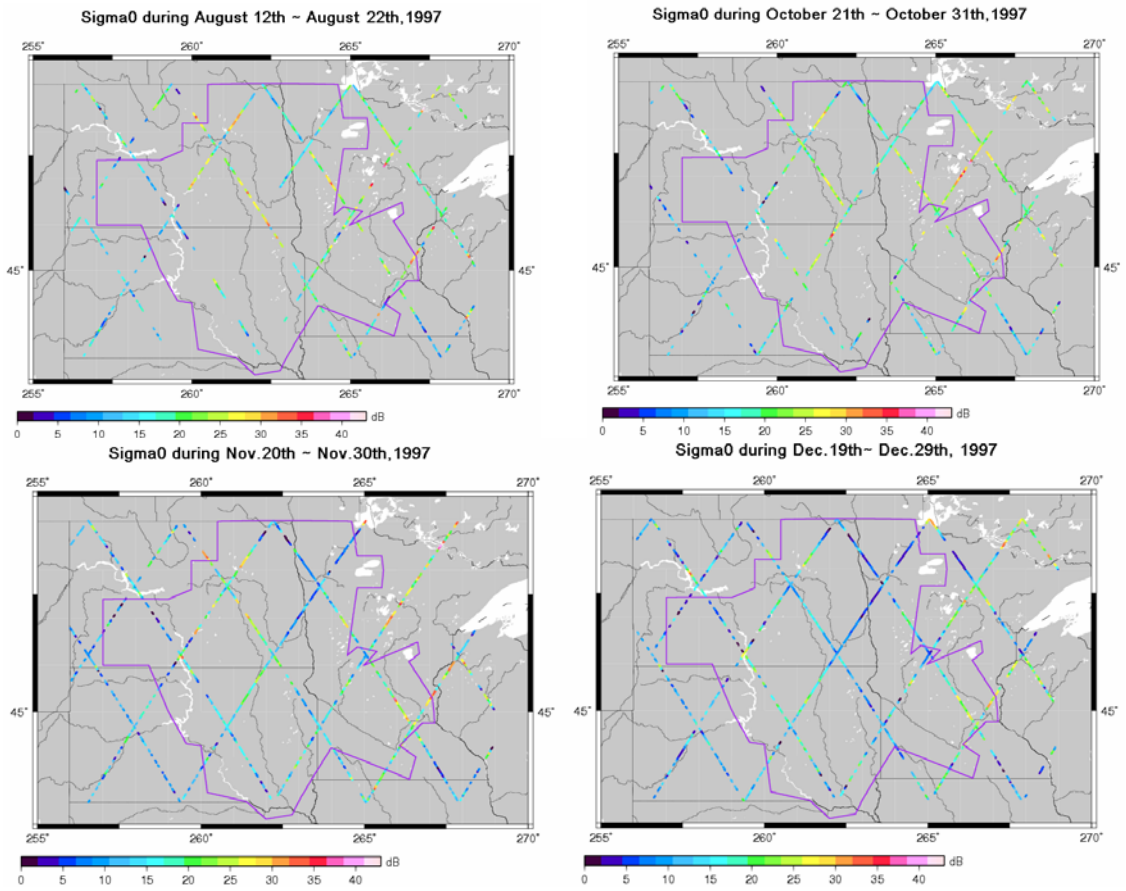


Figure 4.4: Ku Backscatter Coefficient for example cycles from August 12<sup>th</sup>, 1997 to December 29<sup>th</sup>, 1997 in North Dakota, South Dakota and Minnesota.

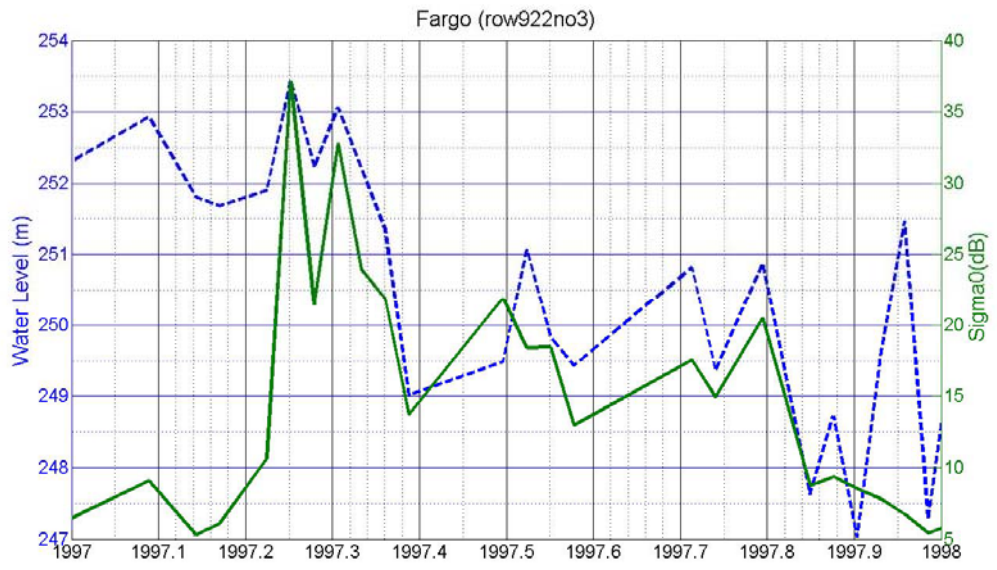


Figure 4.5: The water level measurement and the backscatter coefficient at the location near Fargo, N. Dakota.

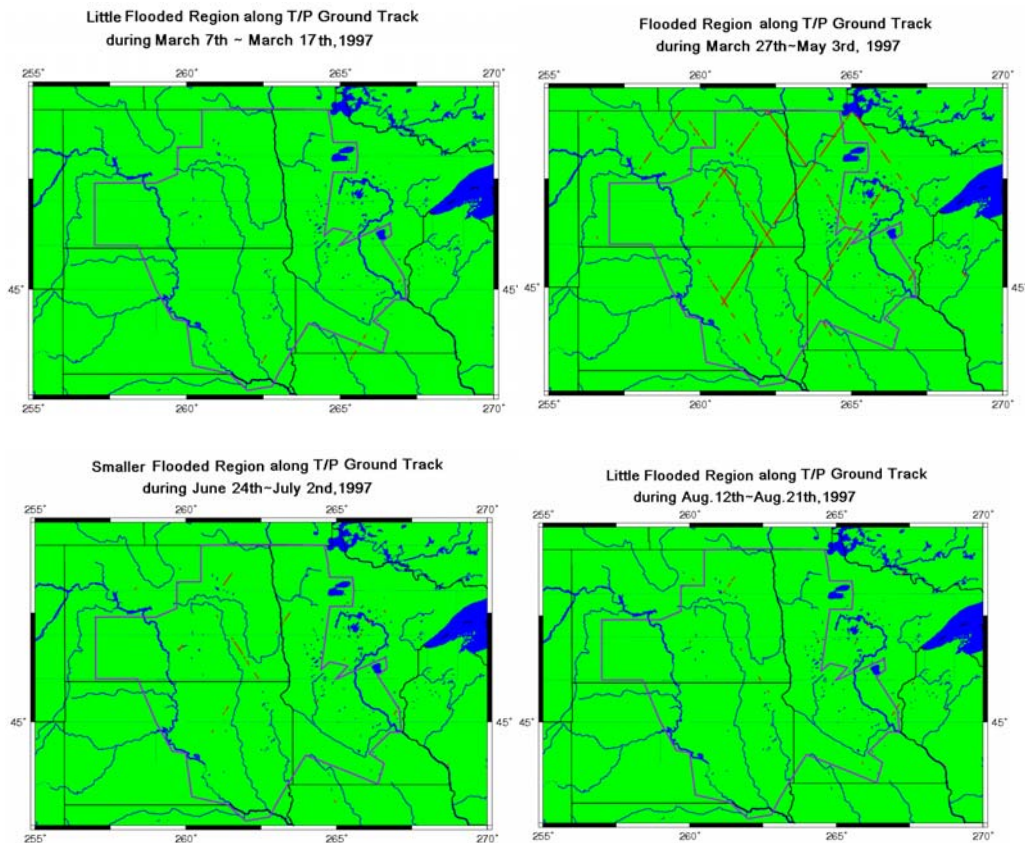


Figure 4.6: The flood extent along the TOPEX/POSEIDON ground tracks before, during and after the 1997 Red River flood.

### 4.3 The 1997 Red River Flood in North Dakota

From the above analysis of  $\sigma_0$ , we know the inundated flood regions include the Red River Basin of the North in North Dakota and in western Minnesota, the upper Mississippi River Basin in Minnesota, the Missouri River Basin in southern North Dakota and in South Dakota. These detected flooded regions agree with the USGS record (Macek-Rowland et al., 2001). In these basins satellite altimetry measurement has not been used to study the flood. Here we use TOPEX/POSEIDON satellite radar altimetry for the first time by applying the water-detection algorithm and using the 10-Hz retracked TOPEX data to study the 1997 flood. The examples of the selected bodies of water indicating the flood in these basins are shown in Figure 4.7, the geographic coordinates of these points are listed in Table 4.1, the location of the data in the Stackfile is denoted by the row# and no# in the title of each time series and in Table 4.1 as explained in Chapter 2. In this Section we present the TOPEX

measurement of the river/lake basins in North Dakota, and the results of measurements for the other basins are presented in the next Section.

The Red River of the North is one of the serious flooded regions in 1997 due to its shallow river channel and flat land surface with less than 0.5ft drop in elevation per mile around Grand Forks (Macek-Rowland et al., 2001). There are numerous small lakes and rivers in the Red River Basin. In addition, there are numerous watersheds in North Dakota which include the James River Basin, the Devis Lake Basin, and the Missouri River Basin. The locations of these basins are shown in Figure 4.8 and the examples of the selected bodies of water in these regions are shown in Figure 4.7. For illustration purposes, we choose Fargo and Grand Forks, N. Dakota as two example regions for the validation of the detected water inundation and to compare 1-Hz non-retracked with 10-Hz retracked radar altimeter measurements for observation of flood elevation change. Finally, we present additional flood water level measurements from satellite altimetry at other locations in North Dakota.

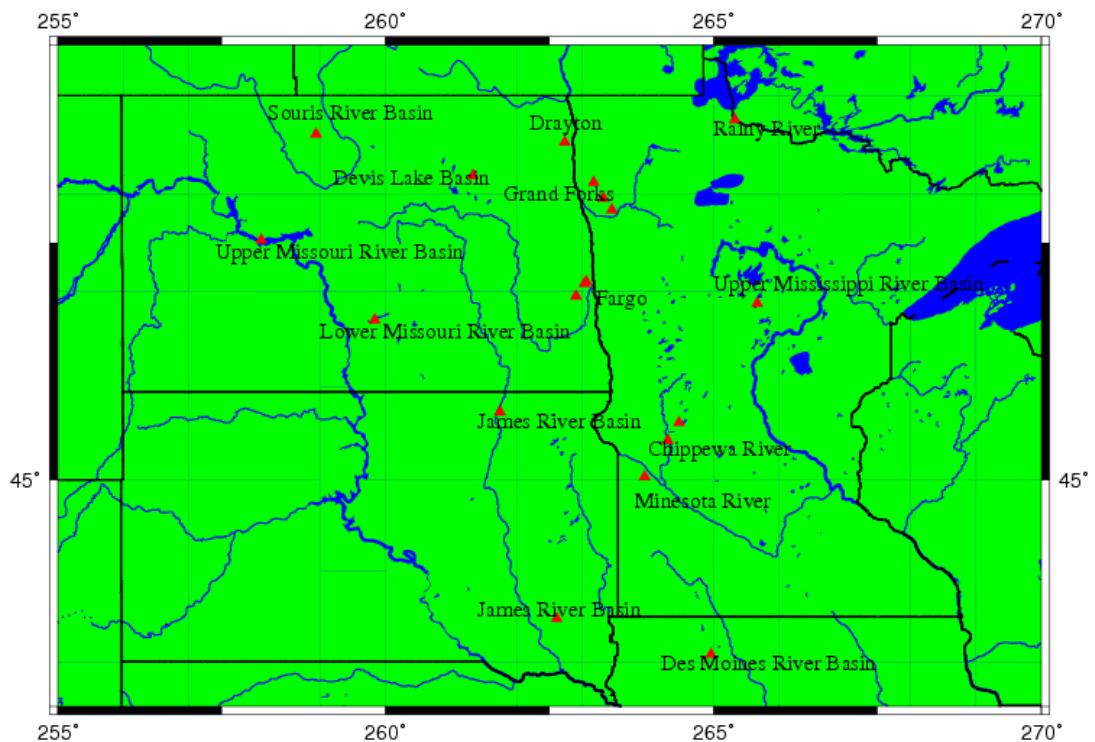
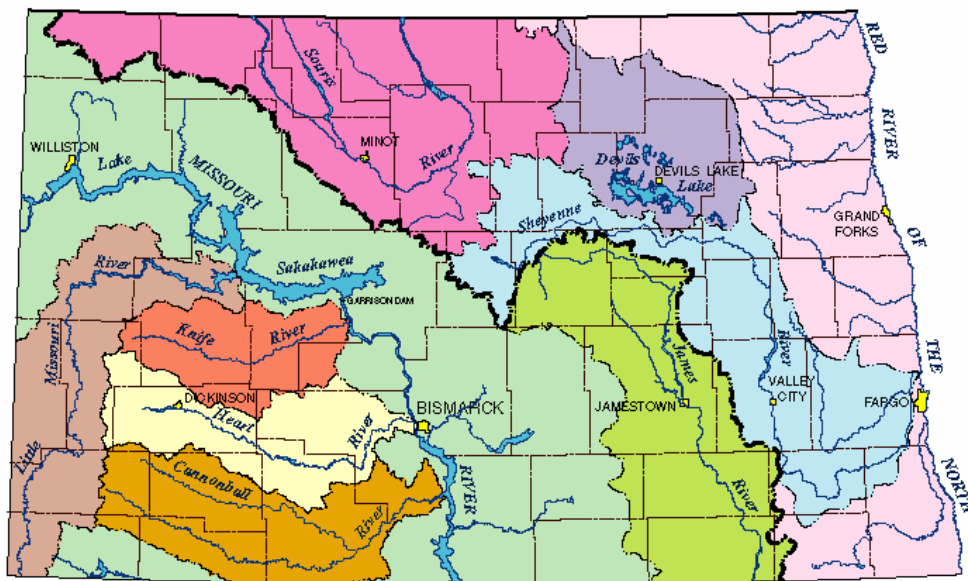


Figure 4.7: The locations of the examples of the selected bodies of water indicating the flood in the Red River of the North Basin, the Missouri River Basin, the Mississippi River Basin, the Minnesota River Basin and their sub-basins.



Major Watersheds of North Dakota - USGS

Figure 4.8: Major watersheds in North Dakota  
<http://savethesheyenne.org/watershedmapusgs.htm>.

To obtain the flood information in Fargo and Grand Forks, which are two typical flooded cities recorded by USGS (Macek-Rowland et al., 2001), we apply the algorithm to select the body of water within the  $1^\circ$  by  $1^\circ$  region centered in the USGS stage gauge of Fargo and Grand Forks respectively. The location of Fargo is shown in the lower right plot in Figure 4.9 through Figure 4.11, the location of Grand Forks is shown in the right plot in Figure 4.12 through Figure 4.14, in these plots the purple triangles denote the selected bodies of water along the satellite track and the red stars denote the stage gauges. There are three locations selected in each of these two regions, the height measurements at all these selected locations are provided in Figure 4.9 through Figure 4.14 with each figure showing the measurement at each of the locations. The upper right plot in Figure 4.9 through Figure 4.11 shows there are small rivers which can not be shown in Figure 4.7 in the Fargo region. We present 2 types of 10-Hz height measurement from TOPEX/POSEIDON with different time span and sampling rate at these locations as explained below.

For the first type of height measurement, the time span is 10 years and the height measurements are averaged every 2 months to reduce data noise. The decadal time series is then compared with the nearby USGS stage gauge measurements available from the USGS web-site (<http://nwis.waterdata.usgs.gov/nwis/measurements>). The decadal measurement from satellite altimeter and the comparison with stage measurement are shown in the upper left plot in Figure 4.9 through Figure 4.14 for each of the locations. The location of the detected bodies of water and the stage gauges are shown in the lower middle plot in each of

Figure 4.9 through Figure 4.14, the red points denote the selected bodies of water along the satellite track and the purple triangles denote the stage gauges in this region. The comparison shows that, although the location of the satellite footprint is different from that of stage gauge, there is seasonal agreement between the stage and the altimeter measurements, which verifies the detected bodies of water and its height measurement from TOPEX. For Grand Forks (upper left plot in each of Figure 4.12 through Figure 4.14), the amplitude of the altimeter measurement is similar or higher than that of USGS stage measurement, while for Fargo (upper left plot in each of Figure 4.9 through Figure 4.11), the amplitude of the altimeter measurement is similar or less than the USGS stage measurement. The amplitude difference between two kinds of measurements is because USGS gauges and satellite altimeter measured height at different locations and in the different time. This first kind of time series includes the height information in years other than 1997 and thus can demonstrate the water level is higher in 1997 flooding time than in other years, which indicates the effect of the 1997 flood. However, it has the disadvantage of obscuring the detailed height information during the flood time due to smoothing.

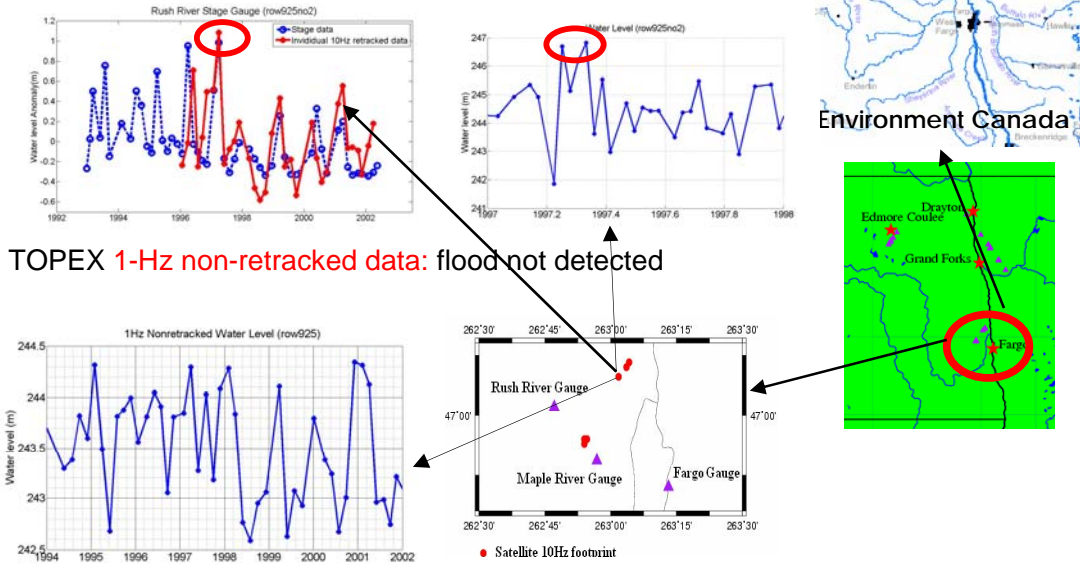
To provide more detailed height and time information of the highest water level during the 1997 flood, we also provide the second type of height measurement with time span reduced to 1 year only, i.e., in 1997, and temporal resolution at 10 days which is the finest temporal sampling rate of TOPEX at any location on Earth. They are shown in the upper middle plot in Figure 4.9 through Figure 4.14 for each of the locations. By keeping the original data with sampling rate of 10 days, the more detailed flood information is retrieved. From this kind of time series for Fargo region (upper middle plot in each of Figure 4.9 through Figure 4.11) we can see the water level is the highest around 1997.25-1997.3, which is in the beginning to middle of April, 1997 when there is serious flood at these locations. Similarly, for Grand Forks region (upper middle plot in each of Figure 4.12 through Figure 4.14) the water level is the highest in the Spring of 1997. The time of the highest water level in the Grand Forks region is different from that in the Fargo region, this is because these two locations are underneath the different satellite track with the different data sampling time, which results in the difference of the observed peak time. The highest observed water level reaches 10 m above the average level in the Grand Forks region. Because TOPEX/POSEIDON can only fly over the same location every 10 days and only the information underneath the satellite track could be retrieved, if the altimeter did not fly over the water with the highest level or at the peak time it will miss the highest water level in that region.

In addition, to assess the value of the 10-Hz retracked measurement in the flood monitoring we compare it with the 1-Hz non-retracked data at the same locations. The 1-Hz non-retracked measurements are shown in the lower left plot in Figure 4.9 through Figure 4.14 with each figure for one location only. From these plots, we can see the 1-Hz non-retracked time series looks mostly noisy without showing the flood, which indicates the 1-Hz non-retracked measurement is not suitable for flood observations in this study and that the 10-Hz retracked measurement is critical to observe the flood information in the relatively small flood inundation region.

**Fargo: TOPEX 10-Hz retracked (OCOG retracker) data: detected flood**

2-month sampling: water level is the highest in 1997 during 1993~2002

10-day sampling: water level is the highest in Spring during 1997



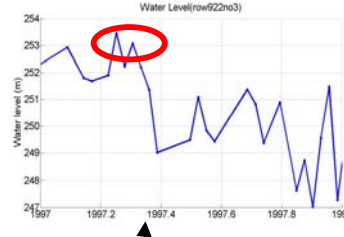
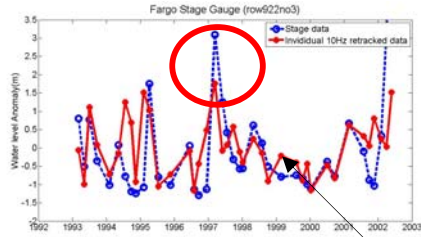
**TOPEX 1-Hz non-retracked data: flood not detected**

Figure 4.9: The time series of the individual 10-Hz retracked TOPEX data with sampling rates of 2-month and 10-day and the time series of the 1-Hz non-retracked TOPEX data for the study of the 1997 Red River flood at the first location in the Fargo region.

**Fargo: Topex 10-Hz retracked (OCOG retracker) data: detected flood**

2-month sampling: water level is the highest in 1993~2002

10-day sampling: water level is the highest in Spring during 1997



**Topex 1-Hz non-retracked data: flood not detected**

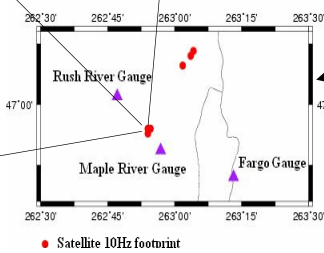
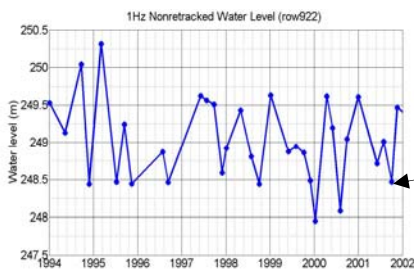
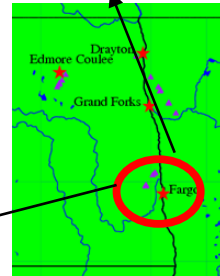
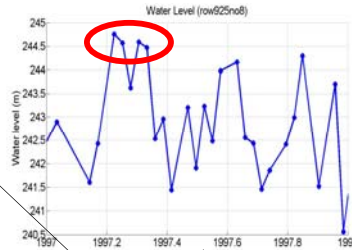
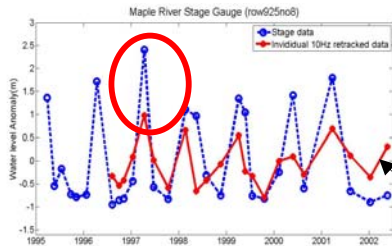


Figure 4.10: The time series of the individual 10-Hz retracked TOPEX data with sampling rates of 2-month and 10-day and the time series of the 1-Hz non-retracked TOPEX data for the study of the 1997 Red River flood at the second location in the Fargo region.

**Fargo:** Topex 10-Hz retracked (OCOG retracker) data: detected flood

2-month sampling: water level is the highest in 1997 during 1993~2002

10-day sampling: water level is the highest in Spring during 1997



Topex 1-Hz non-retracked data: flood not detected

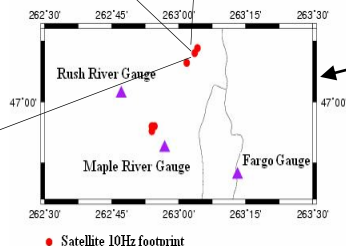
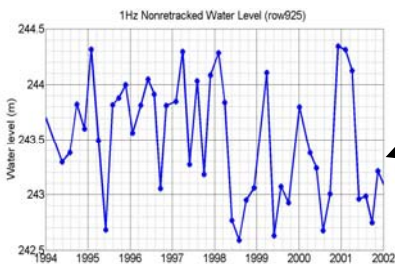
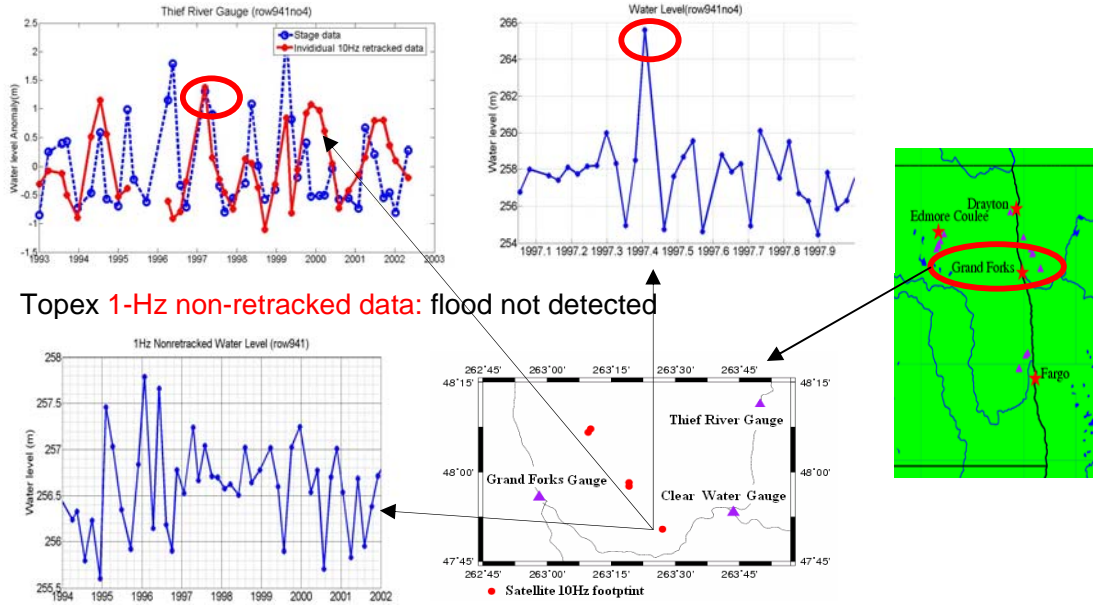


Figure 4.11: The time series of the individual 10-Hz retracked TOPEX data with sampling rates of 2-month and 10-day and the time series of the 1-Hz non-retracked TOPEX data for the study of the 1997 Red River flood at the third location in the Fargo region.

**Grand Forks: TOPEX 10-Hz retracked (OCOG retracker) data:** Detected flood  
 2-month sampling: water level is the highest in 1997 during 1993~2002  
 10-day sampling: water level is the highest in Spring during 1997



**Topex 1-Hz non-retracked data:** flood not detected

Figure 4.12: The time series of the individual 10-Hz retracked TOPEX data with sampling rates of 2-month and 10-day and the time series of the 1-Hz non-retracked TOPEX data for the study of the 1997 Red River flood at the first location in the Grand Forks region.

**Grand Forks: TOPEX 10-Hz retracked (OCOG retracker) data:** Detected flood  
 2-month sampling: water level is the highest in 1997 during 1993~2002  
 10-day sampling: water level is the highest in Spring during 1997

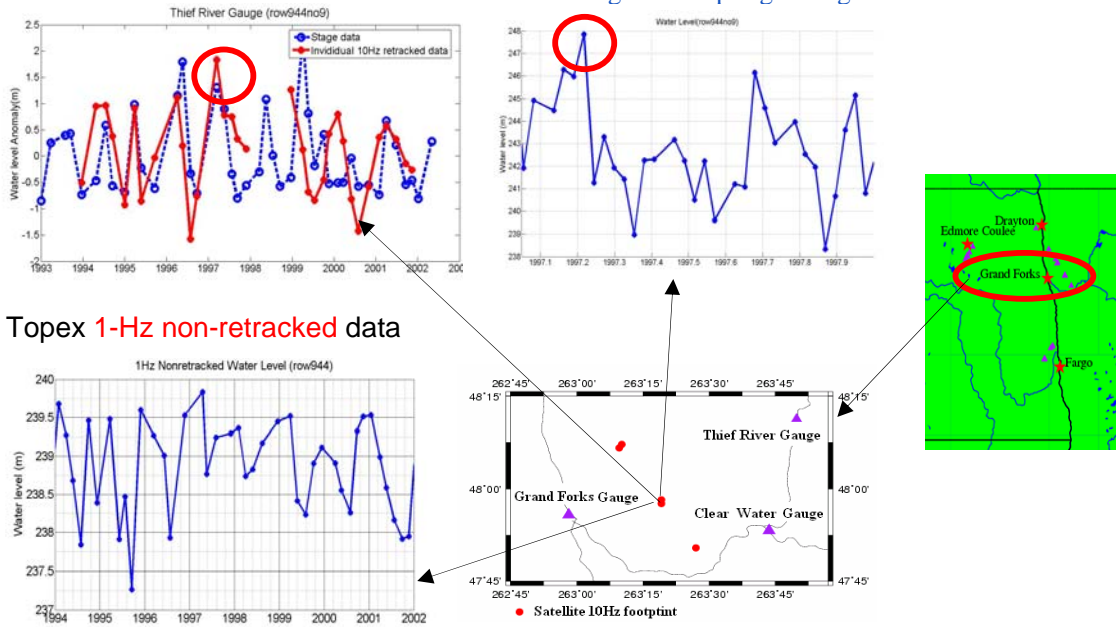
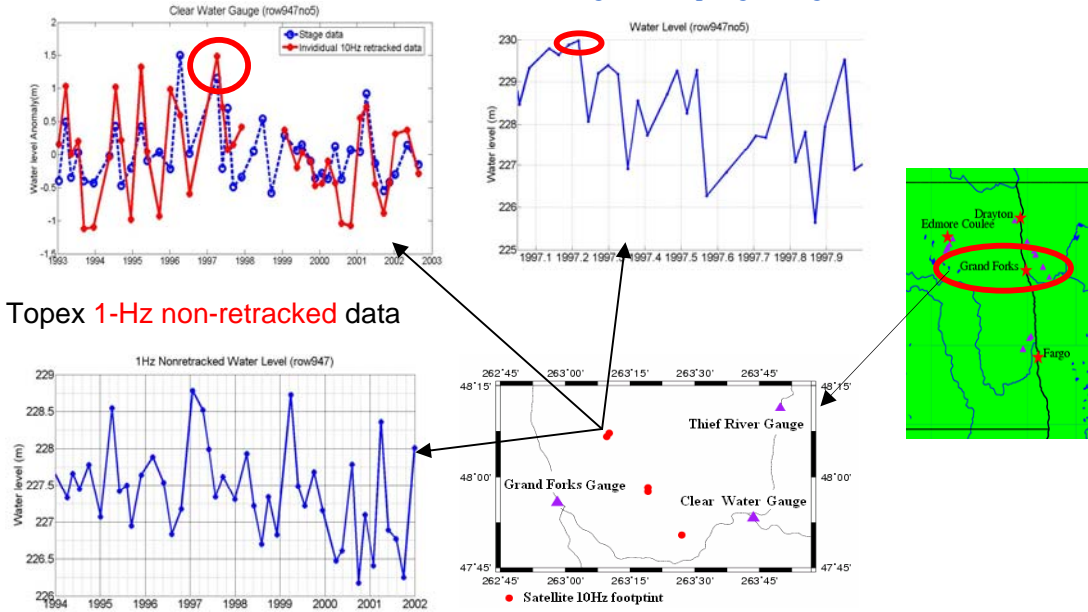


Figure 4.13: The time series of the individual 10-Hz retracked TOPEX data with sampling rates of 2-month and 10-day and the time series of the 1-Hz non-retrackded TOPEX data for the study of the 1997 Red River flood at the second location in the Grand Forks region.

**Grand Forks: TOPEX 10-Hz retracked (OCOG retracker) data:** Detected flood  
 2-month sampling: water level is the highest in 1997 during 1993~2002  
 10-day sampling: water level is the highest in Spring during 1997



Topex 1-Hz non-retracked data

Figure 4.14: The time series of the individual 10-Hz retracked TOPEX data with sampling rates of 2-month and 10-day and the time series of the 1-Hz non-retracked TOPEX data for the study of the 1997 Red River flood at the third location in the Grand Forks region.

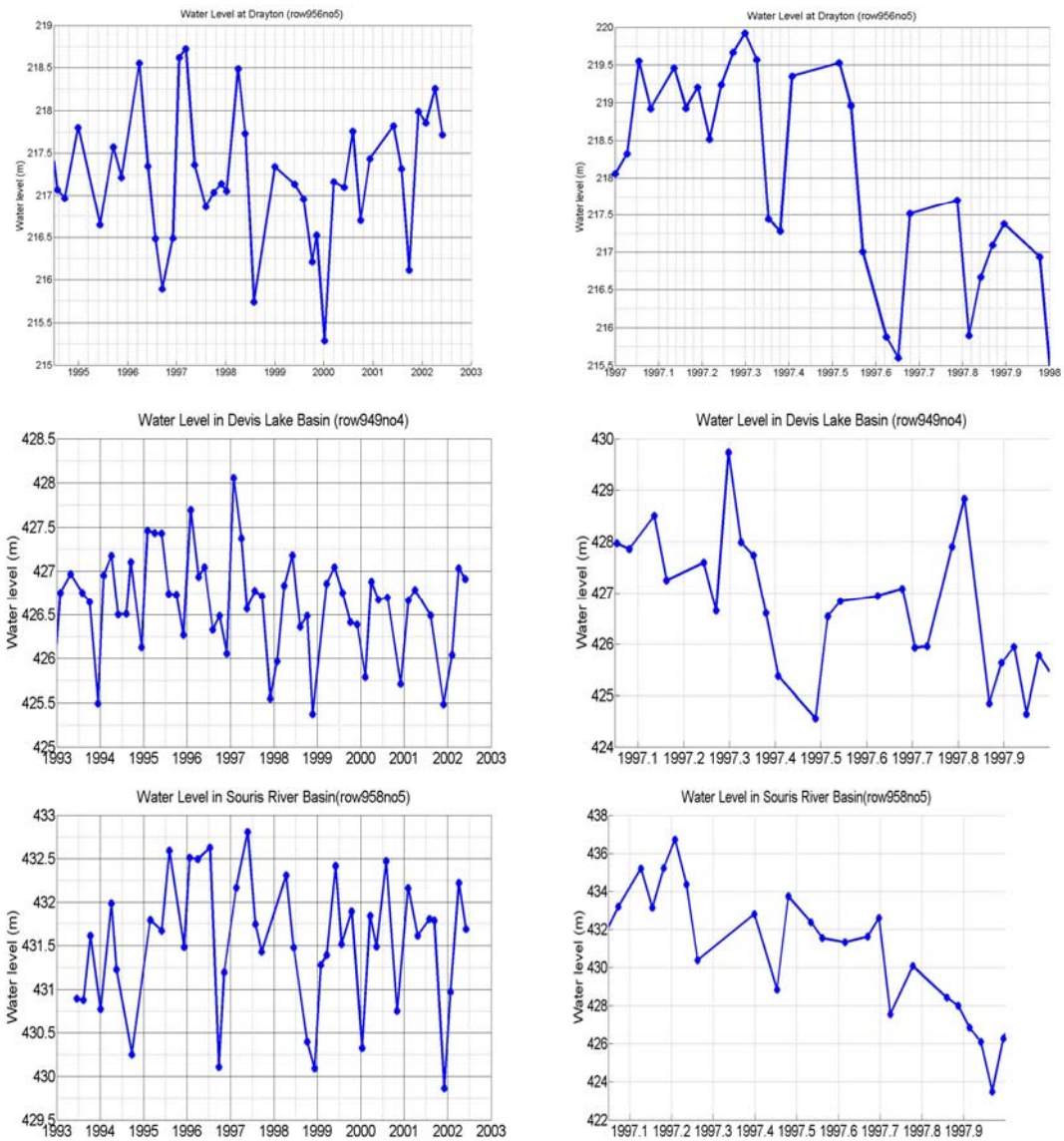


Figure 4.15: The height measurement of the body of water in the Drayton region, in the Bevis Lake Basin and in the Souris River Basin. The right side is 2-month sampling data from 1993-2003 and the left side is 10-day sampling data in 1997.

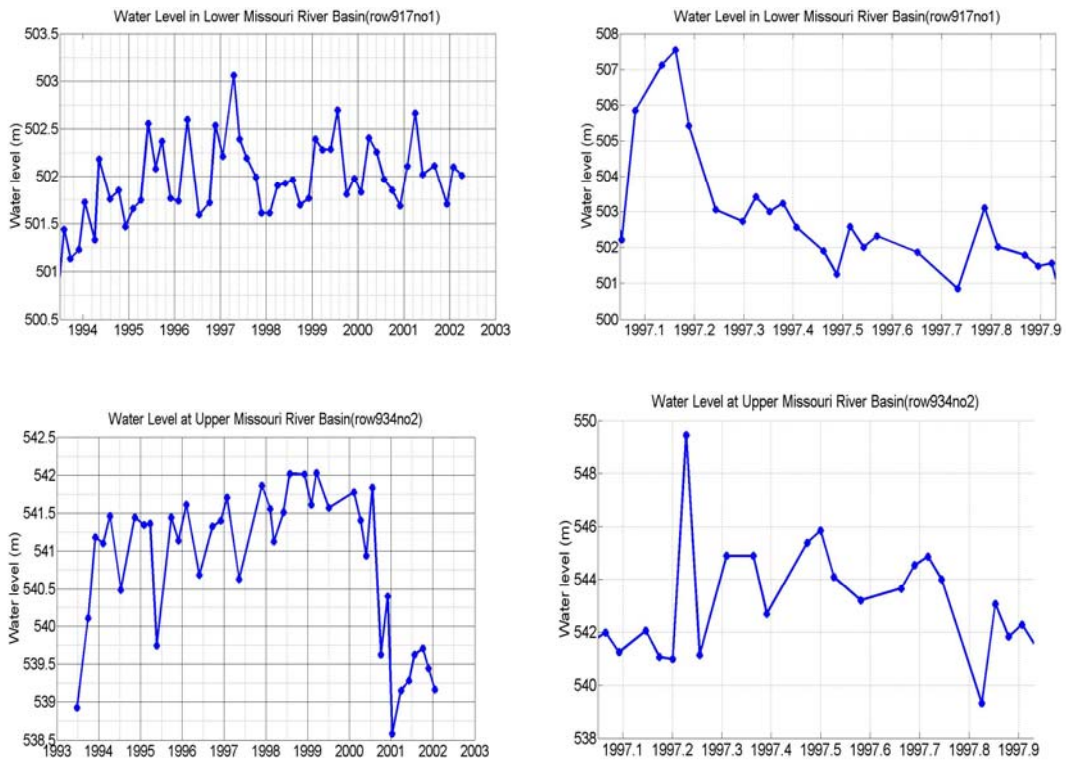


Figure 4.16: The height measurement of the body of water in the Missouri River Basin. The right side is 2-month sampling data from 1993-2003 and the left side is 10-day sampling data in 1997.

Similar to what we did in the Fargo and Grand Forks region, we extracted the height measurement showing 1997 flood with sampling rates of 2-month and 10-day in the Drayton, the Devis Lake basin, the Souris River Basin, and the Missouri River Basin, a few more example time series are presented in Figure 4.15 and Figure 4.16. In Figure 4.15 and Figure 4.16, the right side is 2-month sampling data from 1993-2003 which shows the water height is the highest in 1997 in the Drayton, the Devis Lake basin, the Souris River Basin, and the Lower Missouri River Basin, the left side is 10-day sampling data in 1997 which demonstrates the water level is the highest in Spring in 1997. The locations of the time series provided in this Section are shown in Figure 4.16 and Table 4.1. As we mentioned in Section 4.2, when we used the  $\sigma_0$  to study the flood coverage we detected the flooded region in the Souris River Basin in the northwest North Dakota (Figure 4.7), which was not recorded by USGS. This is further validated by the water level measurement from TOPEX altimetry provided in the last two plots in Figure 4.15, which indicate that the 1997 flood is also in the Souris River Basin. These results demonstrate that the satellite altimetry measured water height and the backscatter coefficient could provide the information of inundated regions, which were not completely measured by the USGS in situ stage gauges.

Basin	Name of the nearby location within 1degree	Longitude(E)	Latitude(N)	Column #	Row #	10Hz #
Red River of North	Fargo, ND	263.03	47.08	85	925	2
		262.90	46.95		922	3
		263.06	47.10		925	8
	Grand Forks, ND	263.17	48.12	102	947	5
		263.32	47.96		944	9
		263.45	47.84		941	4
	Drayton, ND	262.73	48.53	102	956	5
Devis Lake Basin	Edmore Coulee, ND	261.33	48.19		949	4
Souris River Basin	Deep River near Upham, ND	258.94	48.61	83	958	5
Upper Missouri River Basin	Spring Creek, ND	258.10	47.53	100	934	2
Lower Missouri River Basin	Apple Creek, ND	259.83	46.70	84	917	1
Minnesota River Basin	Minnesota River, MN	263.95	45.03	86	881	4
	Chippewa River, MN	264.30	45.42	86	889	8
		264.47	45.61	86	893	6
Upper Mississippi River Basin	Leech Lake River, MN	265.667	46.875	86	920	9
Rainy River Basin	Rainy River, MN	265.324	48.755	103	961	5
James River Basin	James River, MN	261.746	45.729	85	896	3
		262.61	43.48	86	848	8
Lower Mississippi River Basin	Des Moines River, SD	264.96	43.08	101	840	7

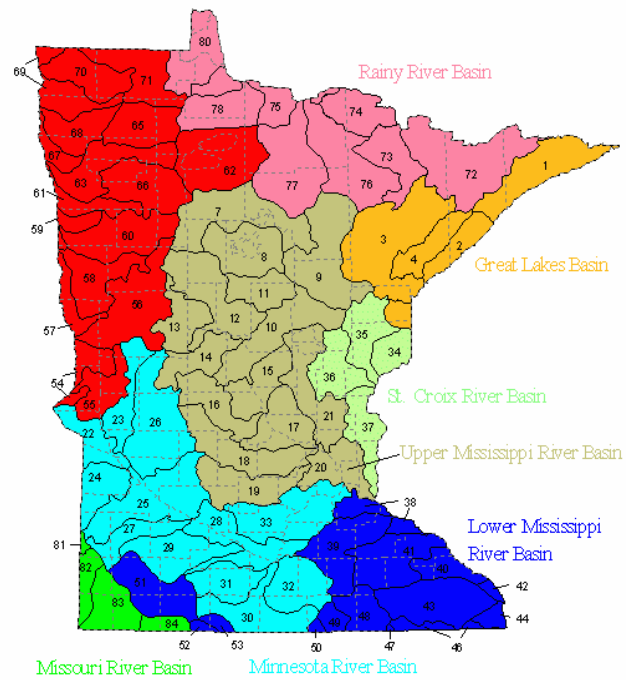
Table 4.1: The coordinates of the selected bodies of water showing the 1997 flood in the Red River of the North Basin, the Missouri River Basin, the Mississippi River Basin, the Minnesota River Basin and their sub-basins.

#### 4.4 The 1997 Flood in Minnesota, South Dakota and Iowa

Similar to the work in Section 4.3, we applied the same methodology and retrieved the TOPEX water height showing flood via the detected bodies of water using our algorithm, in the Minnesota River Basin, the Upper Mississippi River Basin and the Rainy River Basins in Minnesota. The locations of the River Basins in Minnesota are shown in Figure 4.17. The water heights with sampling rates of 2-month and 10-day are shown in Figure 4.18 through Figure 4.19, respectively. In addition, we extracted the water height measurements indicating flood at the James River Basin in South Dakota (Figure 4.20), and in the Des Moines River Basin in Iowa (Figure 4.19). The locations of the time series are shown in Figure 4.7 and Table 4.1. In Figure 4.18 through Figure 4.20, the right side is 2-month sampling data from 1993-2003 showing the water level is the highest in 1997, the left side is 10-day sampling data in 1997 demonstrating the water level is the highest in Spring of 1997.

## MAJOR BASINS AND WATERSHEDS OF MINNESOTA

Red River of the North Basin



 **Minnesota**  
**Department of Natural Resources**

Figure 4.17: The major basins in Minnesota (<http://www.dnr.state.mn.us/watersheds/map.html>).

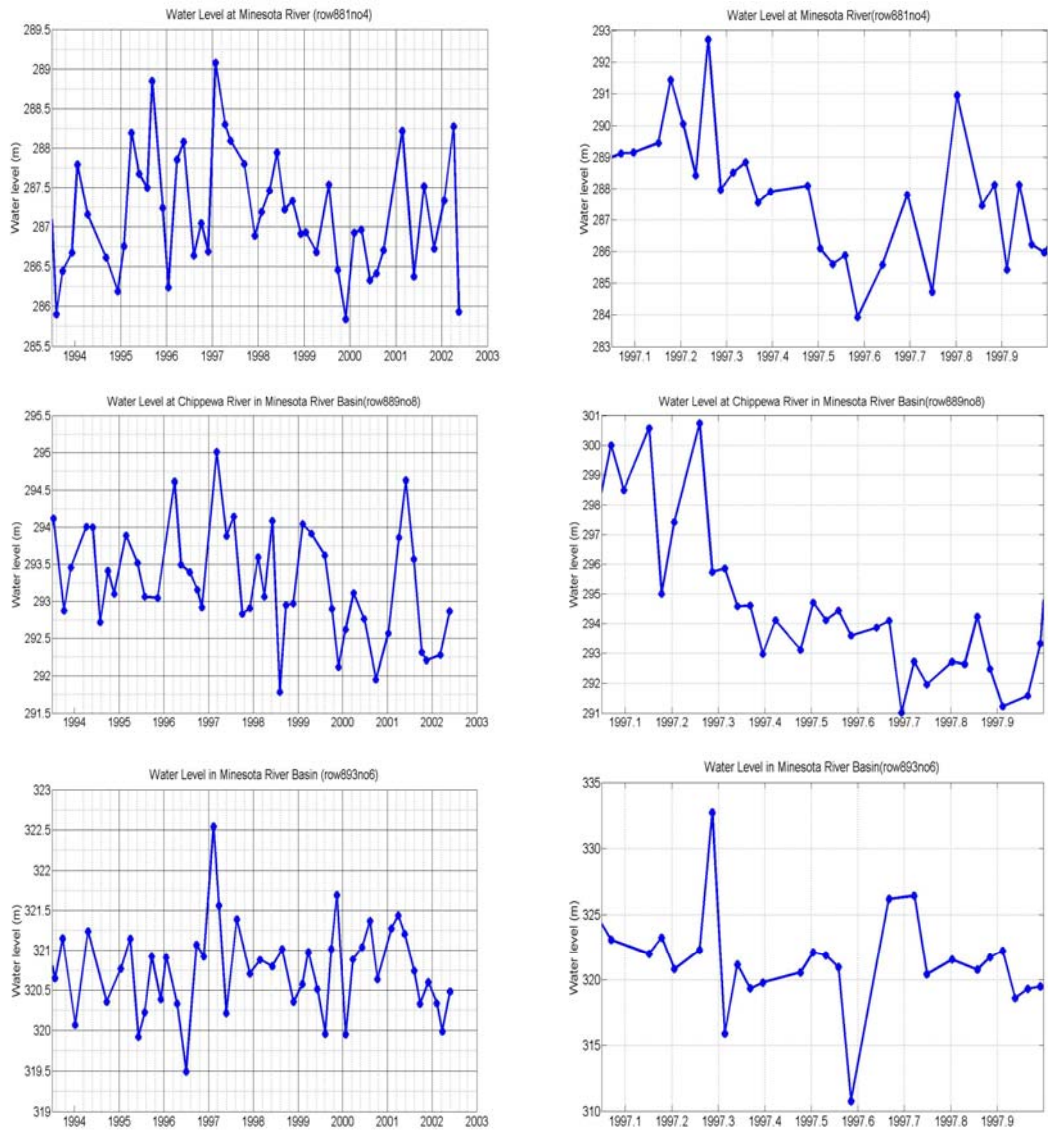


Figure 4.18: The height measurement of the example point in the Minnesota River Basin. The right side is 2-month sampling data from 1993-2003 and the left side 10-day sampling in 1997.

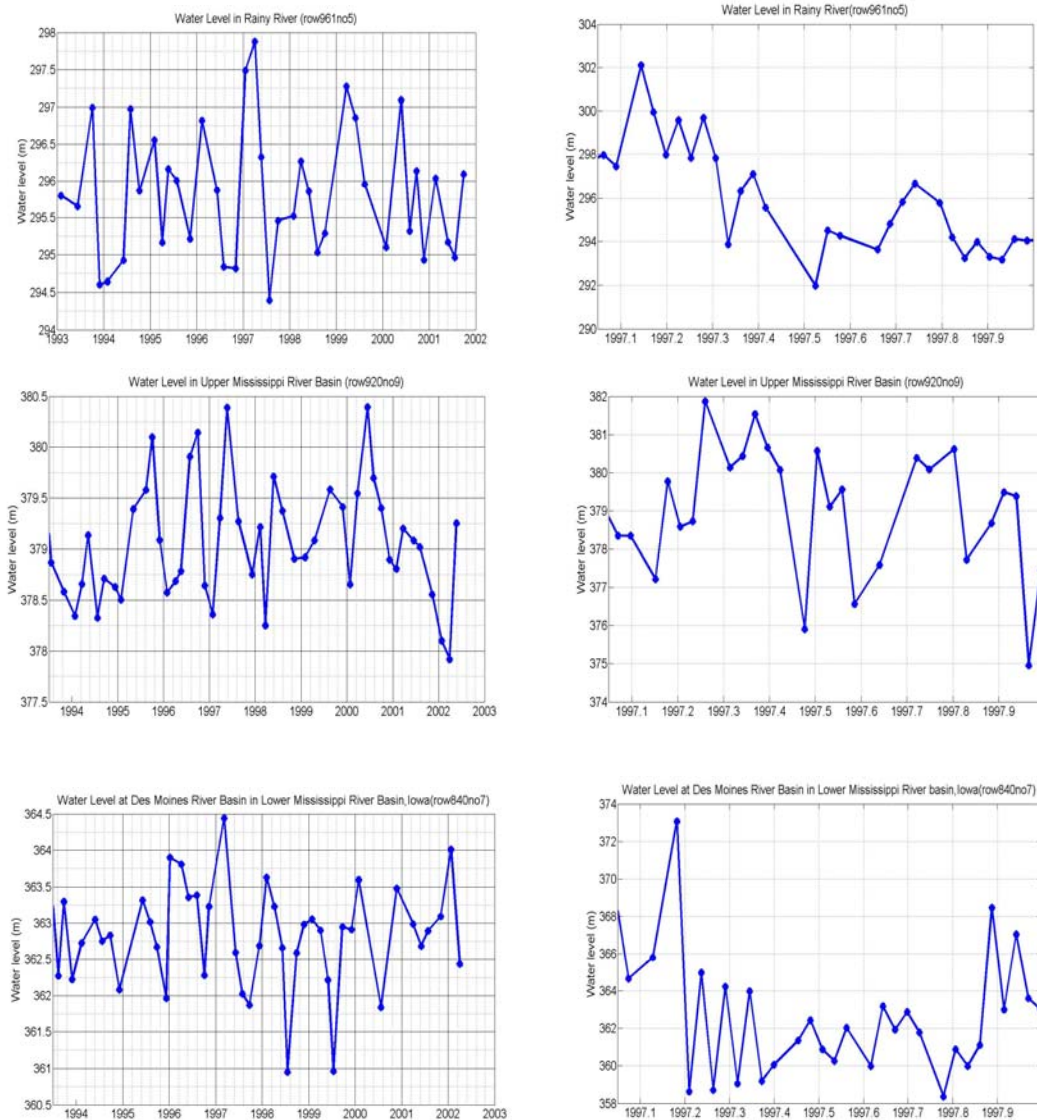


Figure 4.19: The height measurement of the example point in the Rainy River Basin, in the Upper Mississippi River Basin and in the Des Moines River Basin. The right side is 2-month sampling data from 1993-2003 and the left side is 10-day sampling data in 1997.

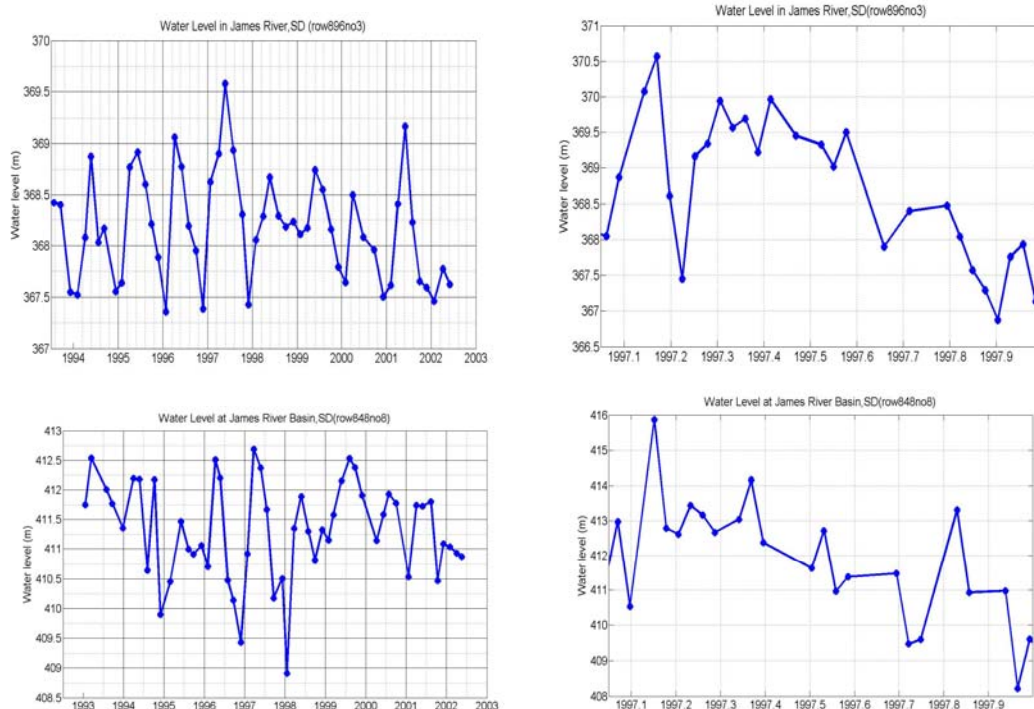


Figure 4.20: The height measurement of the example point in the James River Basin. The right side is 2-month sampling data from 1993-2003 and, the left side 10-day sampling data in 1997.

## 4.5 Conclusions

In this Chapter, we explored the application of the satellite altimetry for the 1997 Red River flood study, using the water detection algorithm, and the 10-Hz retracked TOPEX water height and the backscatter coefficients. First, we investigated the characteristics of the backscatter coefficient during the flood and snow coverage in North Dakota, South Dakota, Minnesota and Iowa. For the flood extent quantification, we compared the backscatter coefficient geographic plots in the time before, during and after the flood. The results indicate that the high backscatter coefficient ( $>35\text{dB}$ ) can be used to observe the flood extent. The detected flood extent using backscatter coefficient agrees with the USGS ground based stage gauge record. For the snow coverage detection, we compared the backscatter coefficient geographic plots during the 1997 Winter, Summer and Autumn seasons, the results show that the low backscatter coefficient ( $<10\text{dB}$ ) can be used to indicate snow coverage.

In addition, to the use of the backscatter coefficients, we applied the water detection algorithm using the 10-Hz retracked data to retrieve the water level measurement in the Red River Basin of the North in North Dakota and in western Minnesota, the upper Mississippi River Basin in Minnesota, the Missouri River Basin in southern North Dakota and in South Dakota. The extracted 10-Hz retracked water height measurements demonstrate that the water level is the highest during the 1997 flood. We compared the decadal TOPEX altimetry measurements with the nearby USGS gauge records and found out there is good seasonal agreements between the two measurements despite their location differences. In addition, we compared the 1-Hz non-retracked measurement with the 10-Hz retracked measurement and confirmed the importance of the 10-Hz retracked data in the flood monitoring. In addition to the agreement with USGS stage gauge record, we detected additional inundated flooding extent of the 1997 flood missed by USGS in the Souris River Basin in the northwestern North Dakota and in the Des Moines River Basin, Iowa using the TOPEX measurements. Our results demonstrate that satellite radar altimetry measured 10-Hz retracked water height and backscatter coefficients have excellent potential for the inland water flood monitoring which could provide valuable information for flood modeling and prediction, and thus flood mitigation.

## CHAPTER 5

### CONCLUSIONS

In this study, we explored the application of satellite altimetry to the inland hydrological study to maximize the usage of satellite altimetry in the continental water. We developed a water-detection algorithm based on the statistics of decadal height measurements to detect the bodies of water including the small bodies of water. In addition, we retrieved the individual 10-Hz retracked data, assessed the performance of 10-Hz retracked data in measuring the continental water level and explored the application of the backscatter coefficient in the land surface classification. Using TOPEX/POSEIDON data as demonstration, we tested the algorithm, researched the individual 10-Hz retracked measurement and the backscatter coefficient in Manitoba and SW Ontario, the Amazon River Basin, and the Southwest Taiwan. After that, we applied the methodology to monitor the 1997 Red River flood.

In Manitoba and SW Ontario region, to assess the accuracy of satellite altimetry measurement we first chose the large Lakes where there are available stage measurements for comparing the retracked TOPEX data with the non-retracked data and with the high-level altimetry data products from LEGOS and USDA & NASA/GSFC. The comparisons are conducted by computing the correlation coefficients of the satellite data with the stage measurement obtained from Environment Canada. The comparison shows the correlation coefficient of TOPEX data and in-situ data improved from 0.34 to 0.87 after retracking, which indicates the accuracy improvement using the retracked data. The individual 10-Hz retracked data yield a correlation coefficient of 0.98 which is higher than both 1-Hz non-retracked data and LEGOS high-level altimetry data product. The improved accuracy of the individual 10-Hz retracked data which has higher along track spatial resolution (~700m) indicates that using the individual 10-Hz retracked data could improve the spatial resolution of the measurement of small bodies of water underneath the satellite ground tracks. We compared the OCOG retracker, 10% threshold retracker, 20% threshold retracker, and 50% threshold retracker, and found that the 10% threshold retracker provided the best performance in study regions in Manitoba and SW Ontario lakes. Following the assessment of the

accuracy of the individual 10-Hz retracked data, we provided the 10-Hz measurement of small bodies of water detected using the algorithm and extracted the 10-Hz AGC at dry season and wet season. The results demonstrate that low AGC could indicate the snow coverage and high AGC could infer the flooded region.

In the Amazon River Basin, we compared the mask produced from the L-band Synthetic Aperture Radar (SAR) image with the water-detection algorithm and found the algorithm could detect the bodies of water, which were not sensed using the mask. The detected bodies of water are verified using the detailed local map in the 3 tested regions including 7 points. The comparison of the TOPEX 10-Hz retracked measurement with the nearby stage measurement shows good agreement in seasonal variations, which validates the accuracy of water level measurements of small bodies of water using satellite radar altimeter. We extracted the 10-Hz AGC in February, 1997 when the water level is high and in September, 1996 when the water level is low. The detailed local map demonstrates the AGC value is obviously high at the locations where there are bodies of water. Furthermore, comparison of the AGC value in wet season and dry season shows that the AGC value improved in the wet season and the area with high AGC value enhanced in the wet season, which indicate again the high AGC values can be used to detect the flooded region. The comparison of different retrackers shows the OCOG retracker is the best at Altamira in the Amazon River basin, which is different from the results in Hudson Bay region. Because the performance of retrackers varies with the region, we should choose carefully the best retracker for different regions.

In Southwestern Taiwan region, the monthly variation of the 10-Hz AGC from 1992-2002 demonstrates the AGC value is high in the rainy season and in the river regions. Based on this analysis, we detected the flooded region at 12:9:14-12:9:26 on August 3rd, 2002 using AGC. The body of water indicated by high AGC and detected by the algorithm is verified by the Google Earth image. We extracted decadal 10-Hz AGC and 10-Hz individual retracked data. There is the annual signal evident in the time series, which agrees with the annual variations of the rainfall due to the Monsoon. Besides the seasonal signal, we detected the semi-annual signal in AGC and water height, which implies the local climate with two rainy seasons in a year (Yen & Chen, 2000).

For the study of the 1997 Red River flood, we applied the same methodology to find the small bodies of water and retrieved the height measurements to record the flood. The comparisons of the extracted individual 10-Hz retracked data with the nearby USGS stage measurements demonstrate good agreements. We compared the 1-Hz non-retracked data and 10-Hz retracked data and found out the individual 10-HZ retracked data is indispensable for the flood monitoring. The comparison of the geographic variation of the backscatter coefficients during the 1997 Spring, Summer, Autumn and Winter seasons illustrates the low

backscatter (<10dB) coefficients could indicate the snow coverage. By comparing the geographic variations of the backscatter coefficients before, during and after the 1997 flood, it was found that the high backscatter coefficients (>35dB) imply the flooded region. The observed inundated regions from TOPEX include the Red River of the North basin in North Dakota and Minnesota, the Missouri River Basin in the North Dakota, the Mississippi River Basin and Minnesota River basin in Minnesota and their sub-basins. We extracted the individual 10-Hz height measurements showing the water level is very high during the 1997 flood over these regions. In addition to the agreement of the flooded regions, additional inundated area were detected in the Souris River Basin, northwest of North Dakota and in the Des Moines River Basin, Iowa using the backscatter coefficients and the individual 10-Hz retracked water height measurements.

## BIBLIOGRAPHY

Alsdorf, D., C. Birkett, T. Dunne, J. Melack, L. Hess, 2001. Water level changes in a large Amazon lake measured with spaceborne radar interferometry and altimetry. *Geophysical Research Letters*, 28(14), 2671-2674.

Alsdorf, D., J. Melack, T. Dunne, L. Mertes, L. Hess, L. Smith, 2000. Interferometric radar measurements of water level changes on the Amazon Floodplain. *Nature*, 404, 174-177.

Alsdorf, D., E. Rodriguez, D. P. Lettenmaier, 2007. Measuring surface water from space. *Reviews of Geophysics*, 45, RG2002, doi:10.1029/2006RG000197.

Anzenhofer, M., C. Shum, M. Renssch, 2000. Coastal altimetry and applications. *Geodetic Science and Surveying Report #464*, The Ohio State University.

Bamber, J.L., 1994. Ice sheet altimeter processing scheme. *International Journal of Remote Sensing*, 15(4), 925-938.

Barrick, D.E., B.J. Lipa, 1985. Analysis and interpretation of altimeter sea echo. *Advances in Geophysics*, 27, 60-99.

Berry, P.A.M., J.D. Garlick, J.A. Freeman, E. L. Mathers, 2005. Global inland water monitoring from multi-mission altimetry. *Geophysical Research Letters*, 32, L16401, doi:10.1029/2005GL022814.

Benveniste, J., et al., 2002. ENVISAT RA-2/MWR product handbook, Issue 1.2, PO-TN-ESR-RA-0050, Frascati, Italy, European Space Agency.

Bracewell, R. N., 1986. *The Fourier transform and its application*. McGraw-Hill, New York.

Brooks, R. L., 1982. Lake elevation from satellite radar altimetry from a validation area in Canada. Report, Geoscience Research, Corporation: Salisbury, MD, USA.

Brown, G.S., 1977. The average impulse response of a rough surface and its applications. *IEEE Transactions on Antennas and Propagation*, 25, 67-74.

Birkett, C.M., 1995. The contribution of TOPEX/POSEIDON to the global monitoring of climatically sensitive lakes. *Journal of Geophysical Research*, 25,179-25.

Birkett, C.M., 1998. Contribution of the TOPEX NASA radar altimeter to the global monitoring of large rivers and lakes. *Water Resources Research*, 34(5), 1223-239.

Birkett, C.M., 2000. Synergistic remote sensing of lake Chas: Variability of basin inundation. *Remote Sensing of Environment*, 72, 218-236.

Birkett, C.M., L.A.K. Mertes, T. Dunne, M.H. Costa, M.J. Jasinski, 2002. Surface water dynamics in the Amazon Basin: Application of satellite radar altimetry. *Journal of Geophysical Research*, 107, doi:10.1029/2001JD000609.

Cazenave, A., P. Bonnefond, K. Dominh, P. Schaeffer, 1997. Caspian sea level from TOPEX/POSEIDON altimetry: level now falling. *Geophysical Research Letters*, 24(8), 881-884.

Chelton, D. B., Walsh, E. J., J. L. MacArthur, 1989. Pulse compression and sea level tracking in satellite altimetry. *Journal of Atmospheric Oceanic Technology*, 6, 407-438.

Chelton, D.B., J. Ries, B. Haines, F. Lee, P. Callahan, 2001. *Satellite Altimetry*. Chapter 1, In "Satellite Altimetry and Earth Sciences", Academic Press, California.

Coe, T. M., Birkett, C., 2004. Calculation of river discharge and prediction of lake height from satellite radar altimetry: Example for the Lake Chad Basin. *Water Resources Research*, 40, W10205, doi:10.1029/2003WR002543.

Cudlip, W., J. K. Ridley, C. G. Rapley, 1990. The use of satellite radar altimetry for monitoring wetlands, in *Remote Sensing and Global Change*. Proceedings of the 16<sup>th</sup> Annual Conference of the Remote Sensing Society, 207-216.

Davis, C., 1993. A surface and volume scattering retracking algorithm for ice sheet satellite altimetry. *IEEE Transactions on Geoscience & Remote Sensing*, 31(4), 811-818.

Davis, C., 1995. Growth of the Greenland ice sheet: a performance assessment of altimeter retracking algorithms. *IEEE Transactions on Geoscience & Remote Sensing*, 33(5), 1108-1116.

Davis C., 1996. A robust threshold retracking algorithm for extracting Ice-Sheet surface elevations from satellite radar altimeters. *Geoscience & Remote Sensing Symposium*, 3, 1783-1787.

Davis, C., 1997. A robust threshold retracking algorithm for measuring ice-sheet surface elevation change from satellite Radar Altimeters. *IEEE Transactions on Geoscience and Remote Sensing*, 35(4), 974-979.

Dingman, S., 2002. *Physical Hydrology*. Prentice Hall, ISBN-10: 0130996955.

Fu, L., E. J. Christensen, C.A. Yamarone, M. Lefebvre, Y. Menard, M. Dorrer, P. Escudier, 1994a. TOPEX/POSEIDON mission overview. *Journal of Geophysical Research*, 99, 24369-24381.

Fu, L., G. Pihos, 1994b. Determining the response of sea level to atmospheric pressure forcing using TOPEX/POSEIDON data. *Journal of Geophysical Research*, 99, 24633-24642.

Fu, L., A. Cazenave, 2001. *Satellite altimetry and earth science*. Academic Press, ISBN-10: 0122695453.

Fedor, L. S., T. Godbey, J. Gower, R. Guptill, G. Hayne, L. Rufenach, J. Walsh, 1979. Satellite altimeter measurements of sea state-An algorithm comparison. *Journal of Geophysical Research*, 87, 3991-4001.

Frappart F., S. Calmant, M. Cauhopé, F. Seyler, Cazenave, 2006. Preliminary results of ENVISAT RA-2-derived water levels validation over the Amazon basin. *Remote Sensing of Environment*, 100, 252-264.

GeoForschungsZentrum Potsdam, 1998. *Envisat D-PAC Phase C/D, Technical Note, Retracking*, 1, ENV-GFZ-TN-VAO-3400-0001.

Gleick, P. H., 2003. Global freshwater resources: Soft-path solutions for the 21st century. *Science*, 302, 1524-1528.

Guzkowska, M. A., C. G. Rapley, J. K. Ridley, W. Cudlip, C. M. Birkett, R. F. Scott, 1990. Developments in inland water and land altimetry. European Space Agency Conference Report, CR-7839/88/F/FL.

Hayne, G. S., 1980. Radar altimeter mean return waveforms from near normal incidence ocean surface scattering. *IEEE Transactions on Antennas and Propagation*, 28, 687-692.

Hayne, G. S., D.W. Hancock, C. L. Purdy, P. S. Callahan, 1994. The corrections for significant wave height and attitude effects in the TOPEX radar altimeter. *Journal of Geophysical Research*, 99 (C12), 24941-24955.

Hess, L. L, J. M. Melack, E. M. Novo, C. F. Barbosa, M. Gastil, 2003. Dual-season mapping of wetland inundation and vegetation for the central Amazon basin. *Remote Sensing of Environment*, 87, 404-428.

Ingram R. G., S. Prinsenber, 1998. Coastal oceanography of Hudson Bay and surrounding eastern Canadian Arctic waters. *The Sea*, 11, 835-861.

Koblinsky, C.J., R.T. Clarke, A.C. Brenner, H. Frey, 1993. Measurement of river level variations with satellite altimetry. *Water Resources Research*, 29(6), 1839-1848.

Kruizinga, G.L., 1997. Validation and applications of satellite radar altimetry. Ph.D. Dissertation, the University of Texas, Austin, Texas, USA.

Lacomme, P., J. Hardange, J. Marchais, E. Normant, 2001. *Air and Spaceborne Radar Systems: An Introduction*. William Andrew Publishing, Norwich, New York.

Lee, H., C. Shum, Y. Yi, A. Braun, C.-Y. Kuo, 2008. Laurentia Crustal Uplift Observed Using Satellite Altimetry. *Journal of Geodynamics*, 46, 182-193.

Lee, H., C. Shum, Y. Yi, M. Ibaraki, J.-W. Kim, A. Braun, C.-Y. Kuo, Z. Lu, 2009. Louisiana wetland water level monitoring using retracked TOPEX/POSEIDON altimetry. *Marine Geodesy*, in review.

Marburger, J. H., J. B. Bolten, 2004. Administration research and development budget priorities. Executive Office of the President Office, Washington, D. C. (Available at <http://www.whitehouse.gov/omb/memoranda/fy04/m04-23.pdf>).

Marburger, J. H., J. B. Bolten, 2005. FY 2007 administration research and development budget priorities. Executive Office of the President Office, Washington, D. C. ([http://www.ostp.gov/html/budget/2007/ostp\\_omb\\_guidancememo\\_FY07.pdf](http://www.ostp.gov/html/budget/2007/ostp_omb_guidancememo_FY07.pdf)).

Margalef, R., 1994. Limnology now: A paradigm of planetary problems. Elsevier Science, New York, ISBN O-444-89826-3.

Martin, T. V., H. J. Zwally, A. C. Brenner, R. A. Bindshadler, 1983. Analysis and retracking of continental ice sheet radar altimeter waveforms. *Journal of Geophysical Research*, 88, 1608-1616.

Maul, G.A., 1985. Introduction to satellite oceanography. Martinus Nijhoff, Dordrecht, The Netherlands.

Macek-Rowland, K.M., 1997. 1997 floods in the Red River of the North and Missouri River Basins in North Dakota and western Minnesota. U.S. Geological Survey Open-File Report 97-575 (<http://nd.water.usgs.gov/pubs/ofr/ofr97575/index.html>).

Macek-Rowland, K.M., M. J. Burr, G. B. Mitton, 2001a. Peak discharges and flow volumes for streams in the northern plains, 1996-97. U.S. Geological Survey Circular 1185-B (<http://pubs.er.usgs.gov/usgspubs/cir/cir1185B>).

Macek-Rowland, K.M., M. J. Burr, G. B. Mitton, 2001b. Precipitation in the northern plains, September 1996 through April 1997. U.S. Geological Survey Circular 1185-A (<http://pubs.er.usgs.gov/usgspubs/cir/cir1185A>).

Mercier, F., A. Cazenave, C. Maheu, 2002. Interannual lake level fluctuations (1993-1999) in Africa from TOPEX/POSEIDON: connections with ocean-atmosphere interactions over the Indian Ocean. *Global and Planetary Changes*, 32, 143-163.

Morris, C. S., S. K. Gill, 1994. Evaluation of the TOPEX/POSEIDON altimeter system over the great lakes. *Journal of Geophysical Research*, 99(C12), doi: 10.1029/94JC01642.

Moore, R. K., C. S. Williams, 1957. Radar terrain return at near-vertical incidence. *Proceedings of the Institute of Radio Engineers*, 45(2), 228-238.

Oki, T., S. Kanae, 2006. Global hydrological cycles and world water resources. *Science*, 313, 1068-1072.

Papa, F., C. Prigent, W. B. Rossow, 2007. Ob's River flood inundations from satellite observations: A relationship with winter snow parameters and river runoff. *Journal of Geophysical Research*, 112, D18103, doi: 10.1029/2007JD008451.

Papa, F., B. Legresy, F. Remy, 2003. Use of the TOPEX-POSEIDON dual-frequency radar altimeter over land surfaces. *Remote Sensing of Environment*, 87, 136-147.

Prigent, C., F. Papa, F. Aires, W.B Rossow, E. Matthews, 2007. Global inundation dynamics inferred from multiple satellite observations, 1993-2000. *Journal of Geophysical Research*, 112, D12107, doi: 10.1029/2006JD007847.

Rapley, C. G., M. A. J. Guzkowska, W. Cudlip, I. M. Mason, 1987. An exploratory study of inland water and land altimetry using Seasat data. Report, 6483/85/NL/BI, European Space Agency, Paris.

Perry, C.A., 2005. Summary of significant floods in the United States and Puerto Rico, 1994 through 1998 water years. U.S. Geological Survey Scientific Investigations Report 2005-5194.

Rodriguez, E., 1988. Altimetry for non-Gaussian oceans: height biases and estimation of parameters. *Journal of Geophysical Research*, 93, 14107-14120.

Seyler, F., A. Cazenave, F. Huynh, F. Mercier, L. Tocqueville, S. Calmant, M.-P. Bonnet, G. Cochonneau, M.-C. Gennero, M. Mangeas, 2007. Contribution of spatial altimetry to hydrology; The CASH project. Comité National Français de Géodésie et Géophysique Rapport Quadriennal 2003-2006, 315-344.

Stewart, D.B., 2000. What makes Hudson Bay special. Fisheries and Oceans Canada Hudson Bay Workshop Reports.

Shum, C., 1995. Development of an optimal and automated radar altimeter waveform processor. Technical Report, Center for Space Research, University of Texas.

Stanev, E. V., E. L. Peneva, F. Mercier, 2004. Temporal and spatial patterns of sea level in inland basins: Recent events in Aral Sea. *Geophysical Research Letters*, 31, L15505, doi:10.1029/2004GL020478.

Townsend, W. F., J. T. McGoogan, E. J. Walsh, 1981. *Satellite radar altimeters: present and future oceanographic capabilities*. Plenum Press, New York.

Ulaby, F.T. Moore, R. K., Fung, A. k., 1981. *Microwave Remote Sensing Fundamentals and Radiometry*. Addison-Wesley, Reading, Massachusetts.

U.S. Department of Commerce, National Oceanic and Atmospheric Administration, National Environmental Satellite, Data and Information Service,  
--1996-97a, Climatological data, Minnesota, September 1996 through April 1997: Asheville, North Carolina, 102(9) through 103(4).  
--1996-97b, Climatological data, North Dakota, September 1996 through April 1997: Asheville, North Carolina, 105(9) through 106(4).  
--1996-97c, Climatological data, South Dakota, September 1996 through April 1997: Asheville, North Carolina, 101(9) through 102(4).

Yen, M.-C., T.-C. Chen, 2000. Seasonal variation of the rainfall over Taiwan. *International Journal of Climatology*, 20, 803-809.

Yi. Y., 2000. Ohio State University Stackfiles. Geodetic Science Report, The Ohio State University.

Zakharova, A. E., A. V. Kouraev, A. Cazenave, F. Seyler, 2006. Amazon River discharge estimated from TOPEX/POSEIDON altimetry. *Comptes Rendus Geosciences*, 338(3), 188-196.

Zakharova, A. E., A. V. Kouraev, J. Cretaux, F. Al-Yamani, I. Polikarpov, 2007. Radar altimetry for studies of large river basins: hydrological regime of the Euphrates-Tigris Rivers. *Envisat Symposium 2007*, Montreux, Switzerland.

Zieger, A. R., D.W. Hancock, G. S. Hayne, C. L. Purdy, 1991. NASA radar altimeter for the TOPEX/POSEIDON project. *Proceedings of the IEEE*, 79, 810-826.